# EPITAXIAL GROWTH OF RARE-EARTH TRIFLUORIDES ON III-V SEMICONDUCTORS

By

Sayuri Ritchie

B. Sc. (Physics) University of Waterloo

M. Sc. (Physics) University of Waterloo

A THESIS SUBMITTED IN PARTIAL FULFILLMENT OF

THE REQUIREMENTS FOR THE DEGREE OF

DOCTOR OF PHILOSOPHY

in

THE FACULTY OF GRADUATE STUDIES

DEPT. OF PHYSICS

We accept this thesis as conforming

to the required standard

THE UNIVERSITY OF BRITISH COLUMBIA

September 1998

In presenting this thesis in partial fulfilment of the requirements for an advanced degree at the University of British Columbia, I agree that the Library shall make it freely available for reference and study. I further agree that permission for extensive copying of this thesis for scholarly purposes may be granted by the head of my department or by his or her representatives. It is understood that copying or publication of this thesis for financial gain shall not be allowed without my written permission.

Physics
The University of British Columbia
2075 Wesbrook Place
Vancouver, Canada
V6T 1Z1

Date: Sep. 16, 1998

_____

## Abstract

Epitaxial growths of rare-earth trifluorides on III-V semiconductors have been investigated. Synchrotron photoemission spectroscopy showed a complete coverage of III-V substrates by $LaF_3$ and $ErF_3$ films and interfacial chemical reactions at the interface. In the $LaF_3$ films on GaAs(111) substrates, residual tensile strains were detected by high-resolution X-ray diffraction (HRXRD) contrary to the expected compressive strains in the case of a pseudomorphic growth. The tensile strains are interpreted as being due to the differential thermal contractions of the fluorides and the semiconductors during cooling.

The correlations between the bulk structure and the surface structure of the $LaF_3$ films on GaAs and InP substrates have been studied by X-ray rocking curve measurements, grazing incidence X-ray scattering and atomic force microscopy. The lateral coherence lengths in the $LaF_3$ films from the X-ray rocking curves and the height-height surface correlation lengths from the X-ray scattering and the atomic force microscopy were comparable to each other and were associated with the lattice mismatch of the system at the growth temperature. The results are interpreted in terms of strain relieving defects surrounding the columns of coherent crystals.

The kinetics of $LaF_3$ film growths on III-V semiconductors were investigated using the self-affine surface structure analysis for the X-ray specular/diffuse scattering and the atomic force microscopy. The scaling exponents for the film growth obtained from the analysis were closest to the exponents predicted by the Villain-Lai-Das Sarma model in which the surface diffusion of deposited particles is the most important process in the film growth.

InP single crystal islands have been grown on $LaF_3$/InP(111) heterostructures. The InP islands are observed to be faceted with three-fold symmetry as expected for (111) orientation. A small broadening of the InP substrate diffraction peak is interpreted as being due to inhomogeneous strains associated with the InP islands and differential thermal contraction of the $LaF_3$ films during cooling.

## Table of Contents

## List of Tables

## List of Figures

## Acknowledgement

I would like to thank my mighty supervisor Tom Tiedje for his patient guidance and support. I would like to thank Jim McKenzie for countless help during my research. I thank Yuan Gao and Tony van Buuren for their help and assistance in the lab and at the Synchrotron Center in Wisconsin. I would like to thank Mario Beaudoin and Ahmad Kassai for their technical help in the lab and for their support during this difficult time. I thank Christian Lavoie and Shane Johnson for teaching me many things during my first years. I thank my Ph.D. committees, Birger Bergerson, Janis McKenna and Jeff Young for their suggestions and advise for my project. I thank Phil Wong for performing the XPS measurements for this project and Andrew Leung for taking the LEED photographs. I thank the people in the lab, past and present, Al, Anders, Christina, Duncan, Mari and Martin for various help and support. I thank Wen-Kai Zhong and Tom Pinnington for assisting me with atomic force microscope.

I would like to thank my kendo teachers Dave Harding and Hiro Okusa for their support and encouragement during the last two years. I also thank the people in the UBC Kendo Club, especially Pierre and Bob for the friendship and for making the life enjoyable. I thank my Zen teacher Hosaka Sensei for teaching me the way of life.

I would finally like to thank my husband Ken Ritchie for constant support and encouragement during my study.

# Chapter 1

## Introduction

Epitaxial growth of fluorides on semiconductors has attracted considerable attention in the past decade due to its potential applications in the semiconductor industry. The epitaxial fluorides on III-V semiconductors such as GaAs and InP, in particular have applications in optical devices such as the integrated semiconductor pumped solid state lasers [1, 2] and the vertical cavity surface emitting lasers [3]. Other applications include gate insulators in three dimensional integrated devices. Use of epitaxial fluorides in these applications is especially important for compound semiconductors such as GaAs and InP since they lack a high quality native oxides analogous to $SiO_2$ for Si.

Most of the previous work on the fluorides have been dedicated to the alkaline earth fluorides, $CaF_2$, $SrF_2$ and $BaF_2$ mainly due to their cubic-fluorite structure which is similar to diamond and zinc-blend structures of group IV and III-V semiconductors. Several studies have also been done on the growth of lanthanide trifluorides on semiconductors. Sinharoy *et al.* have reported the epitaxial growth of crack-free $LaF_3$ films of up to 200 nm thick on GaAs(111) substrates [5]. They have characterized the surface of the films using low-energy electron diffraction (LEED) and reflection high-energy electron diffraction (RHEED). Strüumpler *et al.* have grown epitaxial $LaF_3$ films on Si(111)[6]. They have studied the surface structure by LEED and scanning electron microscopy (SEM) and the crystal structure by X-ray diffraction (XRD) using the angle-dispersive scanning detection. They have observed the epitaxial islands on the film of thickness less than 15 nm. The surface of the films of thickness greater than 15 nm were found to be smooth.

They have also shown that the *c*-axis of $LaF_3$ films is oriented parallel to the [111] direction of Si substrates. The (111) surfaces of substrates were used instead of (100) surfaces because the structures and the lattice spacing of the trigonal face of the trifluorides are the closest to those of the (111) substrate surfaces of the semiconductors as we show in Sec. 1.1. A number of studies have been performed on interfacial reactions and band alignments of lanthanide trifluorides on Si(111) using photoemission spectroscopy [7, 8, 9, 10]. The surface structures of lanthanide trifluoride films on semiconductors has also been studied by LEED and RHEED [7, 10, 11]. They have shown that the trigonal structures of $HoF_3$ and $GdF_3$ which are normally only stable at high temperatures, are stable at room temperature for thin layers (1–20 nm) deposited on Si(111), Ge(111) and GaAs(111)B substrates.

In this study, the epitaxial growth of rare-earth fluoride films on III-V semiconductors, particularly $LaF_3$ and $ErF_3$ films grown on GaAs and InP substrates are investigated. One aim of this study is to epitaxially grow high quality rare-earth fluoride films on III-V semiconductors. The term *epitaxy* means the oriented or single-crystalline growth of one material upon another such that there exist crystallographic relations between the film and the substrate. Certain crystallographic directions in the film and the substrate are parallel. Another aim of this study is to gain insights into the mechanisms whereby the insulator films grow on semiconductors. We will achieve this by studying the system from various aspects such as crystal structures using the high-resolution X-ray diffraction (HRXRD), surface morphologies using the X-ray specular and diffuse scattering and chemical compositions of the film/substrate interface using the synchrotron photoemission spectroscopy. The study of film crystal properties using the high-resolution X-ray diffraction have been performed on the epitaxial $LaF_3$ films for the first time. The surface morphology study using the X-ray specular and diffuse scattering of the fluoride films on semiconductors have never been performed previously.

In the first part of this study, the growth process at the initial stages of the film growth are studied. For this purpose, very thin fluoride films of less than 10 nm are grown on III-V semiconductors. The growth process is determined by examining the surface morphologies and the chemical interactions at the film/substrate interfaces. The experiments are done by photoemission spectroscopy with synchrotron radiation. (Chapter 3)

In Chapter 4, the growth mechanism at the later stage of the film growth is investigated. To achieve this, thick fluoride films of thickness 10–400 nm are grown on III-V semiconductors. The bulk structural properties of the films such as crystal orientations, strains and defects are studied by X-ray diffraction.

Finally, the kinetic mechanisms of the film growth are described using the scaling laws for self-affine surfaces. For this purpose, the surface height is modelled with a self-affine correlation function and the evolution of surface morphology with time or the film thickness $t$ and with the spatial frequency $q$ is determined using X-ray scattering and atomic force microscopy. By comparing the results with theoretical continuum models, we can infer about the dominant mechanisms of the film growth such as surface diffusion, evaporation and recondensation of the deposited species. (Chapter 5)

In Chapter 6, the growth of III-V semiconductors, InP and GaAs on rare-earth trifluoride/III-V semiconductor structures is investigated. The surface morphlogy of these structures is studied by AFM, SEM and X-ray scattering. The structure of the layers is studied by X-ray diffraction and the chemical composition of the system is studied by X-ray photoelectron spectroscopy.

The structural properties and surface morphology of the fluoride films are also technically important. The crystalline properties of the films and the surface morphology affect the growth of the more complicated structures such as semiconductor/fluoride/semiconductor systems. The surface and interface roughness have a great influence on the power loss

Table 1.1: Some physical properties of $LaF_3$, $ErF_3$ and $CaF_2$

| | $LaF_3$ | $ErF_3$ | $CaF_2$ |
|---|---|---|---|
| Crystal Structure | Trigonal | Orthorhombic | Cubic-fluorite |
| | $P\bar{3}c1 - D^4_{3d}$ | $Pnma - D^{16}_{2h}$ | |
| Lattice Parameters | $a = 7.185$Å | $a = 6.354$ Å | $a = 5.4640$ Å |
| | $c = 7.351$ Å | $b = 6.846$ Å | |
| | | $c = 4.380$ Å | |
| Mismatch with GaAs | +3.8 % | -8.6 % ($a$-axis), +9.0 % ($c$-axis) | -3.3 % |
| with InP | -0.04% | -12 % ($a$-axis), +5.4 % ($c$-axis) | -6.9 % |
| Melting Point | 1493°C | 1140°C | 1423°C |
| Density | 5.938 g/cm$^3$ | 7.772 g/cm$^3$ | 3.179 g/cm$^3$ |
| | 6 molecules/cell | 4 molecules/cell | 4 molecules/cell |
| Band Gap | 9.92 eV | – | 12.1 eV |

in the optical waveguides through scattering and the carrier mobilities in electronic devices. The stability of the films upon annealing will also be important in the subsequent processing during device fabrication.

## 1.1 Physical Properties of $LaF_3$

The physical properties of $LaF_3$ are summarized in Table 1.1. The crystal structure of $LaF_3$ is trigonal ($P\bar{3}c1 - D^4_{3d}$). A plan view of the $a \times a$ trigonal plane of $LaF_3$ is shown in Fig. 1.1. The $a \times a$ trigonal basal plane of $LaF_3$ is similar to the hexagonal (111) face of semiconductors with the diamond or zinc-blend structures. The crystal structure of $ErF_3$ is orthorhombic (Pnma). Projection along the $c$-axis and a view from the direction perpendicular to the $c$ axis of the orthorhombic structure of $ErF_3$ is shown in Fig. 1.2.

The rare-earth trifluorides $SmF_3$ to $LuF_3$ are known to undergo high-temperature dimorphism, inverting from trigonal to orthorhombic crystals on cooling [14]. The trifluorides $LaF_3$ to $NdF_3$ exist only in trigonal form. The trigonal lattice constant ($a$-axis) of

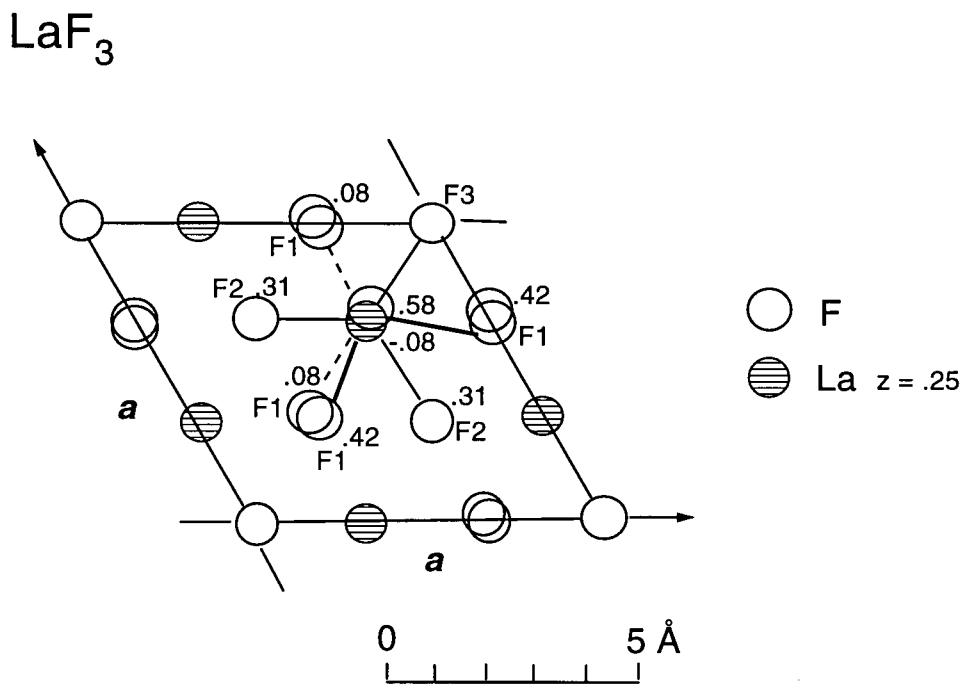


Figure 1.1: Projection along the $c$-axis of the trigonal structure of $LaF_3$ showing the nine coordinations of the La atom at the (0.3401, 0.3401, 0.25) position. The numbers indicate the positions of the fluorine atoms along the $c$-axis. Double circles indicate that the atoms are overlapped at those positions.

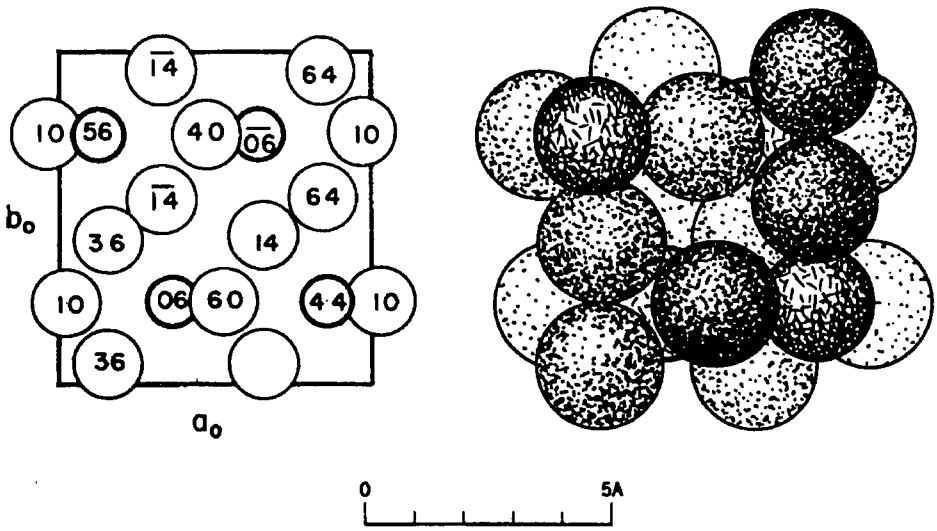


Figure 1.2: Projection along the c-axis (left) and a view from the direction perpendicular to the *c*-axis (right) of the orthorhombic structure of $ErF_3$ from Ref. [13]. The larger circles are the fluorine (F) atoms and the smaller circles are the erbium (Er) atoms. The numbers in the circles indicate the positions of atoms along the c-axis.

the rare earth trifluorides at room temperature is plotted in Fig. 1.3. The lattice distances of hexagonal (111) faces of GaAs and InP are also plotted. Linear expansion coefficients of $LaF_3$ have been used to estimate the approximate constants at room temperature from the high temperature data in Ref [14]. The trigonal lattice constants of the trifluorides lies approximately between the hexagonal lattice spacing of GaAs and InP(111).

The difference in thermal expansion coefficients between $LaF_3$ and GaAs or InP is smaller than the difference between $CaF_2$ and GaAs or InP. Linear thermal expansion and thermal expansion coefficients of $LaF_3$ are listed in Table 1.2. At room temperature, the thermal expansion coefficient of $LaF_3$ is 16 $\times 10^{-6}K^{-1}$ and that of $CaF_2$ is 19 $\times 10^{-6}K^{-1}$ whereas the thermal expansion coefficient of GaAs is $5.7 \times 10^{-6}K^{-1}$ and that of InP is $4.8 \times 10^{-6}K^{-1}$. The $LaF_3$ crystal is also known to be mechanically hard and chemically stable [17, 14]. A summary of physical properties of $LaF_3$ can be found in Ref. [17]. The

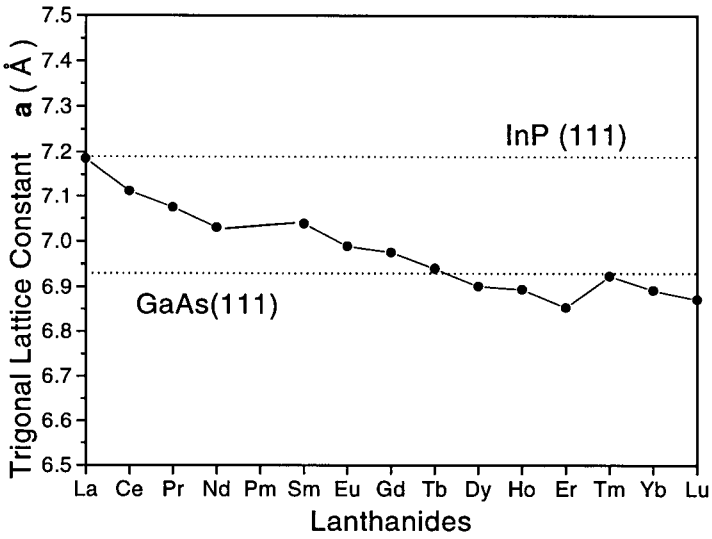


Figure 1.3: Trigonal lattice constant ($a$-axis) of the rare earth trifluorides at room temperature. The dotted lines are the lattice distances of hexagonal (111) faces of GaAs and InP. Linear expansion coefficients of $LaF_3$ have been used to estimate the approximate constants at room temperature from the high temperature data in Ref [14].

Table 1.2: Linear thermal expansion $\Delta L/L$ of $LaF_3$ where $L$ is a length at 0°C, thermal expansion coefficients $\alpha$ of $LaF_3$, GaAs and InP as a function of temperature from Ref. [15].

| Temperature (°C) | $\Delta L/L$ (%) | $LaF_3$ $\alpha$ ($\times 10^{-6}$ $K^{-1}$) | GaAs $\alpha$ ($\times 10^{-6}$ $K^{-1}$) | InP $\alpha$ ($\times 10^{-6}$ $K^{-1}$) |
|---|---|---|---|---|
| 29 | 0.014 | 15.8 | 5.7 | 4.3 |
| 180 | 0.291 | 18.0 | 6.5 | 4.7 |
| 380 | 0.669 | 20.6 | 6.9 | – |
| 580 | 1.111 | 23.3 | 7.2 | 6.1 |
| 780 | 1.635 | 33.6 | – | – |

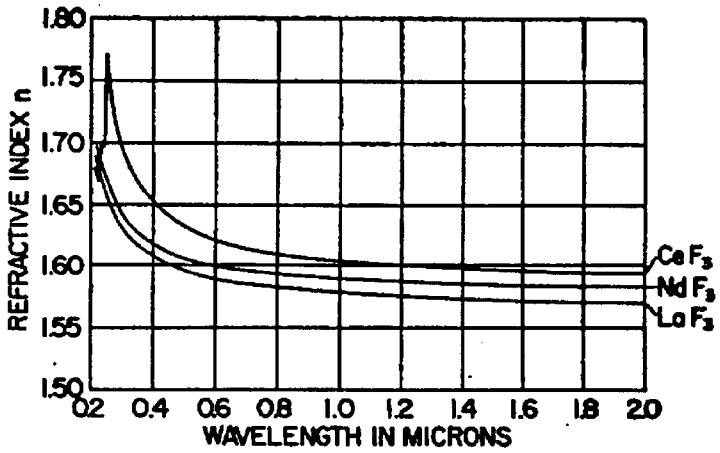


Figure 1.4: Refractive indices of films of $CeF_3$, $NdF_3$ and $LaF_3$ as a function of wavelength from Ref. [16]

refractive indices in the wavelength range from 0.2 to 2.0 $\mu$m for $LaF_3$, $NdF_3$ and $CeF_3$ are plotted in Fig. 1.4 from Ref. [16].

# Chapter 2

# Sample Preparation

The preparation of the rare-earth fluoride/semiconductor samples involves two basic steps: substrate cleaning and fluoride thin film deposition. The surface of semiconductors as received from manufacturers are generally contaminated with carbon compounds, silicon oxides and native oxides. For epitaxial growth of high quality films, these contaminants must be removed. In this chapter, we describe the procedures for the sample preparation and discuss the effect of atomic hydrogen etching on the surface of GaAs and InP wafers.

## 2.1 Substrate Cleaning

The thin film samples ($< 10$ nm) for surface analysis by photoemission were prepared at the Synchrotron Radiation Center in Wisconsin. The (111) and (100) oriented GaAs and InP wafers were etched in a concentrated $H_2SO_4$ solution to remove native oxides. They were rinsed with deionized water and blown dry with $N_2$ before being inserted in the UHV analysis chamber. The wafers were 400 to 500 $\mu$m thick and 1 to 2 cm$^2$ in area.

The thick film samples ($> 10$ nm) used in the X-ray scattering and diffraction experiments were prepared in our lab at the University of British Columbia. The GaAs and InP wafers used for the samples were 2 in. diameter wafers, 400 to 500 $\mu$m thick. The wafers were cleaved into 6 pie shaped pieces. The GaAs and InP wafers were first rinsed in concentrated HF solution for 1 min. to remove any residual $SiO_2$ on the surface. $SiO_2$

on the surface is believed to be residual from the chemical polishing process at manufacturer [18]. They were next rinsed in deionized water and oxidized in a UV ozone reactor. The ozone reactor consisted of a 60 W mercury UV lamp and a sample holder placed 1.5 in. away from the lamp [19]. Growth of oxide by UV ozone treatment helps remove carbon contaminants from the surface. The substrates were subsequently inserted in a UHV chamber with a typical background pressure of 5 to $10 \times 10^{-10}$ mbar.

The oxide on the GaAs and InP wafers was removed by atomic hydrogen etching in the vacuum chamber. The atomic hydrogen etching is one of the substrate cleaning methods for molecular beam epitaxy. A *prepurified* grade $H_2$ gas (99.99%) was used for the etching. The hydrogen pressure during the etching was $1 \times 10^{-6}$ torr. The hydrogen molecules were dissociated thermally with a resistively heated tungsten filament placed at about 5 cm from the substrate surface. The temperature of the filament was between 1800 and 2000°C. The substrate was heated to 300°C by the substrate heater during etching. The temperature of the substrate was measured by a thermocouple situated between the heater and the substrate. The oxides were removed in approximately 10 min. at this condition as verified by reflection high energy electron diffraction (RHEED) [27], but the substrates were further cleaned by atomic hydrogen for approximately 20 min. in order to remove residual carbon. The secondary ion mass spectroscopy (SIMS) study of the hydrogen etched GaAs wafers showed that the amount of carbon contaminants on the wafers decreased with increasing hydrogen etching time [27].

## 2.2 Fluoride Film Growth

The rare-earth trifluoride films were grown by evaporation from a high purity (99.9 %) crystalline powder. For the thin film samples used in the photoemission experiments, the fluoride powder was evaporated from a $3 \times 1$ cm$^2$ Ta boat, placed 10 cm from the

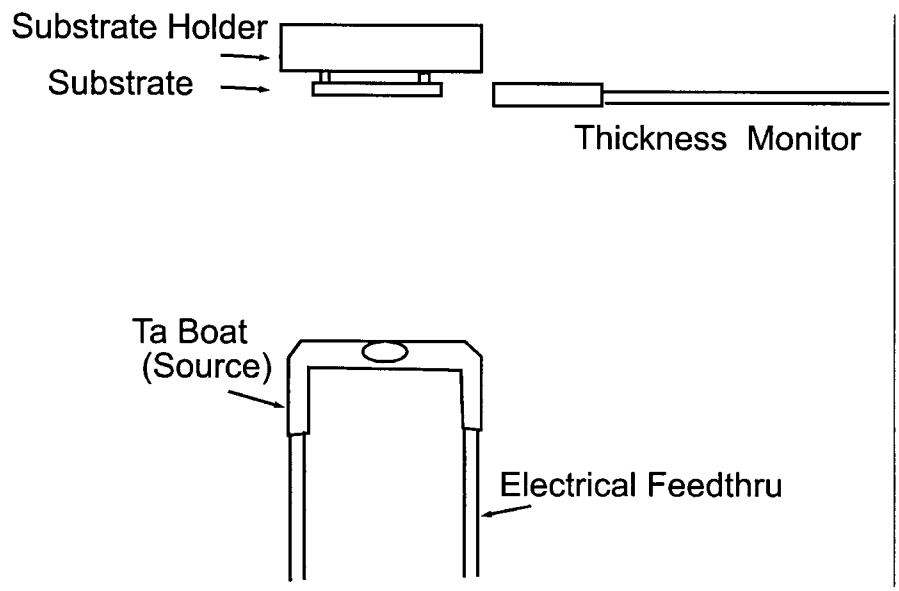


Figure 2.5: Schematic illustration of the fluoride evaporation setup for thin film samples used in the photoemission experiments carried out at the Synchrotron Radiation Center in Wisconsin.

sample ( see Fig. 2.5 ). The Ta boat is attached to a feedthrough and heated resistively to the melting temperature of the fluoride (1493°C for $LaF_3$ and 1140°C for $ErF_3$). The pressure during evaporation was approximately $1 \times 10^{-7}$ mbar. The sample was not independently heated during the evaporation, although the close proximity to the hot evaporator caused some unintentional heating. The film thickness ranged from 0.5 to 2 nm as measured by the thickness monitor located beside the sample.

The thick film samples (10–400 nm) were prepared by molecular beam epitaxy in our lab at the University of British Columbia. The schematic illustration of the growth setup is shown in Fig. 2.6. The evaporation was done from a high temperature effusion cell (VG-6HT) with a tungsten crucible. The semiconductor substrates were placed on a heated stage in a UHV chamber with a typical background pressure of $1 \times 10^{-9}$ mbar. The substrate temperature during growth was 600±20° C for GaAs and 400±20°C for InP as measured by a thermocouple situated between the heater and substrate. Typical

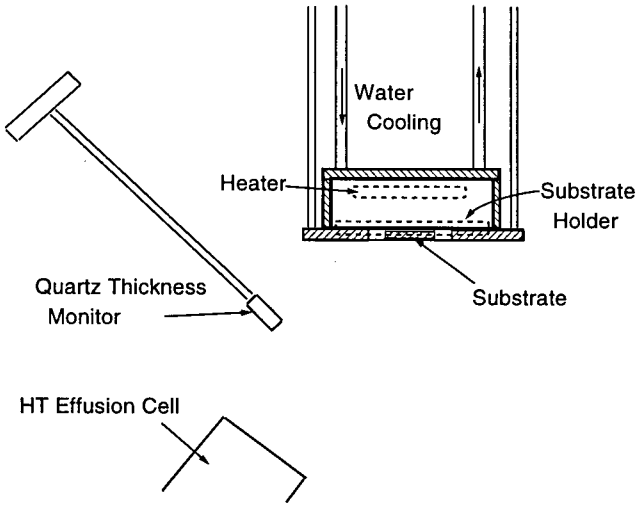


Figure 2.6: Schematic illustration of the molecular beam epitaxy setup for thick film samples.

pressure during evaporation was $1 \times 10^{-7}$ mbar.

Although the Ta boat setup costs less and is easy to implement than the effusion cell setup, there are several advantages for using an effusion cell. One of the advantages for using an effusion cell over a Ta boat is that the effusion cell allows a deposition over a larger area than the Ta boat does. The deposition of a sample area up to 2 in. in diameter circle is possible with an effusion cell whereas the sample size is limited to about 1/2 in. in diameter circle. The effusion cell also allows us a better control of the source temperature than the Ta boat setup, hence a better control of the flux of the fluoride molecular beam.

## 2.3 Atomic Hydrogen Etching

The effect of hydrogen etching on the surface of GaAs and InP wafers was studied by UV photoemission spectroscopy. We used photoemission to determine whether the atomic hydrogen etching removes oxides, carbon contaminants and other chemical species on

the surface. The basic principle of photoemission spectroscopy is described in Chapter 3. Photoemission experiments were performed at the Canadian Synchrotron Radiation Facility at Synchrotron Radiation Center at the University of Wisconsin-Madison, using a grazing-incidence grasshopper monochromator . The combined resolution of the analyser and the monochromator is 0.2 eV. The atomic hydrogen cleaning for the photoemission experiments was carried out in a similar manner to the MBE substrates. Typical base pressure in the analysis chamber was $1 \times 10^{-9}$ mbar. High purity $H_2$ gas (99.99%) was used for the etching. The hydrogen pressure during the etching was $1 \times 10^{-6}$ torr. The hydrogen molecules were dissociated thermally with a resistively heated tungsten filament placed at about 3 cm from the substrate surface. The temperature of the filament was between 1800 and 2000°C. The substrate was not intentionally heated, but has been heated by radiation from the hot filament.

### 2.3.1 GaAs wafers

Photoemission spectra of the Ga 3d and As 3d core levels from a GaAs(111) wafer (as-received) before the atomic hydrogen etching are shown in Fig. 2.7. The spectra taken before the atomic hydrogen etching show chemically shifted components separated by 1.2 eV in the Ga 3d core level and 2.9 eV in the As 3d core level. The components are commonly observed in oxidized GaAs [20, 21, 22]. The peaks at the lower binding energy are associated with the Ga-As bonds of the bulk GaAs and the peaks at the higher binding energy, with the surface oxides, $Ga_2O_3$ and $As_2O_3$ [20, 21, 22].

Photoemission spectra of the Ga 3d and As 3d core levels from a GaAs(111) wafer after an exposure to $3 \times 10^{16}$ $cm^{-2}$ of atomic hydrogen are shown in Fig. 2.8. The calculation of the hydrogen exposure is described in Appendix A. The intensities of oxide components $Ga_2O_3$ and $As_2O_3$ are no longer detected or they are below the noise level which is 1 % of the intensity before atomic-H etching.

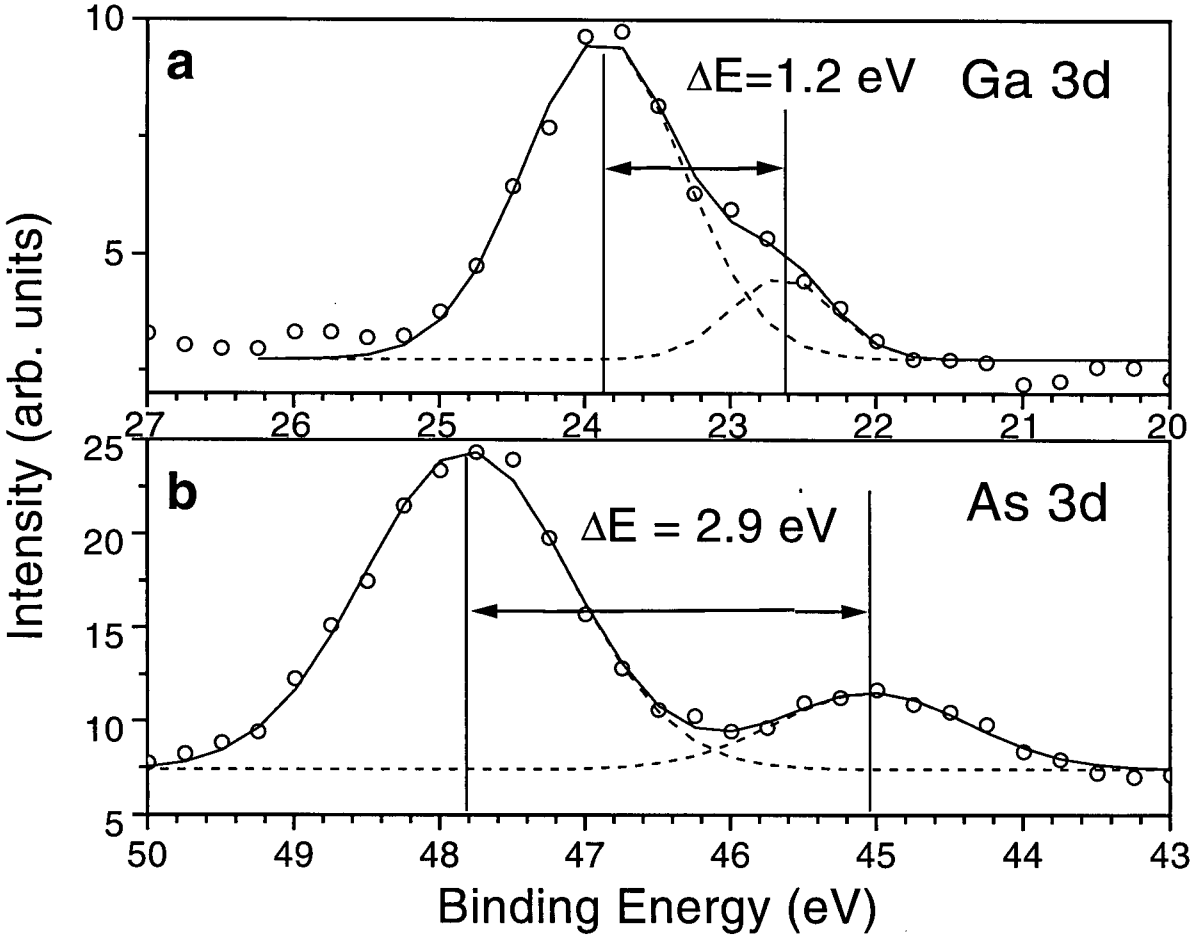


Figure 2.7: Photoemission spectra of the (a) Ga 3d and (b) As 3d core levels from a (111)B GaAs wafer before atomic H-etching showing two components for each Ga 3d and As 3d core levels, separated by 1.2 and 2.9 eV, respectively. The component at the lower binding energy corresponds to the Ga-As bonds in the bulk GaAs. The component at the higher binding energy is associated with the chemical bonds in the surface oxides. The solid lines are fits of a Gaussian function to the data.

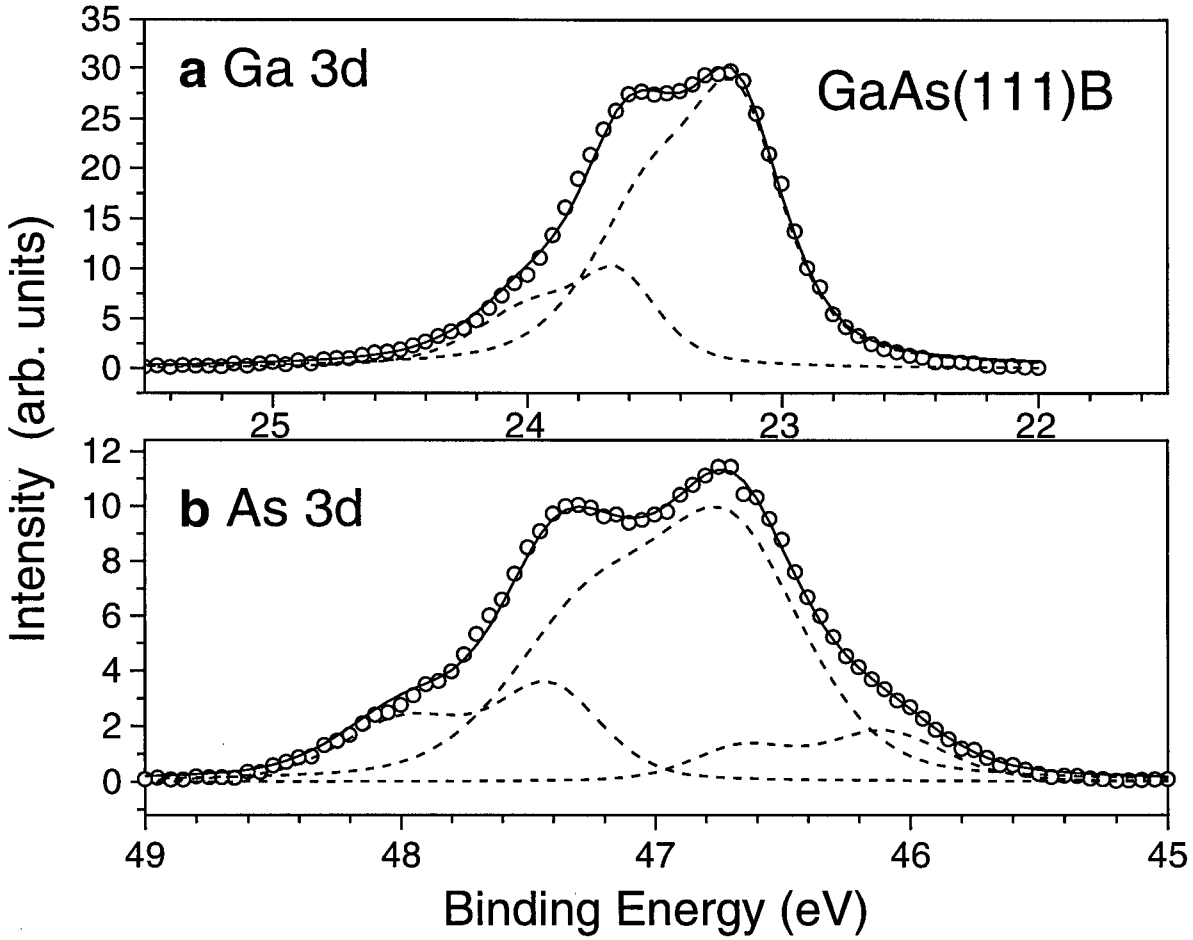


Figure 2.8: Photoemission spectra of the (a) Ga 3d and (b) As 3d core levels obtained from a (111)B GaAs wafer after atomic hydrogen etching. The solid lines are fits of a mixed Gaussian-Lorentzian function to the data.

To resolve the components present in the spectra, the Gaussian-Lorentzian mixed function of the form [23]:

$$f(\Gamma,\eta,x) = \frac{\eta}{1+(\frac{x-x_0}{0.5\Gamma})^2} + (1-\eta)\ \exp[-(\frac{x-x_0}{b\Gamma})^2] \tag{2.1}$$

is fitted to the data as shown by solid lines in Fig. 2.8. In this expression, $x$ is the binding energy, $\Gamma$ is the width of the function, $b = (1/2)\sqrt{\ln 2} = 0.60056$ and $\eta$ is the Lorentzian fraction. The basic shape of the photoemission peak is Lorentzian associated with the finite core hole life time. The Gaussian function represents other factors such as instrumental broadening and phonon broadening. In the spectrum of the Ga 3d core level (Fig. 2.8 (a)), two components separated by 0.4 eV are resolved. The chemical shifted components are also observed by Pianetta *et al.* [22]. The component at lower binding energy is GaAs bonds in the bulk GaAs and the component at higher binding energy corresponds to the Ga-O bonds of the chemisorbed oxygen.

In the As 3d core level spectrum shown in Fig. 2.8 (b), three components are resolved. The highest intensity peak reveals the Ga-As bonds in the bulk GaAs. The component shifted by 0.7 eV toward higher binding energy is associated with a single As-O or As-OH bond of the As surface atoms [20]. Surface As-H bond produces a smaller chemical shift (0.3 eV) and may also be present [24]. The component shifted by 0.6 eV towards lower binding energy is the surface component of Ga-As bonds.

The thicknesses of oxide and carbon contaminant layers etched by the atomic hydrogen exposure of $3 \cdot 10^{16}$ cm$^{-2}$ were determined from the ratio of photoemission intensities before and after etching. They were 0.9 nm and 0.6 nm respectively. Corresponding efficiencies of the atomic hydrogen etching are 0.3 nm/($10^{16}$ H atoms cm$^{-2}$) for the oxide layer and 0.2 nm/($10^{16}$ H atoms cm$^{-2}$) for the carbon layer respectively. A detailed description of the calculation is included in Appendix B. It has been shown by laser light scattering [27] that the surfaces of atomic hydrogen etched GaAs wafers were smoother

than the surface of the thermally desorbed GaAs wafers.

### 2.3.2 InP wafers

The effect of the atomic hydrogen etching as well as the HF etching on the surface of InP wafers was studied. Photoemission spectra from a (111)B InP wafer as received (a), after the HF etching (b) and after atomic hydrogen etching (c) are shown in Fig. 2.9. In the photoemission spectrum of the as-received InP wafer, silicon (Si) 2p core levels in addition to the phosphorus (P) 2p core levels are observed. Hence, the surface of the InP wafer is contaminated with Si, or more likely, $SiO_2$. To further examine the presence of $SiO_2$, the total electron yield spectra of the InP wafer before and after the HF etching are obtained and shown in Fig. 2.10. An absorption peak at 105 eV corresponds to the Si L edge in $SiO_2$ and the smaller peak at 130 eV corresponds to the phosphorus (P) L edge.

The photoemission spectrum of the InP wafer after being removed from the analysis chamber and being etched in concentrated HF for 1 min is shown in Fig. 2.9 (b). After this treatment the Si 2p core level is missing from the photoemission spectrum. The HF etching evidently removed the $SiO_2$ contamination. Similarly, the Si L edge absorption in the total electron yield spectrum of the InP wafer was not detected after the HF etching (Fig. 2.10 (b)). The intensity of the phosphorus (P) L edge in Fig. 2.10 (b) has increased by a factor of 2.5. Furthermore, the P 2p core levels after the HF etching (Fig. 2.9 (b)) has also increased. This suggests that the $SiO_2$ contamination covers the wafer rather uniformly. We believe that the $SiO_2$ contamination is a residue from the chem-mechanical process used to polish the wafers produced by an improper polishing procedure [18]. If the $SiO_2$ contamination were in the form of particles, the photoemission intensity of the substrate peak would not change so dramatically after HF etching, given that the escape depth of the 50eV photoelectrons is on the order of 1 nm.

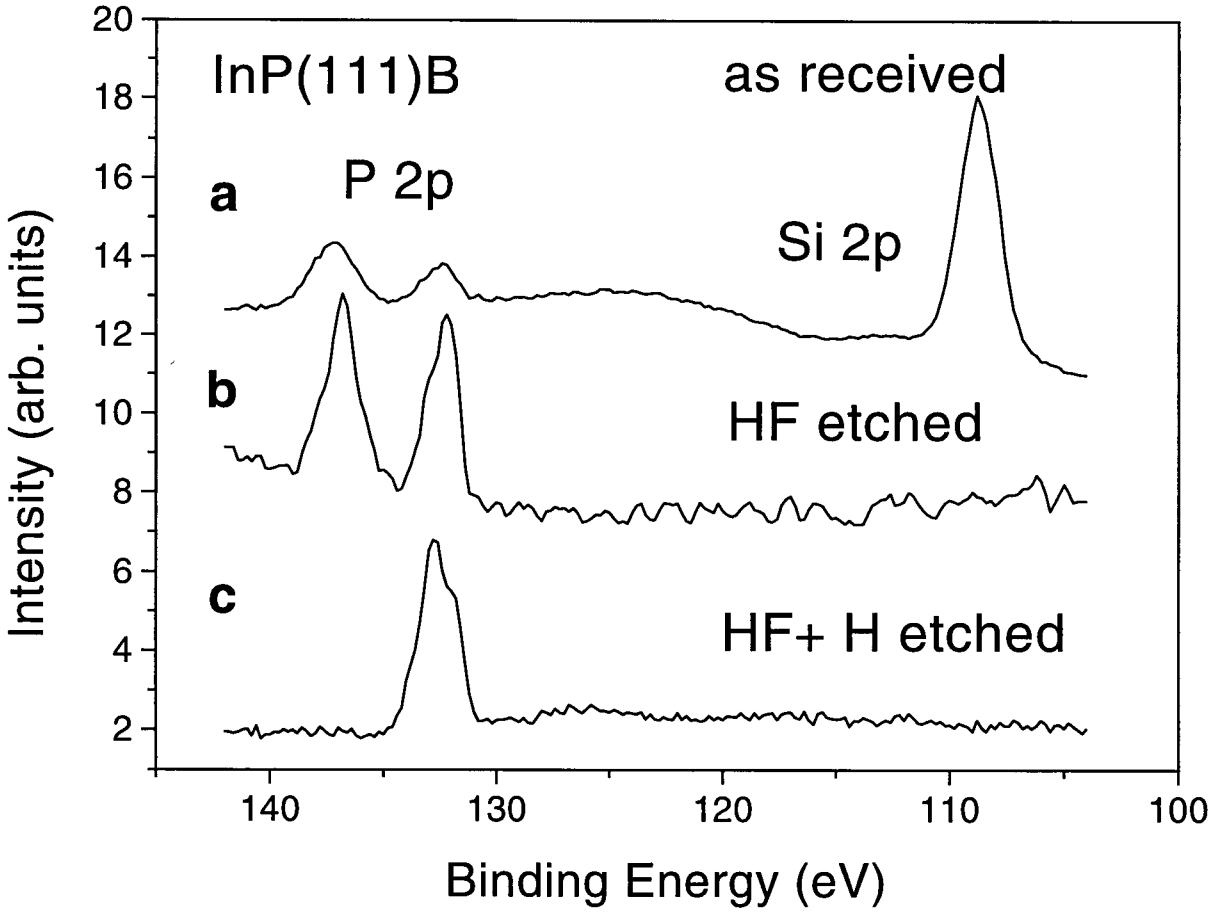


Figure 2.9: Photoemission spectra from a (111)B InP wafer excited at a photon energy of 180 eV: (a) as-received, (b) after HF etching and (c) atomic hydrogen etching. All three curves show the P 2p core level; curves (a) and (b) show a chemically shifted P 2p core level (P-O bonding); curve (a) also shows the Si 2p core level.

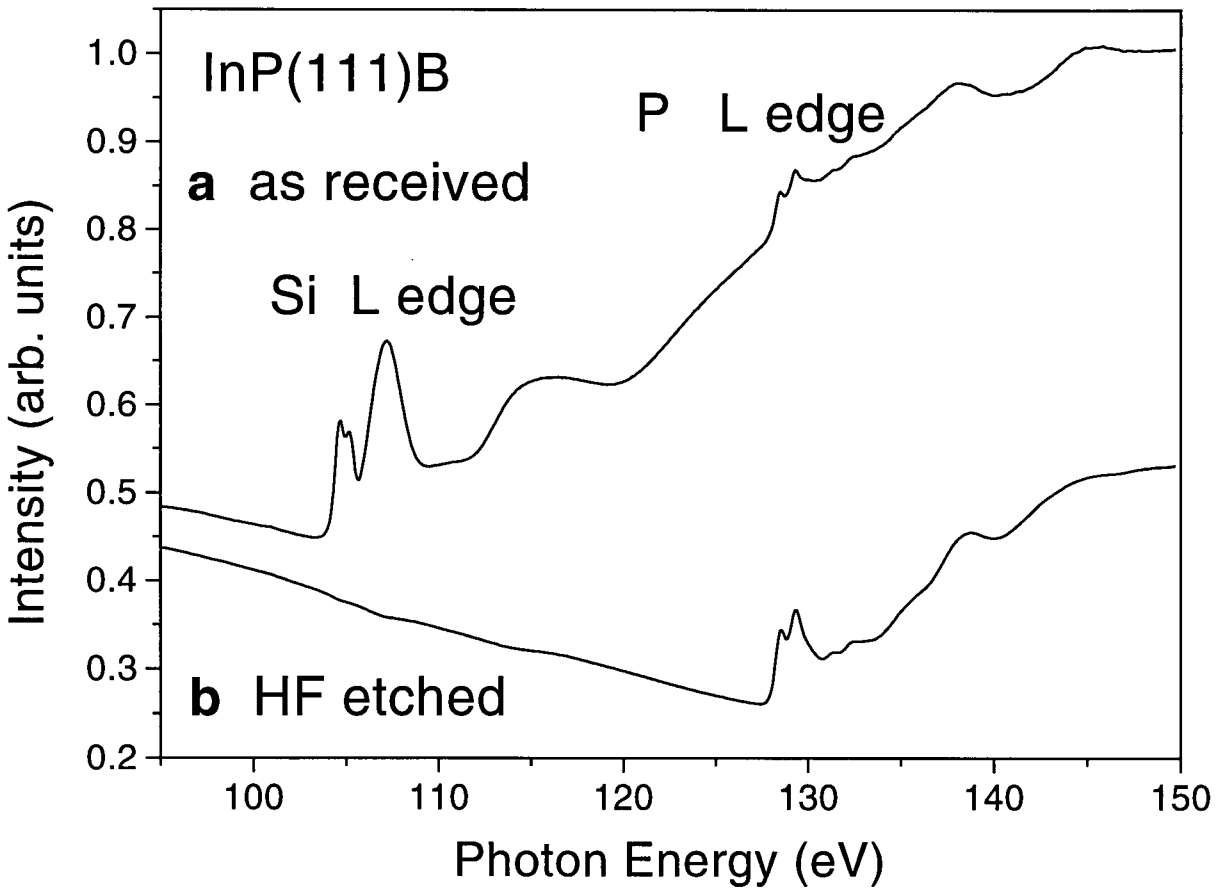


Figure 2.10: Total electron yield spectra from a (111)B InP wafer: (a) as-received and (b) after HF etch. Both the silicon L edge and phosphorous L edge are observed in spectrum (a), while only the phosphorous L edge is detected in spectrum (b).

The photoemission spectrum of the P 2p core levels for the as-received InP wafer in Fig. 2.9 (a) shows a component chemically shifted to a higher binding energy corresponding to the surface oxide. As can be seen in the spectrum in Fig. 2.9 (b), the surface oxide is reduced but not removed by the HF etch. The photoemission spectrum taken after HF etching followed by an exposure to $9 \times 10^{16}$ cm$^{-2}$ of atomic hydrogen is shown in Fig. 2.9 (c). The oxide component of the P 2p core levels are not detected. This shows that the hydrogen etching removed the phosphorus oxide.

The thicknesses of $SiO_2$ removed by HF etch and the oxide+carbon layer removed by atomic hydrogen are estimated as 0.9 and 0.4 nm respectively from the ratio of the photoemission signals. The corresponding efficiency of the atomic-H etching is 0.04 nm/($10^{16}$ H atoms cm$^{-2}$) for the oxide+carbon layer. The details of the calculations are described in Appendix B. The difference in efficiency between the InP wafer and the GaAs wafer (0.3 nm/($10^{16}$ H atoms cm$^{-2}$)) probably comes from the failure to estimate the atomic hydrogen exposure required to remove 0.4 nm of oxide+carbon layer in the InP wafer case. The actual atomic hydrogen exposure that removed 0.4 nm of oxide+carbon layer may have been less than total exposure $9 \times 10^{16}$ cm$^{-2}$. The lower efficiency for the InP substrate is not due to the presence of $SiO_2$ particles after HF etching, since the SIMS experiment showed that the atomic-H etching does not remove $SiO_2$.

The C 1s core level spectra from a (111)B InP wafer before and after the atomic hydrogen etching are shown in Fig. 2.11. The spectrum in Fig. 2.11 (a) was taken after the HF etching and the spectrum in Fig.2.11 (b) was taken after the HF etching followed by the exposure to $3 \times 10^{16}$ cm$^{-2}$ of atomic hydrogen. The intensity ratio of the C 1s core levels in Fig. 2.11 before and after hydrogen etching is estimated to have an upper limit of $I_{C1sf}/I_{C1si} < 0.05$. Therefore the carbon contamination was reduced by factor of at least twenty by atomic hydrogen etching. Other photoemission experiments not described here showed that atomic hydrogen etching did not remove the $SiO_2$, consistent

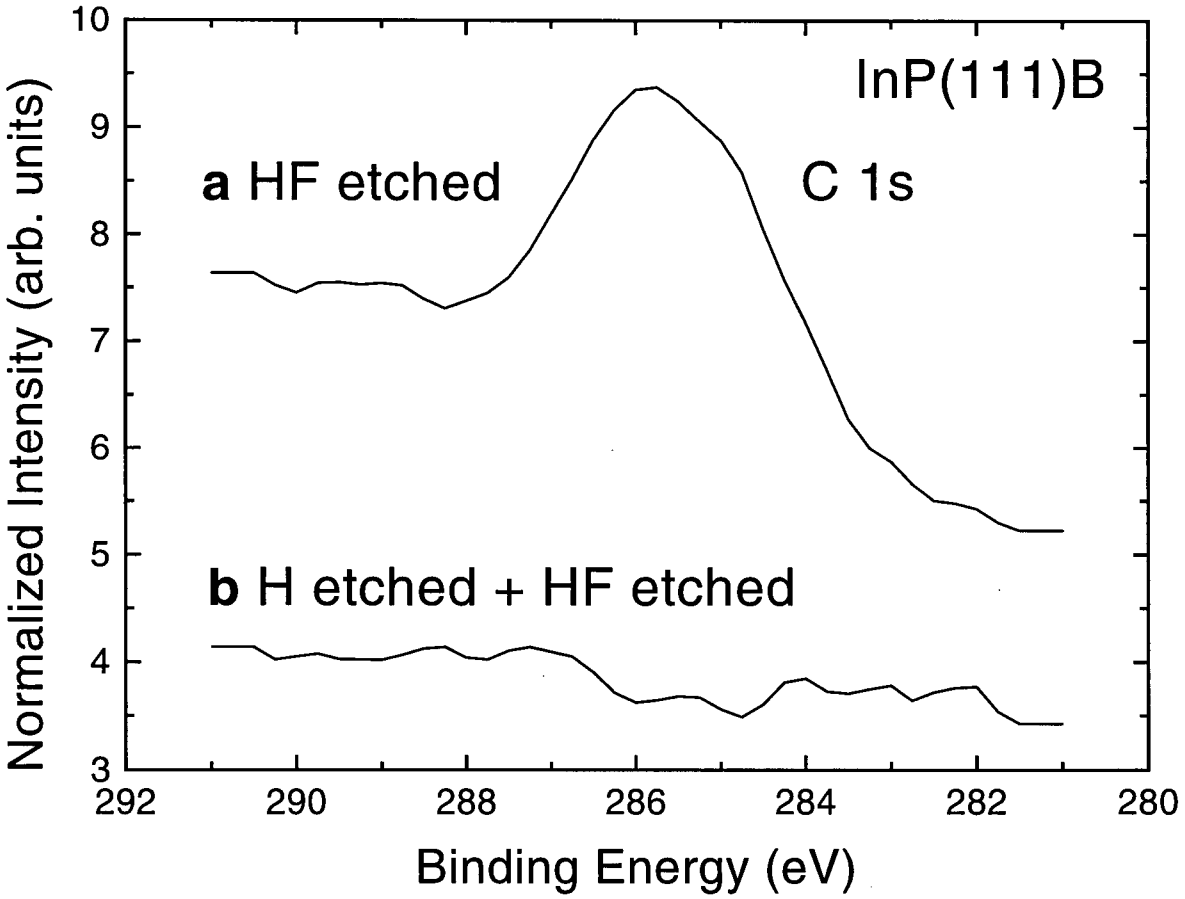


Figure 2.11: Carbon 1s photoemission spectra for a (111)B InP wafer: (a) after an HF etch and (b) after an HF etch followed by an atomic-H etching which removed 75 % of the carbon.

with the SIMS measurements of the atomic hydrogen etched GaAs wafers in Ref. [27]. Although the photoemission measurements of C and $SiO_2$ contamination were carried out on InP substrates, we expect similar results for the GaAs substrates.

### 2.3.3 Summary

Photoemission results showed that the atomic hydrogen etching effectively removed the surface oxides and carbon contaminants from the GaAs and InP wafers. The study also showed that layers of $SiO_2$ are present on the as-received wafers from the manufacturers. The $SiO_2$ layers can be removed by HF etching as shown by PES.

The laser light scattering study of the atomic hydrogen etching [27] showed that the surface roughness of the wafer whose oxide was removed by thermal desorption was greater than the surface roughness of the wafer cleaned by atomic hydrogen etching. The thermal desorption roughens the surface whereas the hydrogen cleaning does not. Furthermore, the SIMS study of the atomic hydrogen etched GaAs wafers [27] showed that the oxide removal by thermal desorption does not remove the carbon contaminants. We conclude that the atomic hydrogen etching is the best method for the substrate preparation for the fluoride film growths.

# Chapter 3

## Initial Stage of Fluoride Film Growth

The quality of epitaxial thin films is often determined at the initial stages of the film growth. In this chapter, the growth process of the rare-earth fluoride films on III-V semiconductors at the initial stage of growth is studied. For this purpose, samples with film of thickness less than 10 nm are prepared. A series of anneals is performed on the samples. After each annealing, the electronic structures at the surfaces and interfaces are examined by photoemission spectroscopy.

The first step of fluoride film growths involves the physisorption of fluoride molecules (e.g. $CaF_2$ and $LaF_3$ molecules) onto the substrate surface. At this stage, the fluoride molecules have not necessary formed chemical bonds at the film/substrate interface. The annealing provides the energy for the fluoride molecules to rearrange themselves and to form crystals. Depending on the film and substrate surface energies and also on the film/substrate interface energy, the film can form islands or wet the substrate surface as illustrated in Fig. 3.12. Further annealing can result in the reevaporation of the fluoride molecules.

In this study, we explore the wetting between the rare-earth fluoride films grown on III-V semiconductors and the substrate surfaces by angle dependent photoemission spectroscopy. The re-evaporation caused by high temperature annealing is also studied by angle dependent spectroscopy. The wetting phenomena of a film on a substrate can be understood thermodynamically [31]. Consider a system of a film on a substrate in which the film/air interface makes a contact angle $\theta$ with the substrate/air interface

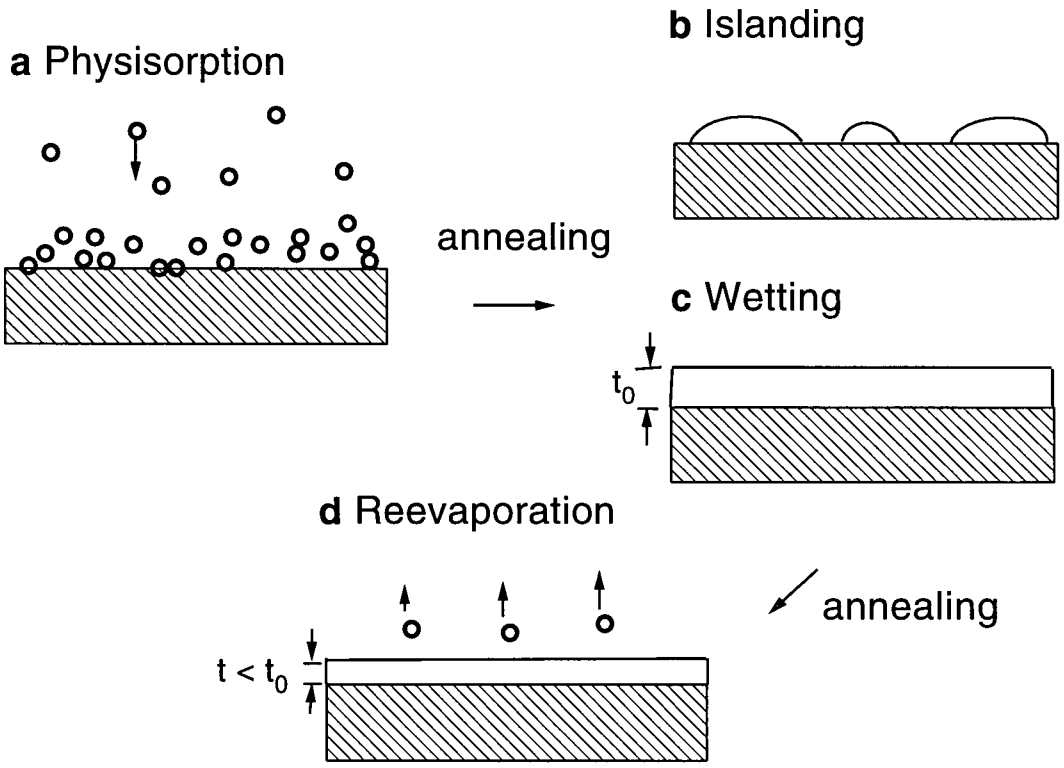


Figure 3.12: Schematic illustration of growth process in thin film evaporation with subsequent high temperature annealing. The first step is the physisorption of the molecules onto the substrate (a). The annealing can cause the film to form islands (b) or to wet the substrates (c). The subsequent annealing can result in the reevaporation of the molecules (d).

as shown in Fig. 3.13. The interface free energies are defined as $\gamma_f$ for film/air, $\gamma_s$ for substrate/air and $\gamma_{sf}$ for film/substrate interfaces. The change in surface free energy $\Delta G$ accompanying a small displacement of the film such that the change in area of substrate covered $\Delta A$, is:

$$\Delta G = \Delta A(\gamma_{sf} - \gamma_s) + \Delta A\gamma_f cos(\theta - \Delta\theta) \tag{3.2}$$

At equilibrium:

$$\lim_{\Delta A \to 0} \frac{\Delta G}{\Delta A} = 0 \tag{3.3}$$

and:

$$\gamma_{sf} - \gamma_s + \gamma_f \cos\theta = 0 \tag{3.4}$$

The condition for wetting is given by:

$$\gamma_s > \gamma_{sf} + \gamma_f \tag{3.5}$$

The surface energy of fluorides are generally lower than that of covalent semiconductors because of the ionic bondings in fluorides. The surface energy of fluorides such as $CaF_2$ and $BaF_2$ ranges between 0.3 and 0.5 J/m$^2$ [32, 33], whereas that of semiconductors such as Si and GaAs ranges between 0.8 to 3.2 J/m$^2$ [34]. The surface energy of a material is different for each crystallographic surface. We expect the film/substrate interface free energy $\gamma_{sf}$ to be lower than either film/air $\gamma_f$ or substrate/air $\gamma_s$ interface energy. Since $\gamma_{semiconductor} > \gamma_{fluoride}$, if we neglect the film/substrate interface energy, the condition for wetting is satisfied. Therefore we expect a complete coverage of semiconductor substrates by fluoride films.

## 3.1 Photoemission Spectroscopy

Photoemission spectroscopy reveals the electronic structures of materials or their occupied density of states. The synchrotron radiation is used as the photon source because of

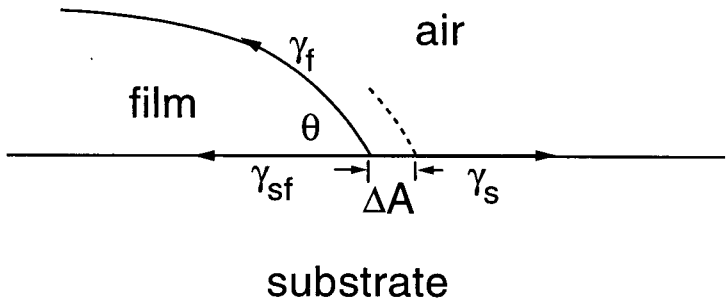


Figure 3.13: Schematic illustration of a system of a film on a substrate. The interface free energies are defined as $\gamma_f$ for film/air, $\gamma_s$ for substrate/air and $\gamma_{sf}$ for film/substrate interfaces.

its energy tunability and strong intensities. Photoemission experiments were performed at the Synchrotron Radiation Center at the University of Wisconsin-Madison, using a grazing incidence grasshopper monochromator. The photon energy ranged from 100 to 200 eV (soft X-rays), since the photoemission experiments performed at this energy range have maximum sensitivity for the material systems of interest here. The electron escape depths in this energy range lies between 0.5 to 3 nm. The combined resolution of the analyser and the monochromator is 0.2 eV.

One often uses a three step model to represent the photoemission process. It consists of the optical transition (1), the transport to the surface (2) and the transmission through the surface (3). The kinetic energy $E_k$ of the outgoing electron is given by:

$$E_k = h\nu - E_b - \phi \tag{3.6}$$

where $h\nu$ is the photon energy, $E_b$ the electron binding energy and $\phi$ the work function.

The tunable photon energy allows data to be collected in several modes. *Energy*

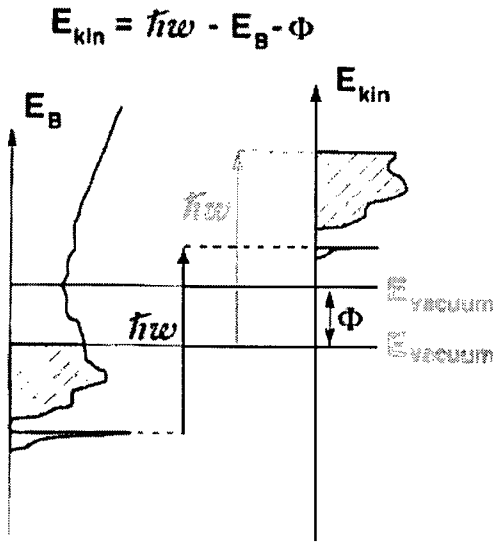


Figure 3.14: Schematic illustration of occupied density of states and corresponding energy distribution curve revealing the bound valence band and a narrower core level, obtained by photoemission.

*distribution curves* (EDC) are obtained to study the valence band and the core level structures of the fluoride/semiconductor samples. EDC is obtained by scanning the kinetic energy of the photoelectrons with photon energy fixed. It maps the occupied density of states as illustrated in Fig. 3.14. Absorption edges of the deep lying levels are studied by *total electron yield* measurements in which the photon energy is scanned while the intensity of the total emitted photoelectrons is measured.

The film coverage at the initial stage of the film growth is determined by *angle dependent photoemission spectroscopy.* The fraction of the substrate area $\gamma$, covered by a film of thickness $t$ is determined from the film/substrate photoemission intensity ratio given by [29]:

$$\frac{I_f(\theta)}{I_s(\theta)} = \frac{I_f^\infty}{I_s^\infty} \frac{\gamma[1 - e^{-t/\lambda(E_f)\sin\theta}]}{(1-\gamma) + \gamma e^{-t/\lambda(E_s)\sin\theta}]} \tag{3.7}$$

where $I_{f,s}(\theta)$ are the intensities of the film (f) and the substrate (s) signals at the escape angle $\theta$, $I_{f,s}^\infty$ are the intensities from an infinite film (f) and an infinite substrate (s),

$\lambda(E_{f,s})$ are the inelastic mean free path in the film at the kinetic energy of the film peak $E_{f,s}$. The fractional coverage $\gamma$ and film thickness $t$ are obtained by fitting Eqn. 3.7 to the plot of $I_f(\theta)/I_s(\theta)$ vs. $1/\sin\theta$.

The localized 4f levels of rare-earth ions in the rare-earth trifluorides are determined using *resonant photoemission spectroscopy.* They are otherwise difficult to locate because of their overlap with fluorine valence bands. An enhancement of photoemission occurs when there are two or more emission processes having the same final states. For example, in the $4d$–$4f$ transitions in the Er ions in $ErF_3$, one of the autoionization processes is:

$$4d^{10}4f^{11} \rightarrow 4d^{9}4f^{12} \rightarrow 4d^{10}4f^{10} + e^{-} \tag{3.8}$$

It has the same initial and final state as the direct emission process:

$$4d^{10}4f^{11} \rightarrow 4d^{10}4f^{10} + e^{-} \tag{3.9}$$

When the photon energy has a same energy as the transition $4d^{10}4f^{11} \rightarrow 4d^{9}4f^{12}$, a resonance occurs and there will be an enhancement of the photoemission because of the extra autoionization process in addition to the direct process. A series of resonant scans are used to locate the positions of the localized 4f levels. It was also used to study the valencies of Er ions at the interface of $ErF_3$/GaAs(111) samples. For $ErF_3$, the resonance is observed near the 4d absorption edge . The Er 4f levels in the Er ions are obtained by taking the difference between the valence band spectra taken at the resonant photon energy (resonance) and at the photon energy just below the resonant photon energy (non-resonance).

## 3.2 Surface Morphology

Photoemission spectra of thin $ErF_3$ and $LaF_3$ films grown on the (111) surface of GaAs and InP substrates are shown in Fig. 3.15, 3.16 and 3.17. The photoelectron intensities

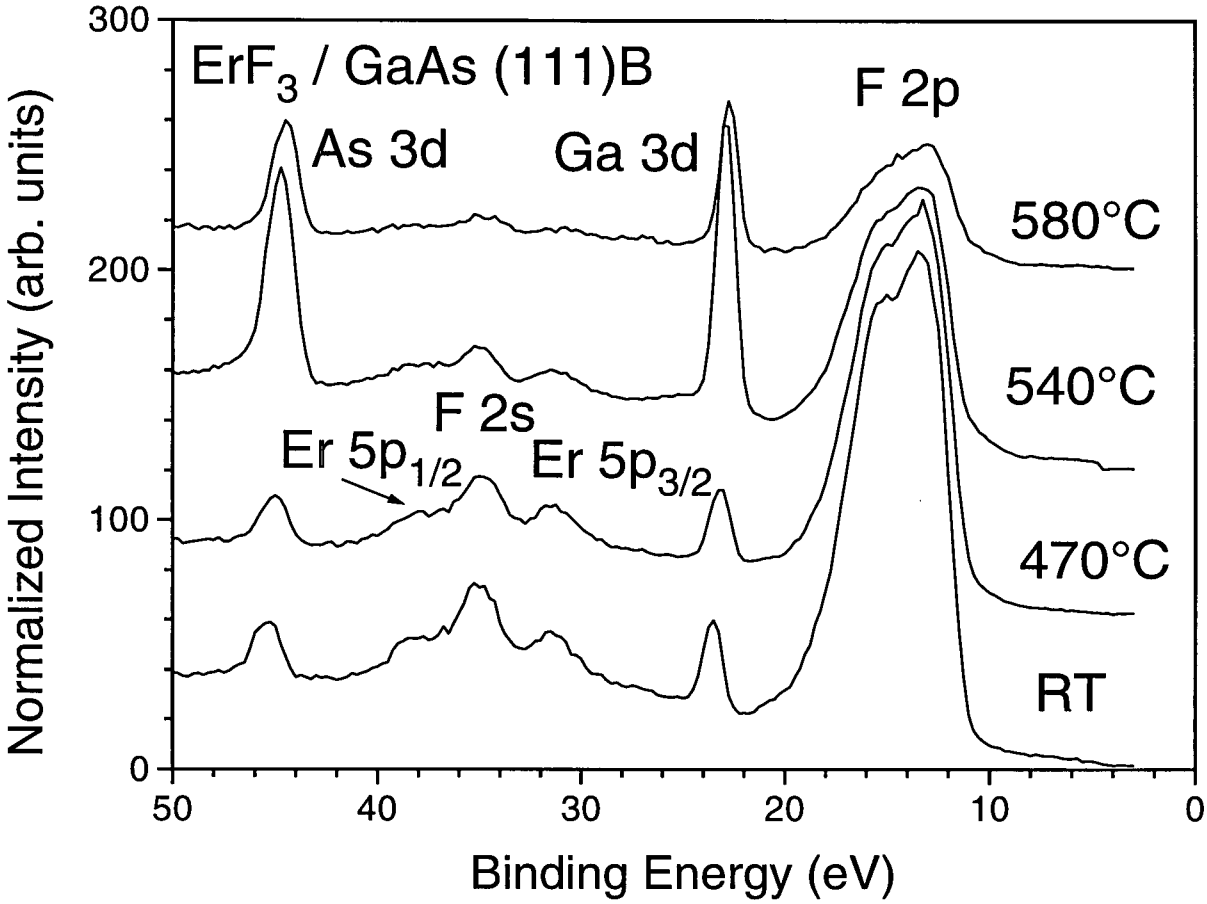


Figure 3.15: Photoemission spectra of an $ErF_3$/GaAs(111)B sample taken after the indicated annealing temperatures showing the film and the substrate peaks.

were normalized using the intensities of the incident photons. The film and the substrate peaks are observed as indicated in the figures. The intensities of the film peaks decreased while the substrate peak intensities increased with increasing annealing temperature for all the samples. Above about 500°C, sample temperatures were measured by infrared pyrometer with an estimated accuracy of ±20°C. Sample temperatures below 500°C were estimated by an extrapolation from high temperatures of a log-log plot of the temperature measured by pyrometer as a function of the heater current [30].

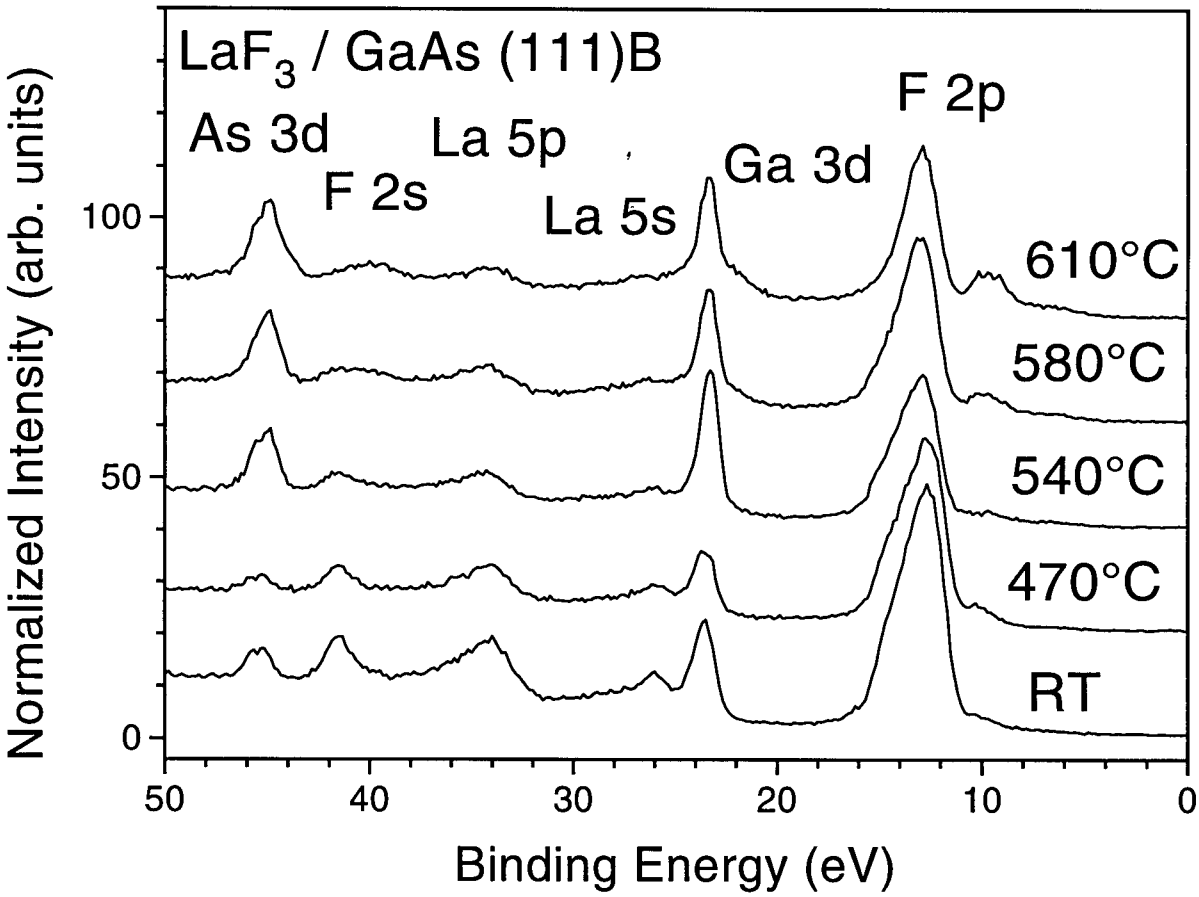


Figure 3.16: Photoemission spectra of a $LaF_3$/GaAs(111) sample taken after the indicated annealing temperatures.

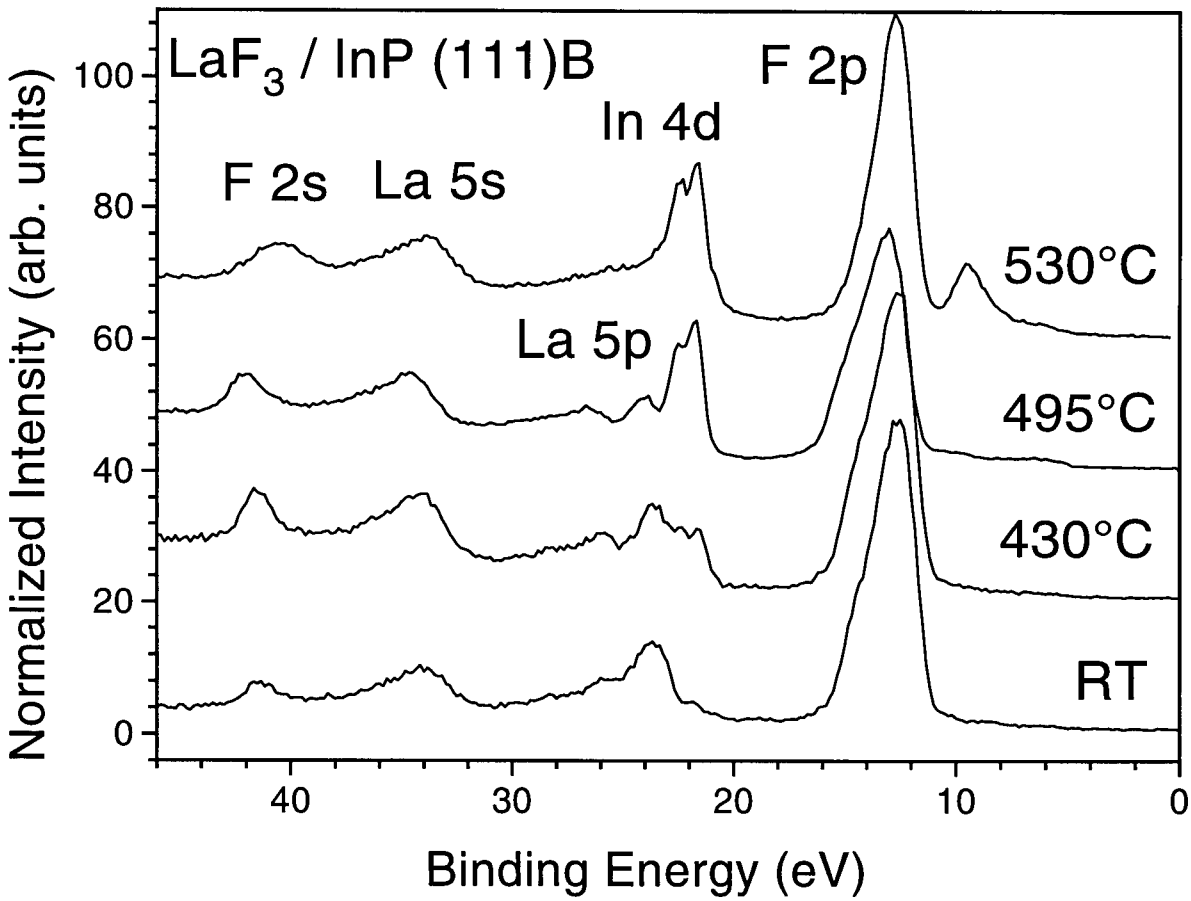


Figure 3.17: Photoemission spectra of the $LaF_3$/InP(111)B sample taken after the indicated annealing temperatures.

Table 3.3: Film/substrate photoemission peak intensity ratios for thick film and bare substrate obtained from measurements.

| | | |
|---|---|---|
| $ErF_3$/GaAs(111)B | $I^{\infty}_{F2p}/(I^{\infty}_{Ga3d} + I^{\infty}_{As3d})$ | 1.7 |
| $LaF_3$/GaAs(111)B | $I^{\infty}_{F2p}/I^{\infty}_{As3d}$ | 3.5 |
| $LaF_3$/InP(111)B | $I^{\infty}_{F2p}/I^{\infty}_{In4d}$ | 1.6 |

Angle dependent spectroscopy was performed to obtain the film thickness and the fractional coverage. The film/substrate photoemission intensity ratios $I_f(\theta)/I_s(\theta)$ as a function of $1/\sin\theta$ for the $ErF_3$/GaAs(111)B, $LaF_3$/GaAs(111)B and $LaF_3$/InP(111)B samples are shown in Fig. 3.18. The annealing temperature for each sample is indicated in the figure. The film thickness $t$ and the fractional film coverage $\gamma$ are determined using the the film/substrate intensity ratio in Eqn. 3.7. The calculated intensity ratio are shown by solid lines in Fig. 3.18. The values of intensity ratios $I^{\infty}_L/I^{\infty}_S$ for the infinite materials used in the calculations were determined from the intensities of a thick film and a bare substrate. They are listed in Table 3.3. An inelastic mean free path of $\lambda = 1$ nm at kinetic energy of 50 eV [25] was used for the fluoride films. The horizontal error bars in the figure correspond to the angular range subtended by the photoelectron detector.

The film thickness and the fractional coverage obtained from the angle dependent scans for each sample are summarized in Table 3.4. The fractional coverage obtained from the angle dependent scans are consistent with the complete coverage of the substrates by the fluoride films upon deposition. As the samles are annealed, the film thickness decreases. Up to the monolayer coverage *i.e.* the thickness $\sim$ 0.3 nm, the samples stay covered. The result for the $LaF_3$/InP sample shows that the further annealing

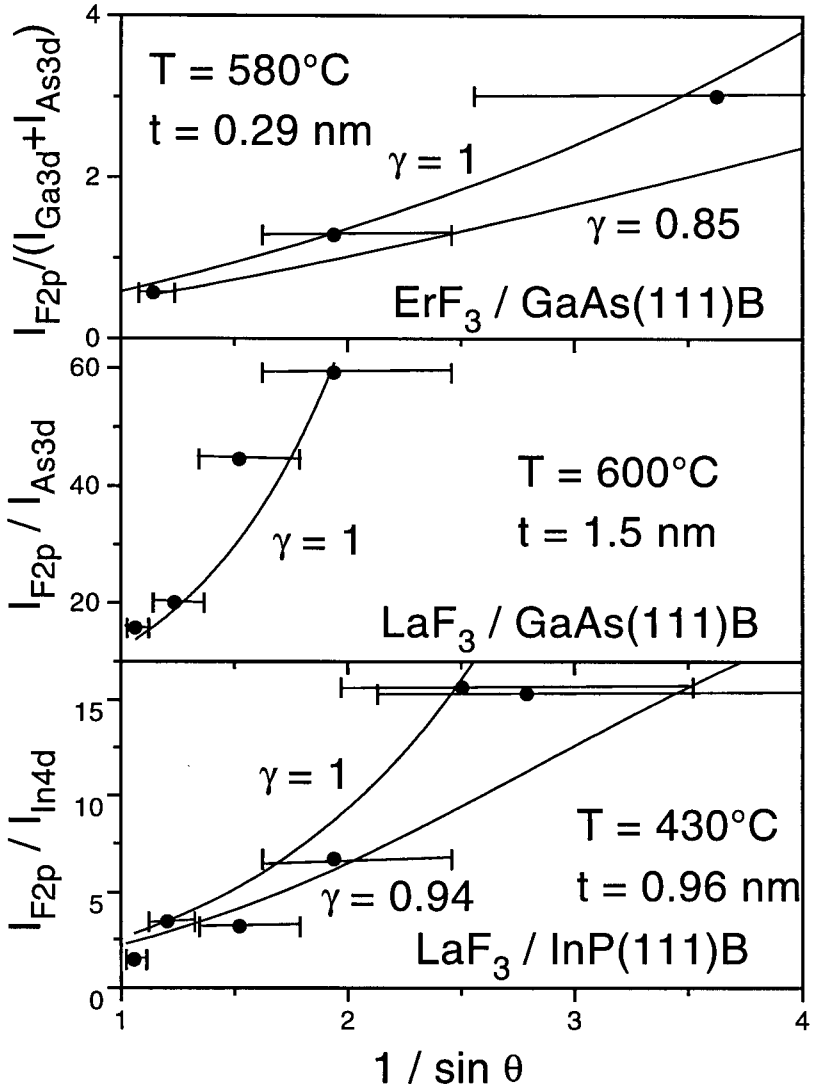


Figure 3.18: Film/substrate intensity ratio vs. $1/\sin\theta$ for the $ErF_3$/GaAs(111)B, $LaF_3$/GaAs(111)B and $LaF_3$/InP(111)B samples obtained using angle dependent photoemission spectroscopy. The annealing temperatures and the film thickness for each sample are indicated. The solid lines are the intensity ratio calculated using the expression for the film/substrate intensity ratio in Eqn. 3.7 using the values of the fractional coverage $\gamma$ indicated. The error bars correspond to the angle subtended by the photoelectron energy analyser.

Table 3.4: Film thickness $t$ and the range of the fractional coverage $\gamma$ obtained by angle dependent photoemission spectroscopy for the $ErF_3$ and $LaF_3$ films grown on GaAs(111)B and InP(111)B substrates at each annealing stage.

| | annealing temperature T (°C) | thickness t (nm) | coverage $\gamma$ |
|---|---|---|---|
| | 470 | $1.4 \pm 0.2$ | 0.9–1.0 |
| $ErF_3$/GaAs(111)B | 540 | $0.3 \pm 0.1$ | 0.9–1.0 |
| | 580 | $0.3 \pm 0.1$ | 0.9–1.0 |
| $LaF_3$/GaAs(111)B | 600 | $1.5 \pm 0.2$ | 0.98– 1.0 |
| | 370 | $1.0 \pm 0.1$ | 0.98–1.0 |
| $LaF_3$/InP(111)B | 495 | $0.3 \pm 0.1$ | 0.98 – 1.0 |
| | 530 | $0.3 \pm 0.1$ | 0.5 – 0.6 |

results in a decrease in coverage. This suggests that the fluoride films re-evaporate rather uniformly without exposing the substrates up to the monolayer coverage without forming 3D islands. This is expected since the surface energy of the fluorides are lower than that of the semiconductor substrates.

## 3.3 Formations of Chemical Bonds at the Film/Substrate Interface

The formation of chemical bonds at the rare-earth trifluoride/III-V semiconductor interface are studied by photoemission spectroscopy. Overview spectra of the $LaF_3$/GaAs(111)B and $LaF_3$/InP(111)B thin film samples in Fig. 3.16 and 3.17 showed some small components developing at the lower binding energy of the fluorine (F) 2p peaks which are usually the sign of chemical reactions at the interface between the film and the substrate. To further investigate the change in electronic structures of the samples, the core level spectra of a $LaF_3$/GaAs(111)B sample are closely examined.

Photoemission spectra showing the the substrate (Ga 3d, As 3d) and film (La 4d)

core levels for a $LaF_3$/GaAs(111)B sample with $LaF_3$ film thickness of 2 nm are shown in Fig. 3.19 to 3.21. The relative thickness of the $LaF_3$ film is measured by quartz thickness monitor (see Fig. 2.5). The relative thickness was corrected by using the film thickness of $LaF_3$ films which were determined by angle dependent photoemission spectroscopy. The spectra are taken after the sample was annealed for 1 min. at the temperatures indicated in the figures. The temperatures of the samples were measured by an infrared pyrometer through a view port with an estimated accuracy of $\pm 20°C$.

No chemically shifted components are detected in the spectra of As 3d and Ga 3d core levels. We interpret the overall shift of the Ga 3d peak towards a lower binding energy as the result of a Fermi level shift. Photoemission intensity of the Ga 3d core level as well as the La 5p core levels in Fig. 3.19 decreased with annealing. On the other hand, the intensity of the As 3d core level increased with annealing. The decrease of the La 5p level intensity and an increase in As 3d core level intensity is an indication that the fluoride thin film is evaporating as has been shown in Section 3.2 by angle dependent photoemission spectroscopy. The ratio of the Ga 3d to As 3d intensities as a function of annealing temperature is plotted in Fig. 3.22. The ratio of Ga 3d to As 3d photoemission intensities decreases with increasing annealing temperature. We have also observed a decrease in the intensity of F 2p peaks with increasing temperature. We interprete this loss of fluorine and the decrease in the Ga/As ratio as being due to the formation of volatile $GaF_x$ molecules with annealing.

Some chemically shifted components develop in the La 4d core levels in Fig. 3.21 as the sample is heated to higher temperatures. To resolve the components present in the La 4d core levels, a mixed Gaussian-Lorentzian function in Eqn. 2.1 is fitted to the spectrum taken after the 600°C anneal and is shown in Fig. 3.23. The solid line in the figure is the fit of the function and the dashed lines are the two chemically shifted components separated by 1.5 eV. The component at the lower binding energy is labelled, *La 1* and

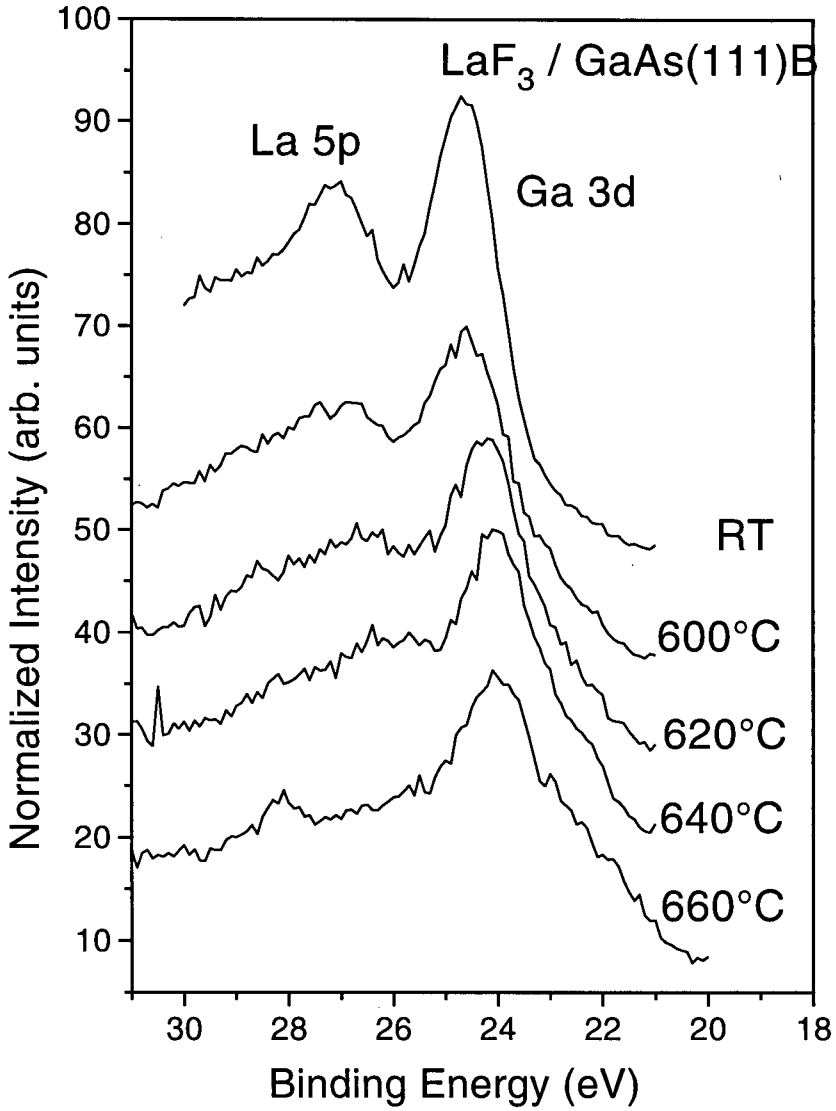


Figure 3.19: Photoemission spectra for the Ga 3d and La 5p core levels from a $LaF_3$/GaAs(111)B sample of film thickness 2 nm after being annealed for 1 min at the temperatures indicated.

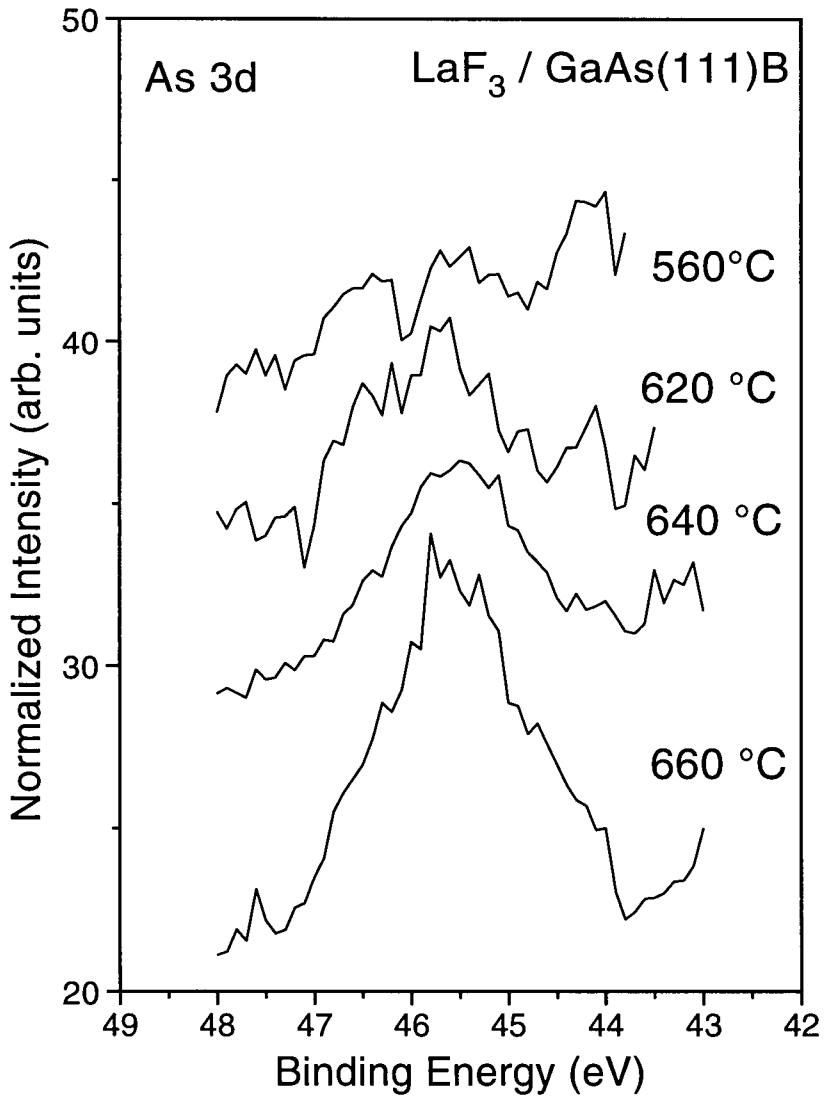


Figure 3.20: Photoemission spectra for the As 3d core levels from a $LaF_3$/GaAs(111)B sample with film thickness 2 nm after being annealed to the temperatures indicated.

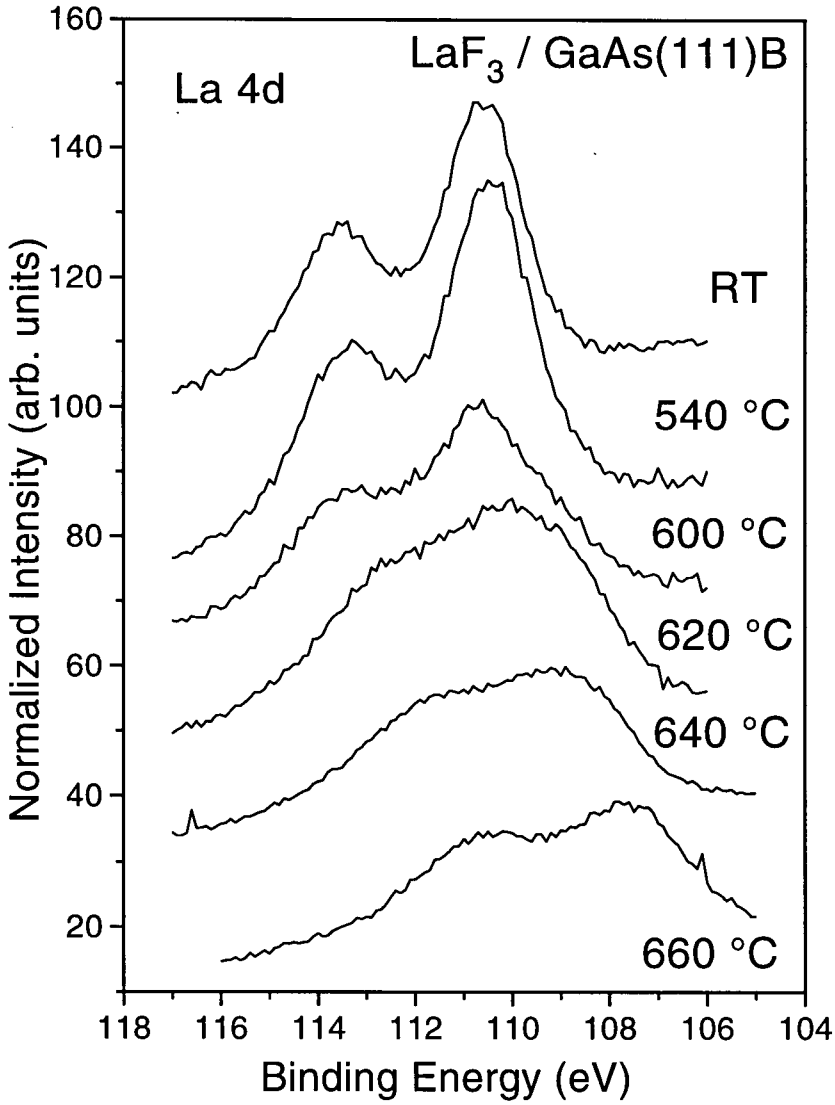


Figure 3.21: Photoemission spectra of La 4d core levels from a $LaF_3$/GaAs(111)B sample with film thickness 2 nm. The annealing temperatures are indicated. The two peaks correspond to La $4d_{3/2}$ and La $4d_{5/2}$ core levels which are split by spin-orbit splitting.

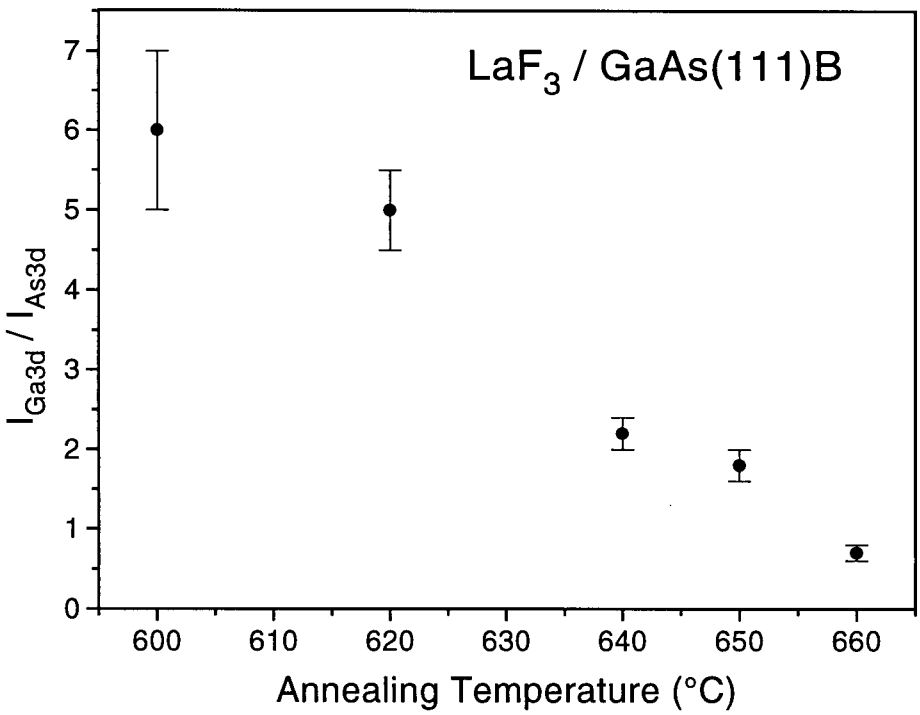


Figure 3.22: The Ga 3d to As 3d photoemission intensity ratio as a function of annealing temperature for a $LaF_3$/GaAs(111)B sample with film thickness 2 nm. A decreace in the intensity ratio with annealing was observed. The decrease in the Ga/As intensity ratio as well as a loss of fluorine atoms with annealing suggest a formation of volatile $GaF_x$ molecules with annealing.

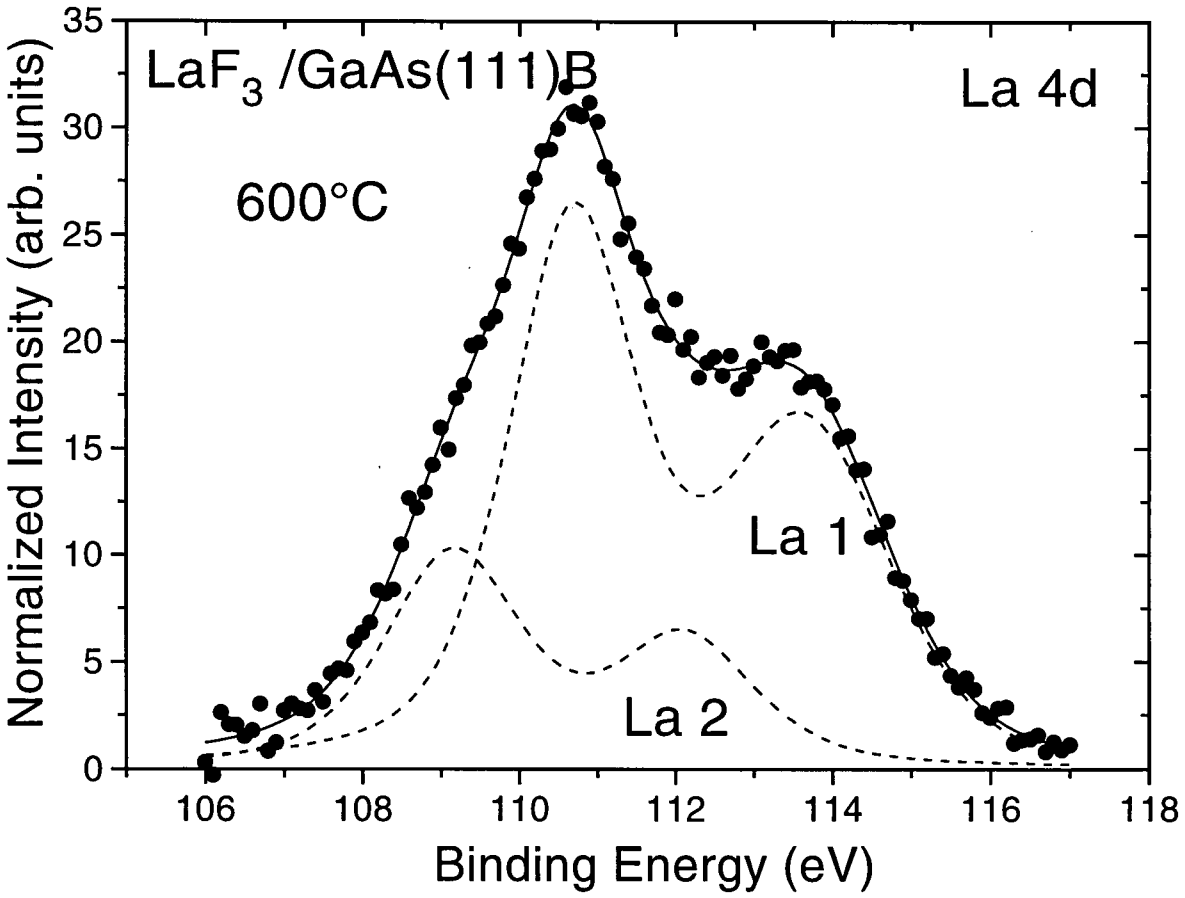


Figure 3.23: Fit of the Gaussian–Lorentzian function to the La 4d core levels from the $LaF_3$/GaAs(111) sample after being heated to 600°C. The chemically shifted components, labelled La 1 and La 2 1.5 eV apart are present. The La 1 component is interpreted as being originated from the bulk La–F bonding and the La 2 component as from the interfacial La–As bonding.

the shifted component, *La 2*. Another component present in the La 4d spectrum taken after the 660°C anneal is labelled *La 3*.

We interpret that the component at the lowest binding energy, *La 1* originates from the La–F bond in the bulk $LaF_3$ film. The second component, *La 2* is likely the interfacial component as a result of the formation of chemical bonds at the interface. The La atoms are probably bonded to the As atoms at the interface, since GaAs(111)B substrate is As terminated. In the overview spectra of this sample after the 640°C anneal, no fluorine peaks are detected indicating that the $LaF_3$ molecules are dissociated. The last component *La 3* is attributed to the chemisorbed La atoms of the dissociated $LaF_3$ molecules on the substrate surface.

Two configurations can be considered at the interface. The first configuration is when the fluorine atoms are situated right above the As atoms, the sites occupied by Ga atoms in the bulk GaAs. The fluorine atoms are bonded to the As atoms. The La atoms are situated above the Ga atoms. The schematic illustration of the configuration at the interface is shown in Fig. 3.24. In this configuration, the chemical shift in the La 4d core level can occur indirectly through the electron transfer from arsenic (As) to fluorine (F) atoms. In the second model, the La atoms are situated directly above the As atoms. The sites above the Ga atoms are then occupied by the fluorine atoms as illustrated in Fig. 3.25. In this model the chemical shifts in the La 4d core level occur as a results of formation of chemical bonds between arsenic (As) and lanthanum (La) atoms.

We expect that the second model in Fig. 3.25 is more plausible of the two models because of the following reasons. Since the La atoms are more positively charged ones of the ionic $LaF_3$ molecules, they are most likely bonded to the As atoms which are more electronegative than the Ga atoms. We have observed a loss of fluorine atoms and a decrease in the intensity ratio of Ga 3d to As 3d levels with annealing suggesting a formation of volatile $GaF_x$ molecules. This is also consistent with the second model

where a loss of fluorine atoms are involved upon the formation of As–La bonds. The chemical shift of the La 4d levels is also in agreement with the second model, since the electron transfer in the second model directly involves the La ions.

## 3.4 Positions of Er 4f levels in $ErF_3$/GaAs(111)B

The positions of Er 4f levels in the Er ions in $ErF_3$/GaAs(111)B samples are studied using resonant photoemission spectroscopy. The resonance is an enhancement of emission due to the interference between two or more emission processes having the same final states as described in Section 3.1. For $ErF_3$, the resonance is observed near the Er 4d absorption edge due to the $Er^{3+}$ $4f^{11} \rightarrow 4f^{10}$ transitions. The photon excitation energies where the resonance occurs are determined from a total electron yield spectrum of the Er 4d absorption edge. Typical total yield spectrum from the Er 4d absorption edge of an $ErF_3$/GaAs(111)B sample is shown in Fig. 3.26. The peaks in the spectrum are due to the resonance involving the $4d$–$4f$ transition in the $Er^{3+}$ ions. To locate the binding energy positions of $Er^{3+}$ $4f^{11}$ levels, the photoemission spectrum is taken with one of the resonant photon excitation energies. Next the photoemission spectrum with the non-resonant photoexcitation energy which is located just below the 4d absorption edge, is obtained. The intensities of the photoemission spectra are normalized by the incident flux of the Synchrotron beam. Since the enhancement of the photoemission intensity is due to the $Er^{3+}$ $4f^{11} \rightarrow 4f^{10}$ transition, the difference in intensity between the resonance and the non-resonant spectra must be from the $Er^{3+}$ $4f^{11} \rightarrow 4f^{10}$ transition. Typical resonant, non-resonant and difference spectra of an $ErF_3$/GaAs(111)B sample are shown in Fig. 3.27. The different spectra of the $ErF_3$/GaAs(111)B samples of two film thicknesses are shown in Fig. 3.28. The resonant and non-resonant spectra were taken at 174 and 161 eV repectively for both samples. The thicknesses indicated in the

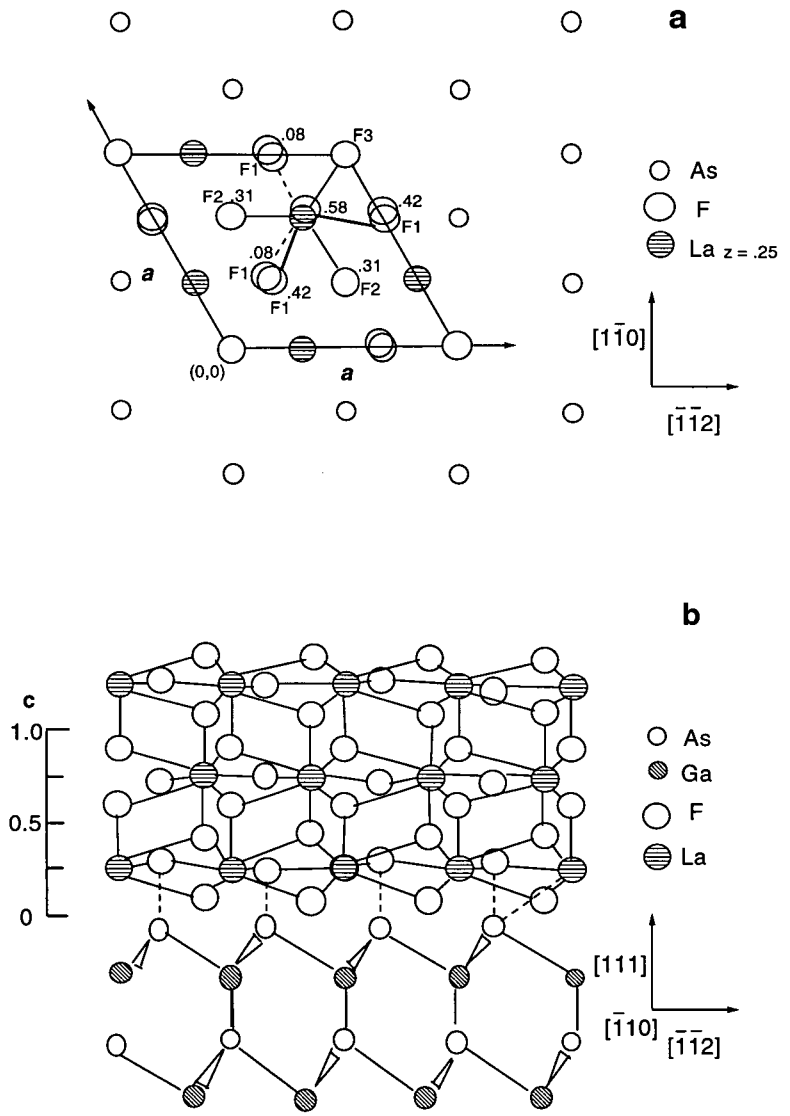


Figure 3.24: Schematic illustration showing a configuration at the interface of the $LaF_3$/GaAs(111) samples: Model 1. In this model, the fluorine atoms overlap with the As atoms. La atoms are situated above the Ga atoms. The figure shows the view along the $c$-axis of $LaF_3$ or the [111] direction of the GaAs substrate (a) and the view along the [$\bar{1}$10] direction of the GaAs substrate (b). Only the first layer of the one of the $LaF_3$ unit cell is shown in (a). The numbers indicated are the positions of the fluorine atoms along the $c$-axis in (a).

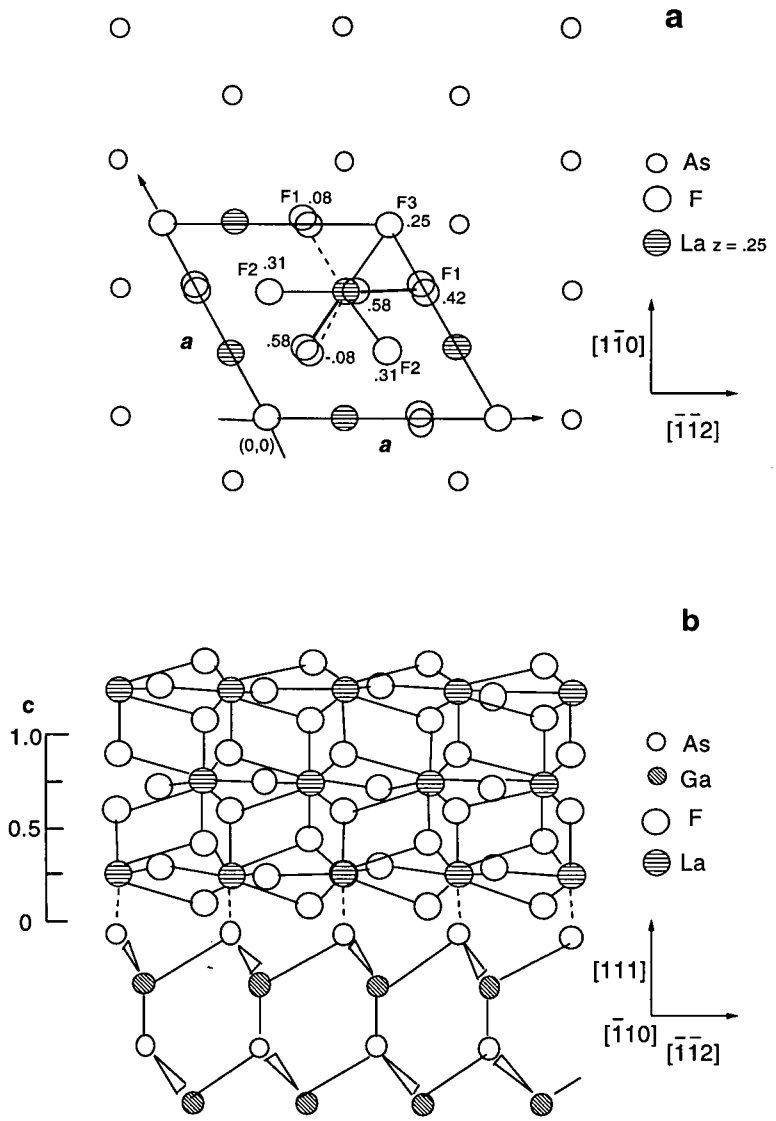


Figure 3.25: Schematic illustration showing a configuration at the interface of the $LaF_3$/GaAs(111) samples: Model 2. In this model, the La atoms are situated directly above the As atoms. The sites above the Ga atoms are occupied by the fluorine atoms. The figure shows the view along the $c$-axis of $LaF_3$ or the [111] direction of the GaAs substrate (a) and the view along the [$\bar{1}$10] direction of the GaAs substrate (b). Only the first layer of the one of the $LaF_3$ unit cell is shown in (a). The numbers indicated are the positions of the fluorine atoms along the $c$-axis in (a).

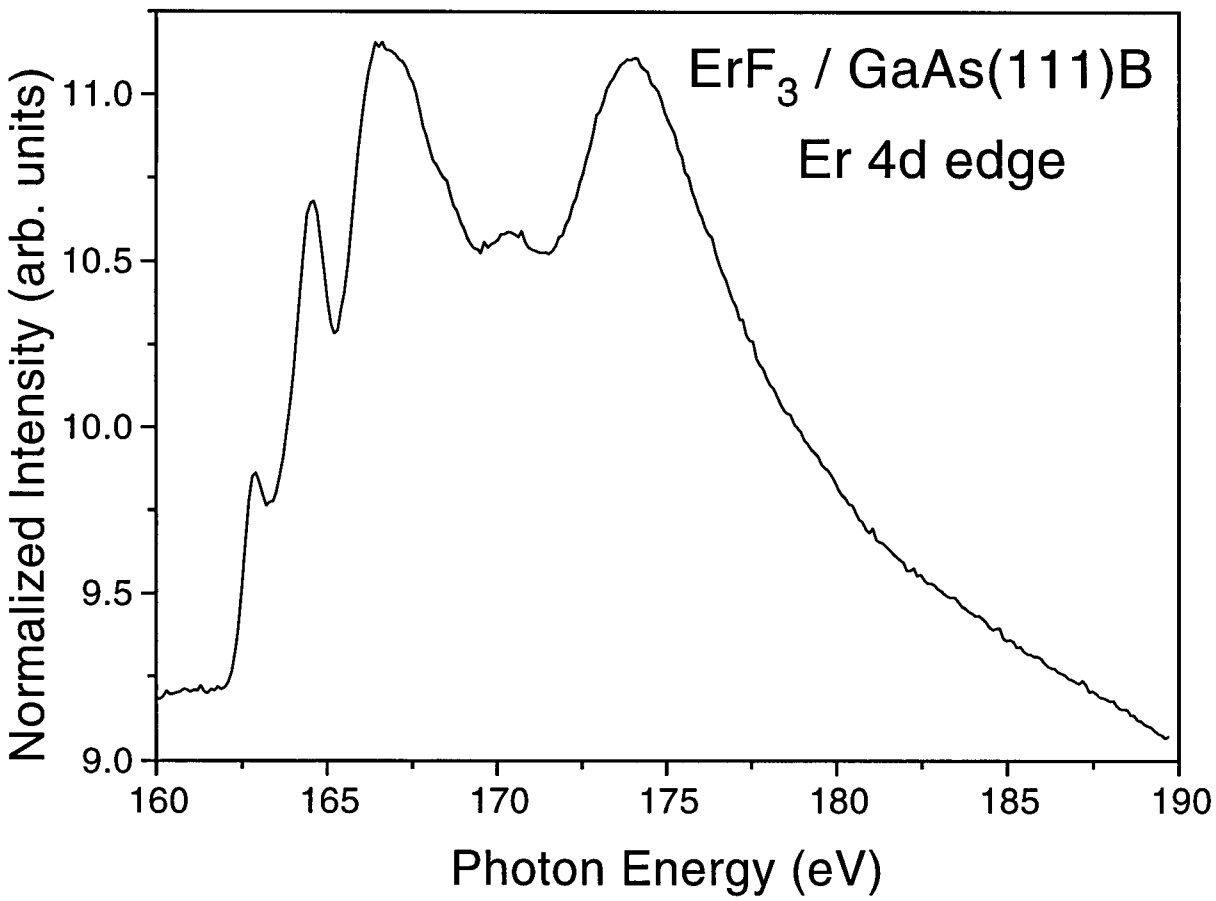


Figure 3.26: Total electron yield spectra of Er 4d absorption edge (N edge) from a $ErF_3$/GaAs(111)B sample. The peaks at $h\nu$ = 163.0, 164.7, 166.9, 170.8 and 174.0 eV are due to the 4d-4f resonance of the $Er^{3+}$ ions.

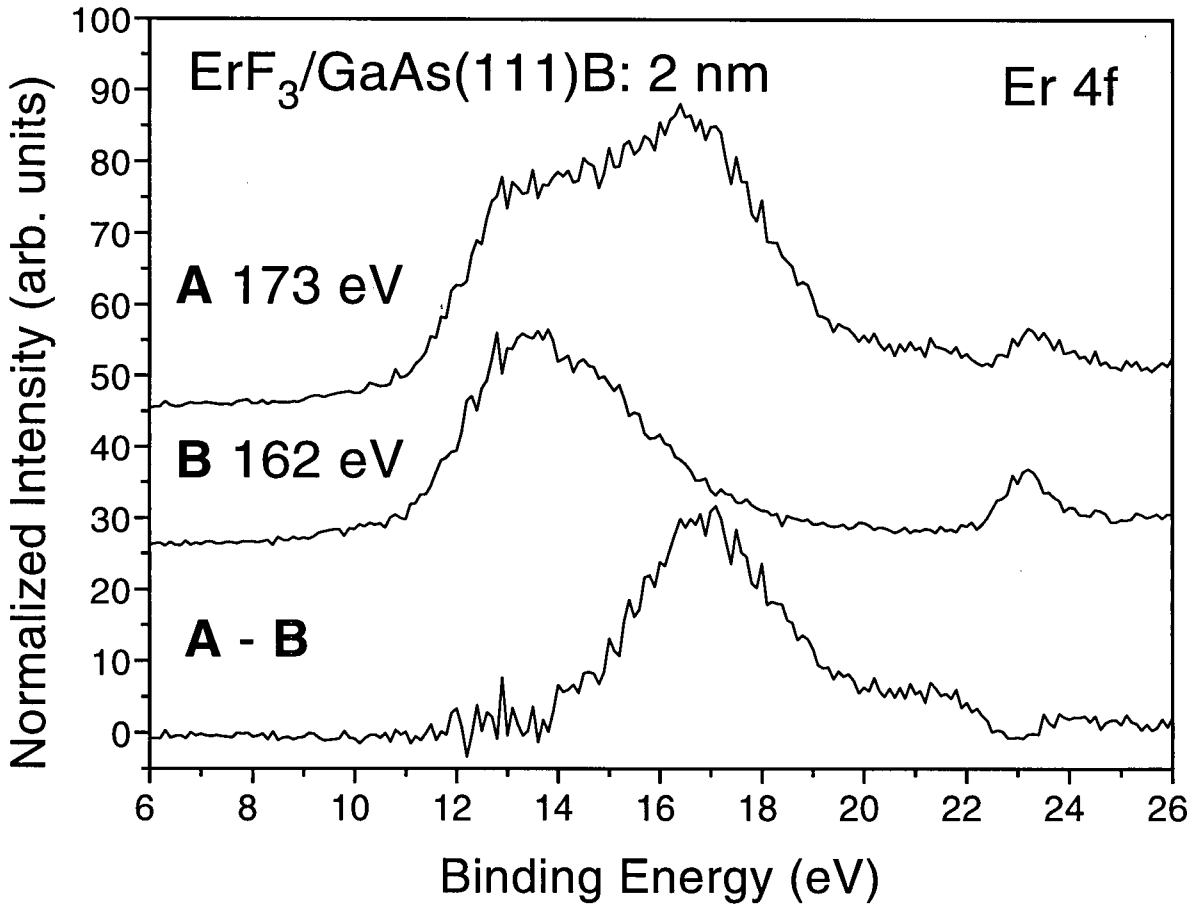


Figure 3.27: Resonant (A), non-resonant (B) and the difference spectra of the Er 4f levels in the Er ions for the $ErF_3$/GaAs(111)B sample with film thickness 2 nm. The excitation energies $h\nu$ are indicated in the figure.

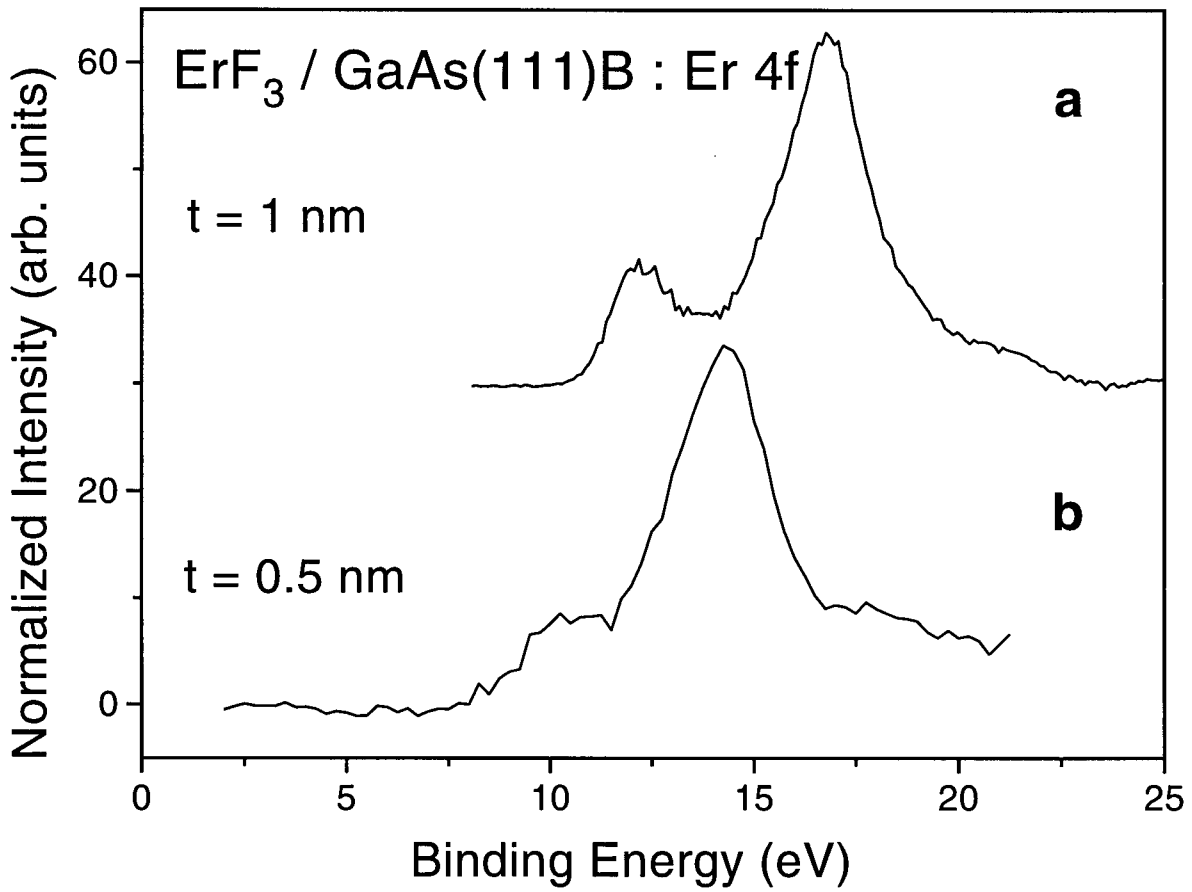


Figure 3.28: Difference spectra of the Er 4f levels in the $Er^{3+}$ ions for the $ErF_3$/GaAs(111)B samples as in Fig. 3.27 for film thicknesses (a) 1 nm and (b) 0.5 nm. The resonant and non-resonant spectra were taken at 174 and 161 eV repectively for both samples.

figure are determined using angle dependent photoemission spectroscopy.

In the 1 nm sample shown in Fig. 3.28 (a), two peaks separated by 4.8 eV are observed. The peaks are the results of the exchange splitting of $Er^{3+}$ 4f levels. The $Er^{3+}$ $4f^{11}$ level has a ground state configuration of $(4f\uparrow)^7(4f\downarrow)^4$ with total spin $S = 3/2$. The final state configuration after the removal of an electron can be either $(4f\uparrow)^6(4f\downarrow)^4$, $S = 1$ or $(4f\uparrow)^7(4f\downarrow)^3$, $S = 2$. Since the $4f\uparrow$ electron has a larger binding energy than the $4f\downarrow$ electron, the peak at the higher binding energy in the difference spectrum of the 1 nm sample in Fig. 3.28 corresponds to the transition $(4f\uparrow)^7(4f\downarrow)^4 \rightarrow (4f\uparrow)^6(4f\downarrow)^4$, whereas the smaller peak at the lower binding energy corresponds to the transition, $(4f\uparrow)^7(4f\downarrow)^4 \rightarrow (4f\uparrow)^7(4f\downarrow)^3$. The ratio of the photoemission intensity of the transition $(4f\uparrow)^7(4f\downarrow)^4 \rightarrow (4f\uparrow)^6(4f\downarrow)^4$ to the transition $(4f\uparrow)^7(4f\downarrow)^4 \rightarrow (4f\uparrow)^7(4f\downarrow)^3$ transition is expected to be approximately 7:4 since there are seven electrons to choose from in the former transition whereas there are only three electrons to choose from for the latter transition. The ratio between the two photoemission peaks were approximately 7 : 1 instead of 7 : 4. The discrepancy may be due to the change in experimental conditions between the acquisition of resonant and the non-resonant spectra, such as the chamber pressure and the angle or position of incident beam relative to the sample. There could also be more steps involved in the resonant photoemission mechanism than the simple transition process described above. In the 0.5 nm sample, the $Er^{3+}4f^{11}$ resonant peak has been shifted to a lower binding energy as compared to the peak observed in the 1 nm sample. In the overview spectra of the same sample, the fluorine peaks were absent. Hence we interpret that the resonant photoemission intensity is originated from the Er ions of the dissociated $ErF_3$ molecules chemisorbed on the GaAs surface.

## 3.5 Band Alignments

The relative positions of the electronic energy bands at the interface between the semiconductor and the fluoride film were obtained by linear extrapolations of the sharp edges in the valence band photoemission spectra. Determining the band alignments is important in designing device structures. The band alignments were determined with films which were sufficiently thin that the substrate spectrum can be measured at the same time as the valence band of the films. An example of the linear extrapolation is shown in Fig. 3.29 for a $LaF_3$/GaAs(111)B sample. An average of positions of the measurements for three samples for each system is taken. There were 6 to 8 photoemission spectra for each sample. The estimated accuracy of the relative positions is $\pm 0.3$ eV. The standard deviations of the measurements of three samples were less than or equal to 0.3 eV.

The measured positions of the F 2p derived valence band in the fluoride films relative to the semiconductor valence band maxima are shown schematically in Fig. 3.30. Positions of $Er^{3+}$ 4f levels determined by the resonant photoemission spectroscopy are also shown. Two peaks correspond to the exchange splitting of the $Er^{3+}$ 4f levels. The energy gaps between the conduction band and the valence band are 1.42 eV for GaAs, 1.35 for InP and 9.9 eV for $LaF_3$ [26].

## 3.6 Summary

The initial stage of rare-earth trifluoride film growths on III-V semiconductors was investigated by photoemission spectroscopy. The angle dependent photoemission spectroscopy results were consistent with the complete coverage of semiconductor substrates by $LaF_3$ and $ErF_3$ films. We have also shown by angle dependent photoemission spectrosocpy that the $LaF_3$ and $ErF_3$ re-evaporate rather uniformly upon annealing without exposing the substrates. A decrease of Ga and fluorine atoms upon annealing suggests a formation

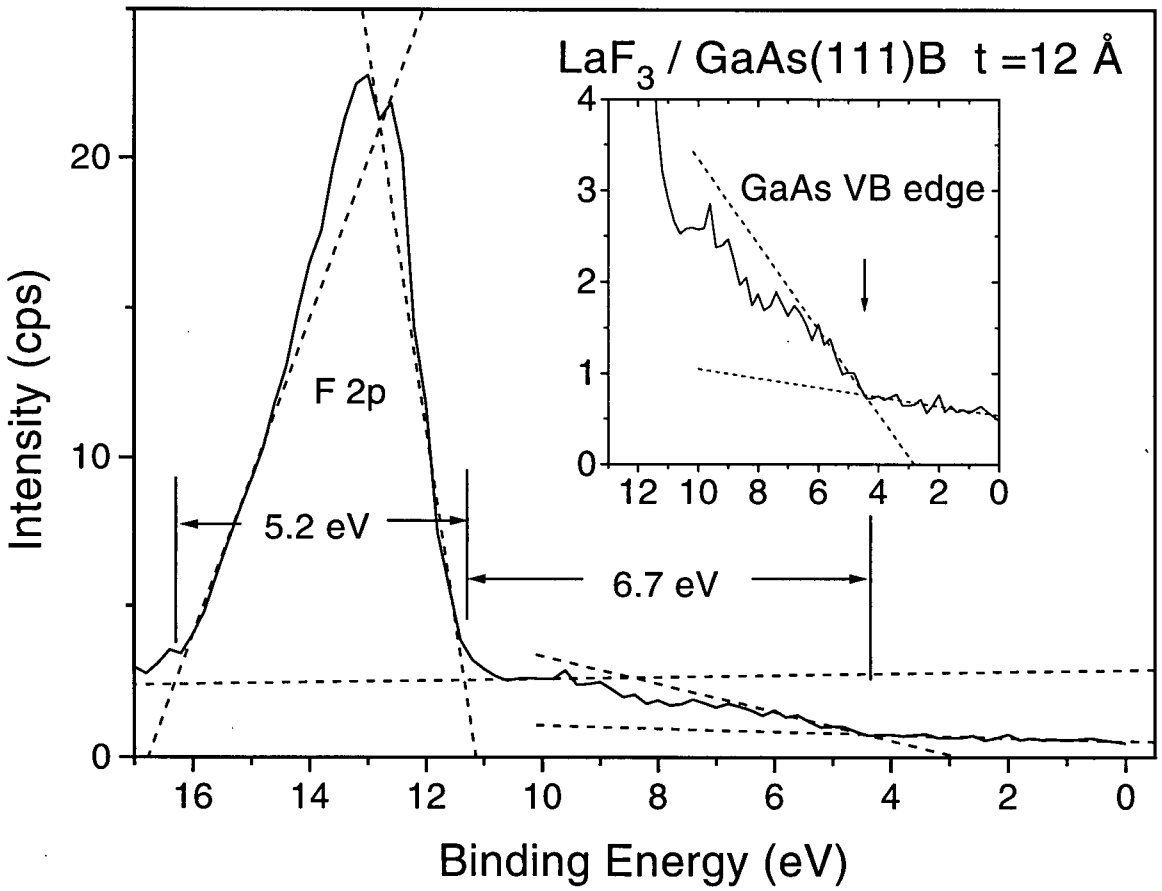


Figure 3.29: Photoemission spectrum of a $LaF_3$/GaAs(111)B sample of thickness 1.2 nm showing the GaAs valence band and the fluorine 2p valence band. The dashed lines are the linear extrapolation to determine the relative position of the valence band edges. The GaAs valence band edge is shown enlarged in the inset.

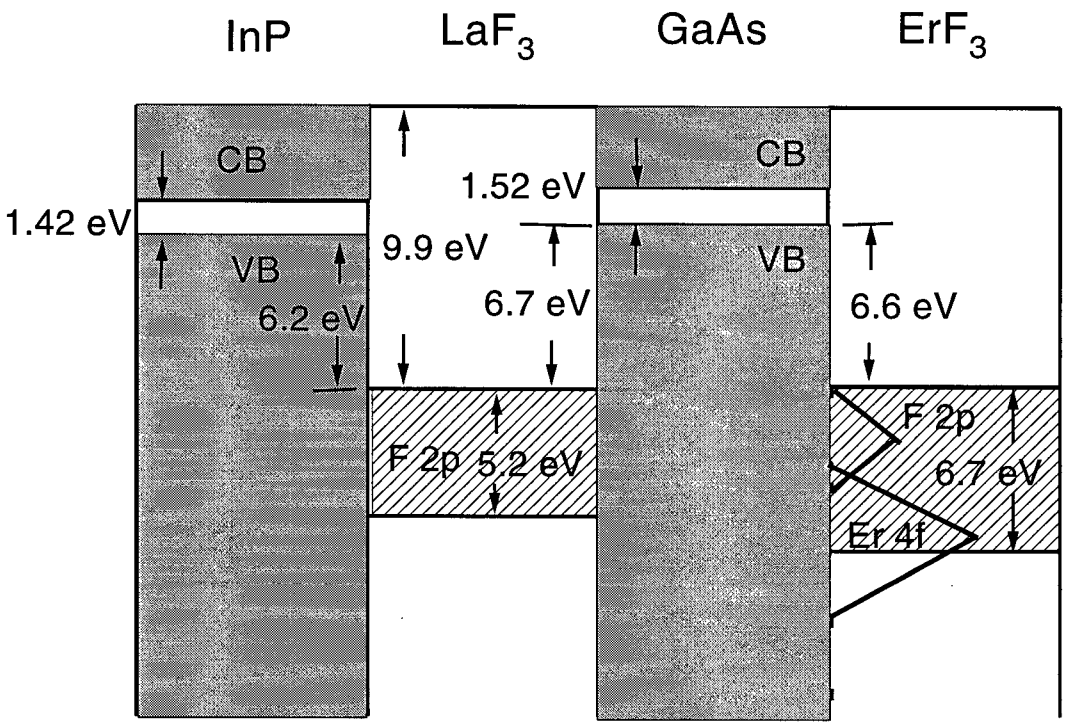


Figure 3.30: Interfacial band alignments in the $LaF_3$/InP(111), $LaF_3$/GaAs(111) and $ErF_3$/GaAs(111) systems determined by linear extrapolations of the sharp edges in the valence band photoemission spectra with an estimated accuracy of $\pm 0.3$ eV. Positions of $Er^{3+}$ 4f levels are also shown. Two peaks correspond to the exchange splitting of the $Er^{3+}$ 4f levels.

of volatile $GaF_x$ molecules. The presence of La and Er atoms on the substrate surface upon annealing above 600°C, indicate that some fluoride molecules dissociate and form volatile $GaF_x$ molecules leaving the La and Er atoms behind on the substrate surface.

From the core level photoemission spectroscopy, we have observed the formation of chemical bonds between the La and the substrate atoms. The loss of Ga and F atoms with annealing as well as the La 4d core level shifts are consistent with the interface bonding model in which the La atoms are chemically bonded to the As atoms at the interface.

The band alignments or the relative positions of the film and the substrate valence band edges are determined by photoemission spectroscopy of the valence band regions. The positions of Er 4f levels in $ErF_3$ on GaAs were also determined by resonant photoemission spectroscopy. The relative positions of valence band edges at the insulator/semiconductor interface are useful in designing electronic or optoelectronic devices.

# Chapter 4

## Structural Properties

The bulk structures of fluoride films grown on semiconductors is one of the important factors which affect the subsequent growth of other materials on the fluoride films. The growths of semiconductors or other materials on fluorides are important in applications such as integrated devices and high reflectance mirrors. Our objective in this chapter is to characterize the structural properties of the fluoride films such as crystal orientations, strains and crystallinity. We have characterized the structural properties of rare-earth trifluoride films of thickness between 10 and 400 nm grown on GaAs and InP using X-ray diffraction.

The crystal orientation of the fluoride films are first determined by X-ray diffraction using a powder X-ray diffractometer. The strains in the rare-earth fluoride films grown on GaAs and InP are measured by high resolution X-ray diffraction (HRXRD). The crystallinity of $LaF_3$ films are studied using the rocking curve measurements. From the rocking curve measurements, we determine the lateral coherence lengths in the $LaF_3$ films grown on GaAs and InP. The X-ray diffraction measurements of the $LaF_3$/semiconductor samples were performed using a Cu K$\alpha$ source with powder and four-crystal diffractometers (BEDE 200). The $LaF_3$ and $ErF_3$ films are grown on GaAs and InP substrates using a high temperature effusion cell as described in Chapter 2.

The $LaF_3$ crystal has a trigonal structure with space group $P\bar{3}c1$ ($D^4_{3d}$) and has lattice constants of $a = 7.185$ Å and $c = 7.351$Å [12]. The trigonal $a \times a$ face of the $LaF_3$ crystal has the same symmetry as the hexagonal (111) face of GaAs or InP as shown in

Fig. 4.31 (a). In this configuration, the trigonal $a \times a$ unit cell of $LaF_3$ corresponds to $\sqrt{3} \times \sqrt{3}$ of the underlining hexagonal lattice of semiconductors or $\sqrt{6}a/2 \times \sqrt{6}a/2$ of semiconductors where $a$ is the lattice constant of the substrate. The lattice mismatch at room temperature in this configuration is +3.8 % for $LaF_3$/GaAs(111) and −0.04 % for $LaF_3$/InP(111). It has been shown by Sinharoy *et al.* [5] using LEED and RHEED that the trigonal $a \times a$ face of the $LaF_3$ crystal is aligned parallel to the hexagonal (111) face of GaAs or the $c$-axis of $LaF_3$ is oriented parallel to the [111] axis of GaAs as in Fig. 4.31 (a). Due to the structural similarity, we expect the $LaF_3$ films on InP(111) to be oriented in the same manner.

The crystal structure of $ErF_3$ is orthorhombic at room temperature. A LEED study of $GdF_3$ deposited on Ge(111) and GaAs(111)B substrates by Jenkins *et al.* [10] showed that the $a \times c$ plane of orthorhombic $GdF_3$ crystals are aligned parallel to the (111) plane of the substrates or the $b$-axis of the film is oriented parallel to the [111] axis of the substrate. The LEED pattern of a $GdF_3$ film 1.8 nm thick deposited on a GaAs(111)B substrate showed a symmetry which coincides with an orthorhombic mesh rotated by 120 and 240° along the [010] axis [10]. Therefore we expect the $b$-axis of orthorhombic $ErF_3$ crystals to be oriented parallel to the [111] axis of the GaAs or InP substrates as well, as shown in Fig. 4.31 (b). In this configuration, the lattice mismatch of $ErF_3$ with GaAs at room temperature is −8.6 % along the $a$-axis and +9.0 % along the $c$-axis. The lattice mismatch of $ErF_3$ with InP is −12 % along the $a$-axis and +5.4 % along the $c$-axis. There is a large difference in thermal expansion coefficient between GaAs or InP and $LaF_3$. At 300 K, the thermal expansion coefficients are $16 \times 10^{-6}$ $K^{-1}$ along the $a$ axis for $LaF_3$, $5.7 \times 10^{-6}$ $K^{-1}$ for GaAs and $4.75 \times 10^{-6}$ $K^{-1}$ for InP.

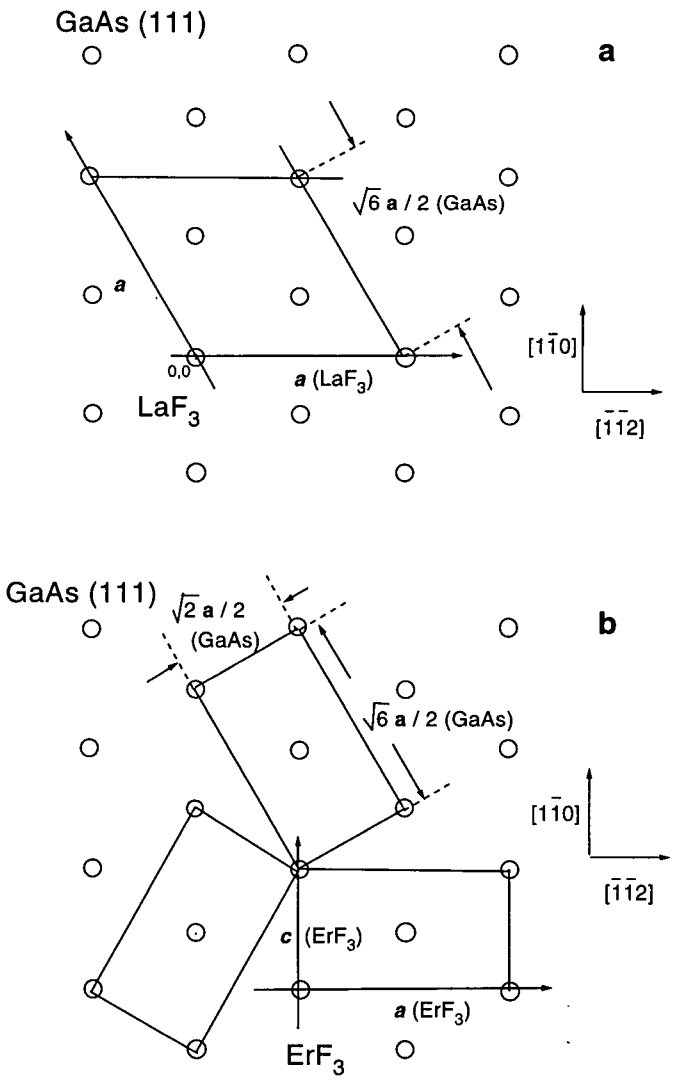


Figure 4.31: Plan view of the (111) plane of GaAs (or InP) substrate showing the structural matching with (a) $LaF_3$ and (b) $ErF_3$ assuming perfect lattice matching. The circles indicate the substrate atoms. The lines in (a) show the trigonal $a \times a$ plane of $LaF_3$ which matches $\sqrt{6}a/2 \times \sqrt{6}a/2$ of the substrate where $a$ is the lattice constant of the substrate. The lines in (b) show the orthorhombic $a \times c$ plane of $ErF_3$ which matches $d \times \sqrt{3}d$ of the substrate. Six configurations are possible in (b): $a \times c$ planes rotated by 120° and 240° to each other as shown in the figure and their mirror planes.

## 4.1 Crystal Orientations

A low energy electron diffraction (LEED) pattern of a $LaF_3$ film deposited on a GaAs(111)A substrate is shown in Fig. 4.32. The $LaF_3$ films for the LEED measurements were grown by the same method as the samples grown for photoemission experiments as described in Chapter 2. The thickness of the film was 1.5 nm as measured by a quartz thickness monitor. The LEED pattern in Fig. 4.32 shows two different structures. The first is the $(1 \times 1)$ pattern of the outer most dots which are related to the atomic spacings of the (111) hexagonal plane of the GaAs substrate. The second is the $(\sqrt{3} \times \sqrt{3})$ superstructure of inner dots, which is associated with the lattice constant of the $LaF_3$ trigonal basal plane. The result shows that the (111) plane of the GaAs substrate is oriented parallel to the trigonal $a \times a$ plane of $LaF_3$ film as shown in Fig. 4.31.

The orientations of the thicker films of $LaF_3$ and $ErF_3$ grown on GaAs and InP were also examined using a powder X-ray diffractometer. Fig. 4.33 shows $\theta$–$2\theta$ scans for the $LaF_3$ crystalline powder, $LaF_3$ films on GaAs(111)A and InP(111)B substrates. Strong $(00l)$ type Bragg peaks in the scans of both $LaF_3$ films on GaAs and InP show that the films are single crystals and that the $c$-axis of the $LaF_3$ film is oriented parallel to the [111] axis of the substrates. The trigonal $a \times a$ plane of the $LaF_3$ crystal is thus aligned parallel to the (111) hexagonal face of the substrates as expected from the interfacial structural matching of this configuration. The result is consistent with the LEED and RHEED studies of the $LaF_3$/GaAs(111)A system by Sinharoy *et al.* [5]. In the $\theta$–$2\theta$ scans of $ErF_3$ films grown on GaAs(111)A shown in Fig. 4.34, $(0l0)$ type peaks as well as the $(lll)$ type peaks of the GaAs substrate were observed. This indicates that the $b$-axis of the $ErF_3$ film is oriented parallel to the [111] axis of the GaAs substrate, i.e. the orthorhombic $a \times c$ plane of $ErF_3$ is oriented parallel to the (111) plane of GaAs as shown in Fig. 4.31. This result agrees with the LEED study of $GdF_3$ deposited on Ge(111) and

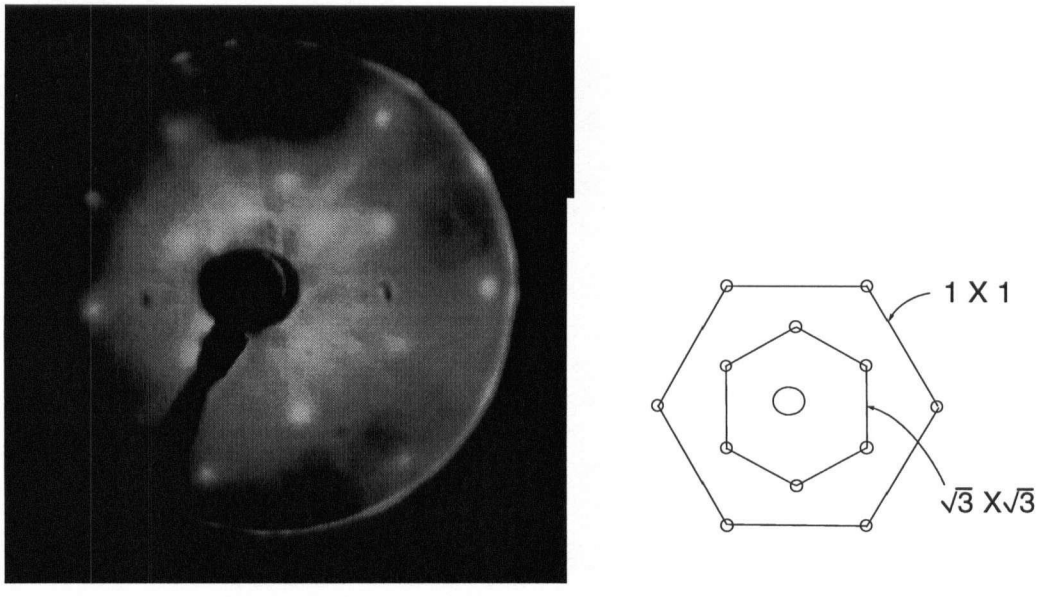


Figure 4.32: LEED pattern of a 1.5 nm thick $LaF_3$ film deposited on a GaAs (111)B substrate with the electron energy of 113.4 eV. It shows two different LEED structures. The first is the $(1 \times 1)$ pattern of the outer most dots which are related to the atomic spacings of the (111)B hexagonal plane of the GaAs substrate. The second is the $(\sqrt{3} \times \sqrt{3})$ superstructure of inner dots, which is associated with the lattice constant of the $LaF_3$ trigonal basal plane.

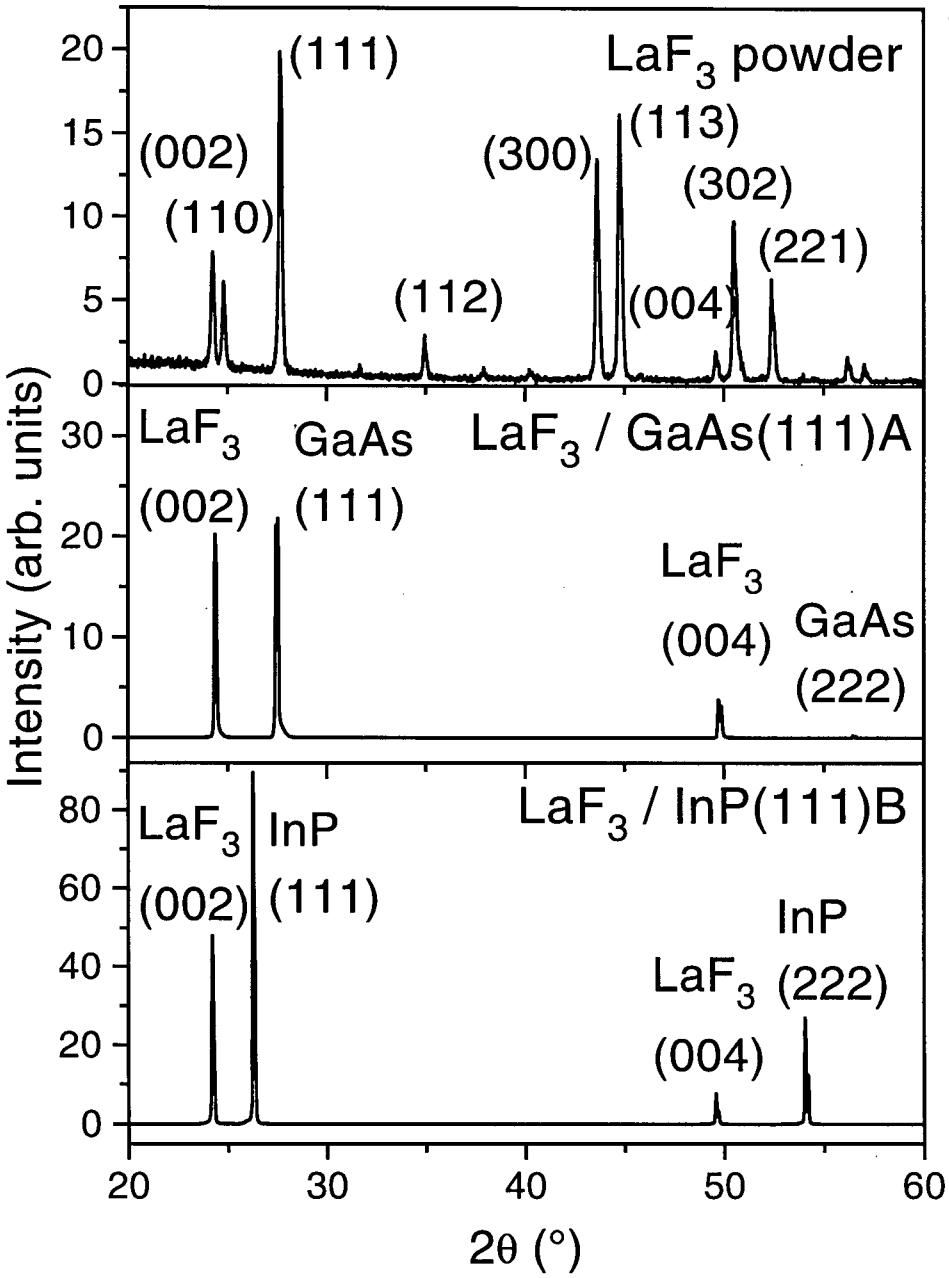


Figure 4.33: Powder X-ray diffraction scans of (top) the $LaF_3$ crystalline powder, (center) $LaF_3$/GaAs(111)A and (bottom) $LaF_3$/InP(111)B samples. The strong (00l) type $LaF_3$ peaks along with (*lll*) type InP peaks indicate that the c-axis of the $LaF_3$ film is aligned parallel to the (*lll*) direction of the substrate.

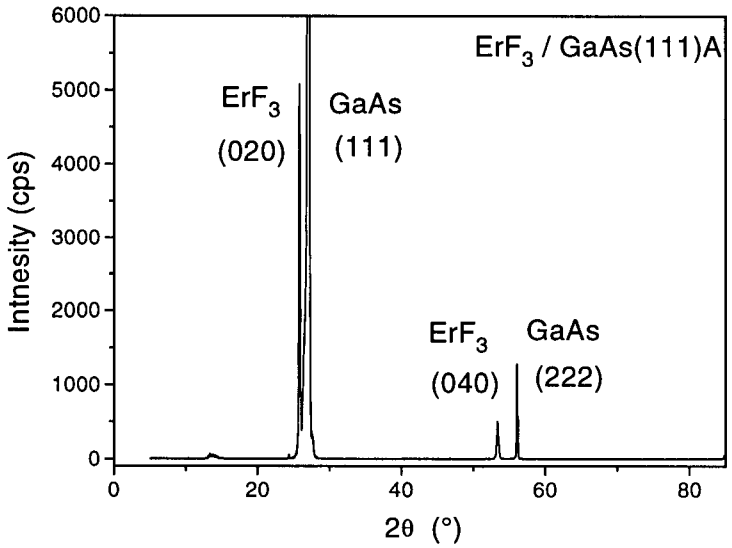


Figure 4.34: Powder X-ray diffraction scans of a $ErF_3$/GaAs(111)A sample with the film thickness t = 41 nm. The $(0l0)$ type $ErF_3$ peaks along with $(lll)$ type GaAs peaks are observed indicating that the $b$-axis of the $ErF_3$ film is aligned parallel to the $(lll)$ direction of the substrate.

GaAs(111)B substrates by Jenkins *et al.* [10].

We have also grown $LaF_3$ films on the (100) face of a GaAs substrate. A $\theta$-$2\theta$ scan of X-ray diffractions using a powder X-ray diffractometer is shown in Fig. 4.35. The top figure shows (002) and (004) peaks of the GaAs substrate. The bottom figure is an enlargement of the top figure. The scan only shows very small $LaF_3$ peaks when aligned to the (001) direction of the substrate. This indicates that the film is polycrystalline. We do not expect $LaF_3$ films to grow as single crystals on (100) surfaces of GaAs substrates, since the cubic (100) face of the semiconductor does not have a same symmetry as the trigonal structure of $LaF_3$.

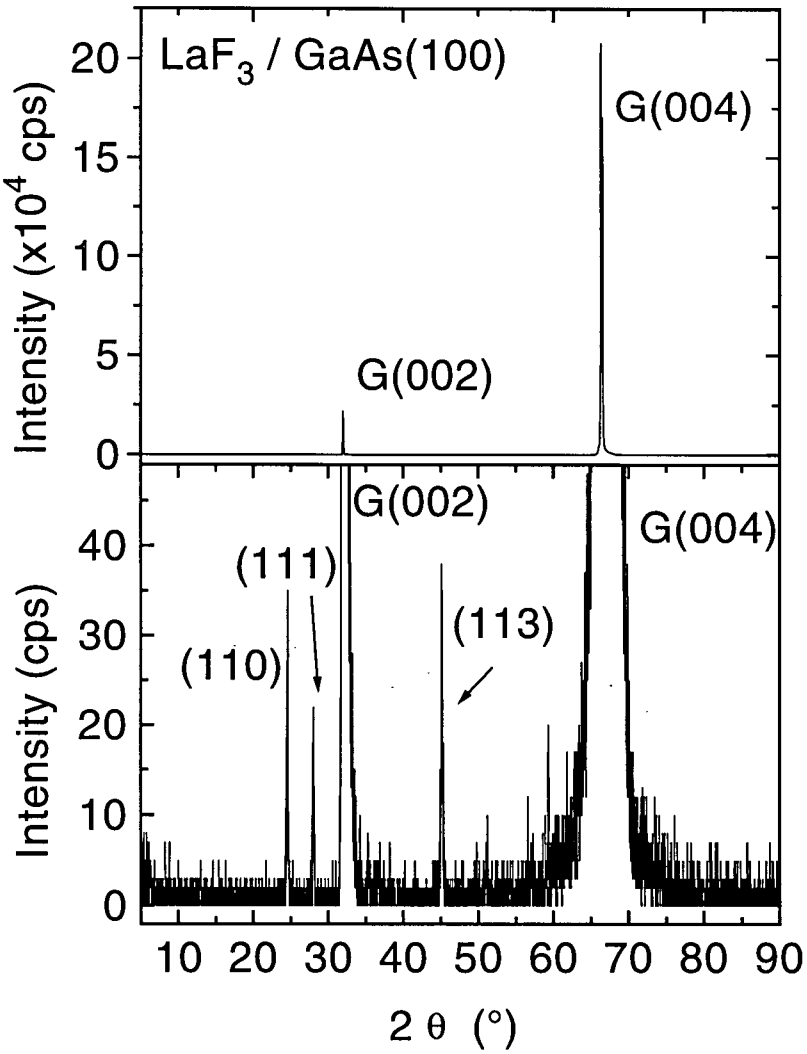


Figure 4.35: Powder X-ray diffraction scans of a $LaF_3$/GaAs(100) sample. The top figure shows (002) and (004) peaks of the GaAs substrate. The marks "G" besides indices indicate that peaks are those of substrates'. The bottom is a blow up of the top figure. The scan only shows small $LaF_3$ peaks suggesting that the film is polycrystalline.

## 4.2 Strains

High resolution X-ray diffraction was performed on the $LaF_3$ and $ErF_3$ films grown on GaAs and InP to study the strains in the fluoride films. Typical $\theta$–$2\theta$ scans for the $LaF_3$ and $ErF_3$ films grown on GaAs and InP are shown in Fig. 4.36. The Bragg peaks of the films and the substrates are observed in the scans as indicated in the figure. To obtain the in-plane strains $\varepsilon_{||}$ or the strains parallel to the film/substrate interface ($a \times a$ plane of $LaF_3$), the strain perpendicular to the interface $\varepsilon_{\perp}$ or the strain along the $c$-axis of $LaF_3$ was first determined from the separation between the (111) GaAs and (002) $LaF_3$ peaks. The values of the lattice constant $c = 7.351$ Å for $LaF_3$ [12] and $a = 5.6534$ Å for GaAs substrate are used in the calculation. The measurements of the lattice constant are performed at two different azimuthal angles for each sample to ensure that the shift of the film peak is not due to the tilting of the $c$-axis of $LaF_3$ with respect to the [111] axis of the substrate. For an isotropic stress in the $a \times a$ plane, the relationship between the in-plane strain $\varepsilon_{||}$ and the perpendicular strain $\varepsilon_{\perp}$ is given by [37]:

$$\varepsilon_{||} = -\frac{C_{33}}{2C_{13}}\varepsilon_{\perp} \tag{4.10}$$

where $C_{33}$ and $C_{13}$ are the elastic constants of the $LaF_3$ film, $C_{13} = 5.9 \cdot 10^{10}$ N m$^{-2}$ and $C_{33} = 22.2 \cdot 10^{10}$ N m$^{-2}$ [38]. Hexagonal symmetry is assumed as was suggested by Laiho *et al* [38].

The in-plane strains in the $LaF_3$ films grown on GaAs(111)A substrates were tensile for the films of thickness less than 200 nm. This is not as expected if the growth is simple pseudomorphic, as the lattice spacing of the trigonal face of $LaF_3$ is larger than that of the hexagonal (111) face of GaAs. The in-plane tensile strain $\varepsilon_{||}$ is plotted as a function of film thickness in Fig. 4.37. The in-plane strain $\varepsilon_{||}$ decreases with increasing film thickness.

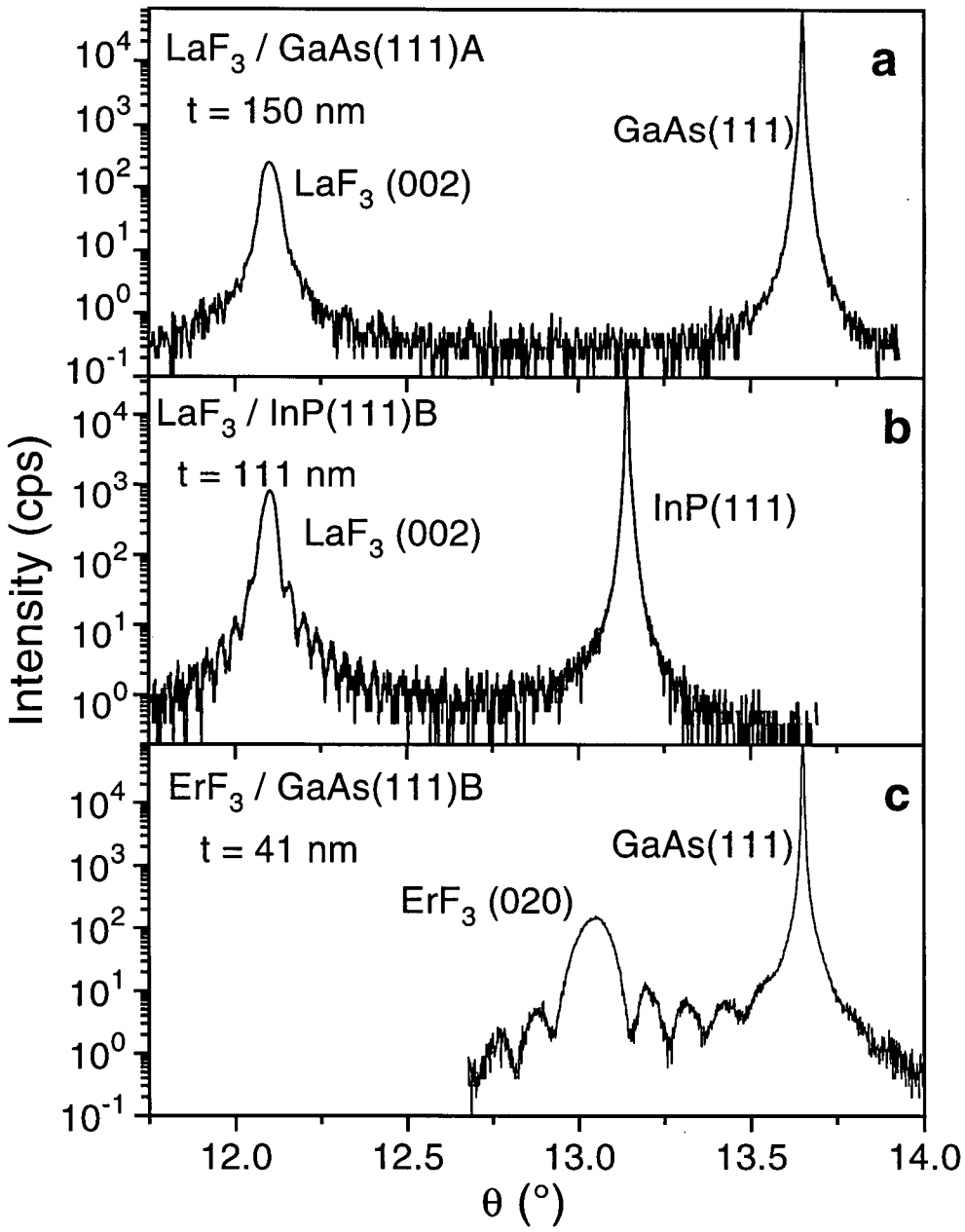


Figure 4.36: High resolution X-ray diffraction scans of the (a) $LaF_3$/GaAs(111)A, (b) $LaF_3$/InP(111)B and $ErF_3$/GaAs(111)A samples.

Tensile strain has also been observed in the Rutherford back scattering (RBS) study of the $CaF_2$/Si(111) system [39]. In the study, the tensile strain was attributed to the large difference in thermal expansion coefficients between $CaF_2$ ($19 \times 10^{-6}$ $K^{-1}$) and Si ($2.5 \times 10^{-6}$ $K^{-1}$). The large difference in thermal expansion coefficients also exists between $LaF_3$ and GaAs. At the growth temperature of 600 °C, the lattice mismatch between $LaF_3$ and GaAs increases to +4.5 % from the RT value of +3.8 %.

In Section 4.3, we will show that $LaF_3$ films on semiconductors have columnar structures. The $LaF_3$ films have defects separating columns of coherent crystals. The separations between defects are found to be equal to the defect spacings required to accommodate the lattice mismatch at the growth temperatures. This suggests that strains in the $LaF_3$ films caused by the lattice mismatch between the fluoride and the substrate are relaxed at the growth temperature by formation of columnar defects.

Between the columnar defects, the fluoride crystals are coherent. We hence expect that the film lattice is registered with the substrate lattice at the film/substrate interface. As the system cools, the $LaF_3$ films have tendencies to contract more than the semiconductor substrate due to their larger thermal expansion coefficients. However, if the columnar defects are pinned at the interface, since the lattices are registered at the interface, the fluoride films are forced to contract according to the thermal contraction of the substrate. This differential thermal contraction can cause the tensile strains in the $LaF_3$ films on GaAs.

As for the RBS study of $CaF_2$ on Si, we will analyse the residual strains in the $LaF_3$ film thickness using the energy balance model by Matthews *et al.* [40] under the assumption that the $LaF_3$ films are relaxed at the growth temperature through some relaxation processes. In the Matthews' model, the strains in the films are relaxed by formation of misfit dislocations by balancing the energy associated with elastic strains due to the lattice mismatch between the film and the substrate, and the energy associated

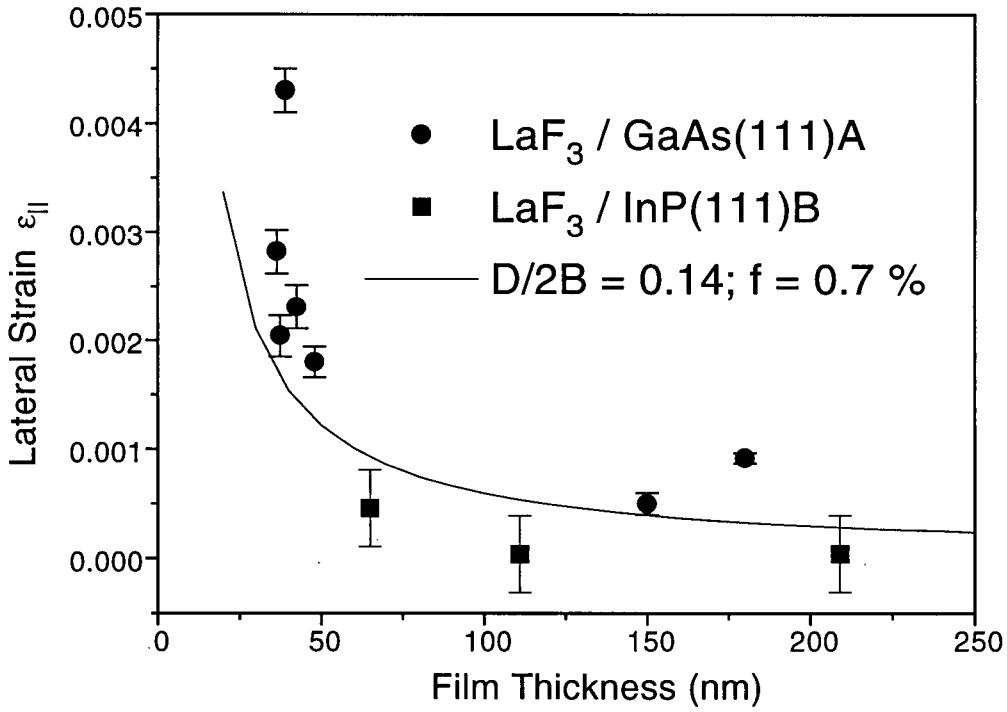


Figure 4.37: Plot of the in-plane tensile strain as a function of the film thickness for the $LaF_3$ film grown on GaAs(111)A and InP(111)B substrates.

with the formation of dislocations accommodating the misfits.

Although the type of defects in the $LaF_3$ films is unknown, we expect that the mechanisms of strain relaxations in the $LaF_3$/GaAs system to be similar to the mechanisms described by the Matthews' model. In the $LaF_3$/GaAs system, the elastic strain energy due to the differential thermal contraction increases with increasing film thickness. Therefore more strain relaxation processes occur in a thicker film than a thinner film. The strain relaxation processes in our system are not necessary a formation of misfit dislocations as in the Matthews' model, but can also be other defect formations or defect motions such as defect slips. Nonetheless, we expect the strain in the $LaF_3$ films to decrease with increasing film thickness as described by the Matthews' model.

The in-plane residual strain $\varepsilon_{||}$ according to the Matthews' model is given by [40]:

$$\varepsilon_{||} = [-\frac{D}{2Bh}] \ln 2(f - \varepsilon_{||}), \tag{4.11}$$

$$D = \frac{G_0 G_s b}{\pi(G_0 + G_s)(1 - \sigma)}$$

In the above expression, $G_0$, $G_s$ are the shear modulus for the film and the substrate respectively, $b$ is the magnitude of the Burgers vector of the dislocations and $\sigma$ is the Poisson ratio of the film. The value of $f$ is the lattice mismatch between the substrate and the film, if no strain relieving process occurs. The constant $B$ for an isotropic film is given as:

$$B = 2G_0(1 + \sigma)/(1 - \sigma) \tag{4.12}$$

The analysis is for an isotropic film. However, since the elastic constants along the principal axes do not vary more than a order of magnitude, we expect the strains given by the analysis to be a good approximation for our $LaF_3$/GaAs system.

The calculated in-plain strain $\varepsilon_{||}$ using the Matthews' model in Eqn. 4.11 is plotted in Fig. 4.37 for the $LaF_3$ films on GaAs. The in-plain strain was calculated under the assumption that the $LaF_3$ films are relaxed at the growth temperature and they contract

according to the thermal expansion coefficient of the substrate. We also assumed in the calculation that the Poisson ratio of the $LaF_3$ film is same as that of the substrate and that the magnitude of the Burger's vector $b$ is $b = a/2$ where $a$ is the lattice constant of $LaF_3$. We used the elastic constants of GaAs and $LaF_3$ ($D/2B = 0.14$). We obtained a good agreement between the calculated in-plain strains and the measured strains. The estimated residual strain $\varepsilon_{||}$ falls within 20 % of the measured residual strains.

We estimated the value of $f$ as follows. The lattice constant at the growth temperature of 600°C of the unstrained $LaF_3$ is $a = 7.264$ Å according to the thermal expansion coefficient of $LaF_3$. If the unstrained $LaF_3$ at 600°C is allowed to cool and it contracts according to the thermal contraction of the substrate then its room temperature lattice constant will be $a' = 7.235$ Å. Thus the expected strain $f$ in the case of no strain relaxation on cooling, is: $f = (a' - a)/a = (7.235 - 7.185)/7.185 = +0.70$ %, which is a tensile strain.

The strains in the $LaF_3$ films grown on InP(111)B substrates were also measured and are plotted in Fig. 4.37. No strains greater than the uncertainty in the measurements $\sim 3 \times 10^{-4}$, were detected. We expect that the strains in the $LaF_3$ films on InP to be less than those on GaAs. As we show later in Section 4.3, the columnar defects in the $LaF_3$ films on InP are less than that on GaAs because the lattice mismatch in $LaF_3$ on InP is less at the growth temperature. Therefore there are less defects pinned at the interface resulting in less strains in the films. We have calculated the strains using the Matthews' model in Eqn. 4.11 assuming that the films are unstrained at the growth temperature and contract according to the thermal contraction of the substrate. The calculated strains for $LaF_3$ on InP overlaps with those for the $LaF_3$/GaAs system, since the strains for $LaF_3$ on InP only differ from those on GaAs by less than 5 %. The calculated strains for $LaF_3$ films on InP are roughly in agreement with the measured strains. The measured residual strains fall within 20 % of the estimated strains taking the uncertainty of the

measurements into account.

The value of $f$ in Eqn. 4.11 is estimated as follows. The lattice mismatch of the system at the growth temperature of 400°C is +0.41 % as compared to −0.04 % at RT. Using the same arguments for the $LaF_3$/GaAs(111)A system, the value of expected strain $f$ without any strain relaxation on cooling from a relaxed state at the growth temperature, for the $LaF_3$/InP(111) system is $f = +0.46$ % as compared to $f = +0.7$ % for the $LaF_3$ film on GaAs. The calculation was performed assuming the magnitude of the Burger's vector of $b = a/2$ where $a$ is the lattice constant of $LaF_3$, and using the elastic constants of InP and $LaF_3$ ($D/2B = 0.12$) with $f = 0.46$.

The strains in the $ErF_3$ films on GaAs(111) shown in Fig. 4.36 were also calculated. The strains along the $b$-axis of $ErF_3$ or along the direction perpendicular to the interface was calculated as $\varepsilon_\perp = 0.0031 \pm 0.0003$ which is a tensile strain. This suggests that $ErF_3$ film is compressively strained along the interface. As we showed in Fig. 4.31, the lattice mismatch of $ErF_3$ on GaAs(111) along the $a$-axis is different from that along the $c$-axis. The mismatch along the $a$-axis is -8.6 % whereas that along the $c$-axis is +9.0 %. The estimation of in-plain strains corresponding to the measured perpendicular strains involves considerations of anisotropic strains along the interface. The calculation of in-plain strains for $ErF_3$ films on GaAs is out of scope of our study.

## 4.3 Crystallinity

The crystallinity of the $LaF_3$ film was studied using X-ray rocking curve measurements. The width of the X-ray rocking curve is associated with the lateral dimension of the coherent region in the crystal [42]. A rocking curve is obtained by scanning the sample axis with detector–source angle fixed. The widths of rocking curves are associated with the lateral coherence lengths $L$ through the relationship: $L \simeq 8 \ln 2/\mathrm{FWHM}$ [43]. That is,

narrower the widths of curves, longer the coherence lengths. Typical rocking curves of the $LaF_3$ (002) peaks for $LaF_3$ films on GaAs(111)A and InP(111)B are shown in Fig. 4.38. The rocking curves were modelled by Gaussian lineshapes. We note that the widths of the rocking curves for $LaF_3$ films on InP are significantly narrower than those for $LaF_3$ on GaAs. This indicates that the lateral coherence lengths or the sizes of coherent crystals in $LaF_3$ on InP are longer. This is expected, since the lattice mismatch in the $LaF_3$/InP system is an order of magnitude smaller than the mismatch in the $LaF_3$/GaAs system. The profiles of rocking curves for $LaF_3$ films on InP suggest that there exists more than one Gaussian peak in the curves. We were able to fit the curves with the sum of two Gaussian functions. This shows that there are regions in the films where the defects are concentrated. The fits with the two Gaussian functions are plotted Fig. 4.38. The Gaussian FWHM and the corresponding coherence lengths obtained from the rocking curves are listed in Table 4.5.

The variation of the FWHM of the X-ray rocking curve and corresponding lateral coherence length with film thickness are plotted in Fig. 4.39. The lateral coherence length increases with increasing film thickness and saturates at 45–55 nm. We note that a part of data points is concentrated near the lateral coherence length 20–30 nm whereas other points are between 45 and 60 nm. This brings up the possibility that the increase in lateral coherence length can also be discontinuous. The discontinuous increase siginifies that there are two distinct regions with different defect concentrations which is consistent with the fit of two-Gaussian curves for the rocking curves of $LaF_3$ on InP shown in Fig. 4.38. In either case, *i.e.* whether continuous or discontinuous, the increase in the coherence length indicates that the concentration of defects is higher near the interface. The coherence lengths for the $LaF_3$/InP(111)B samples are significantly longer, $L_x$ = 80–540 nm than those for the $LaF_3$/GaAs(111)B samples, $L_x$ = 20–60 nm, consistent with the closer lattice match in the $LaF_3$/InP(111) system.

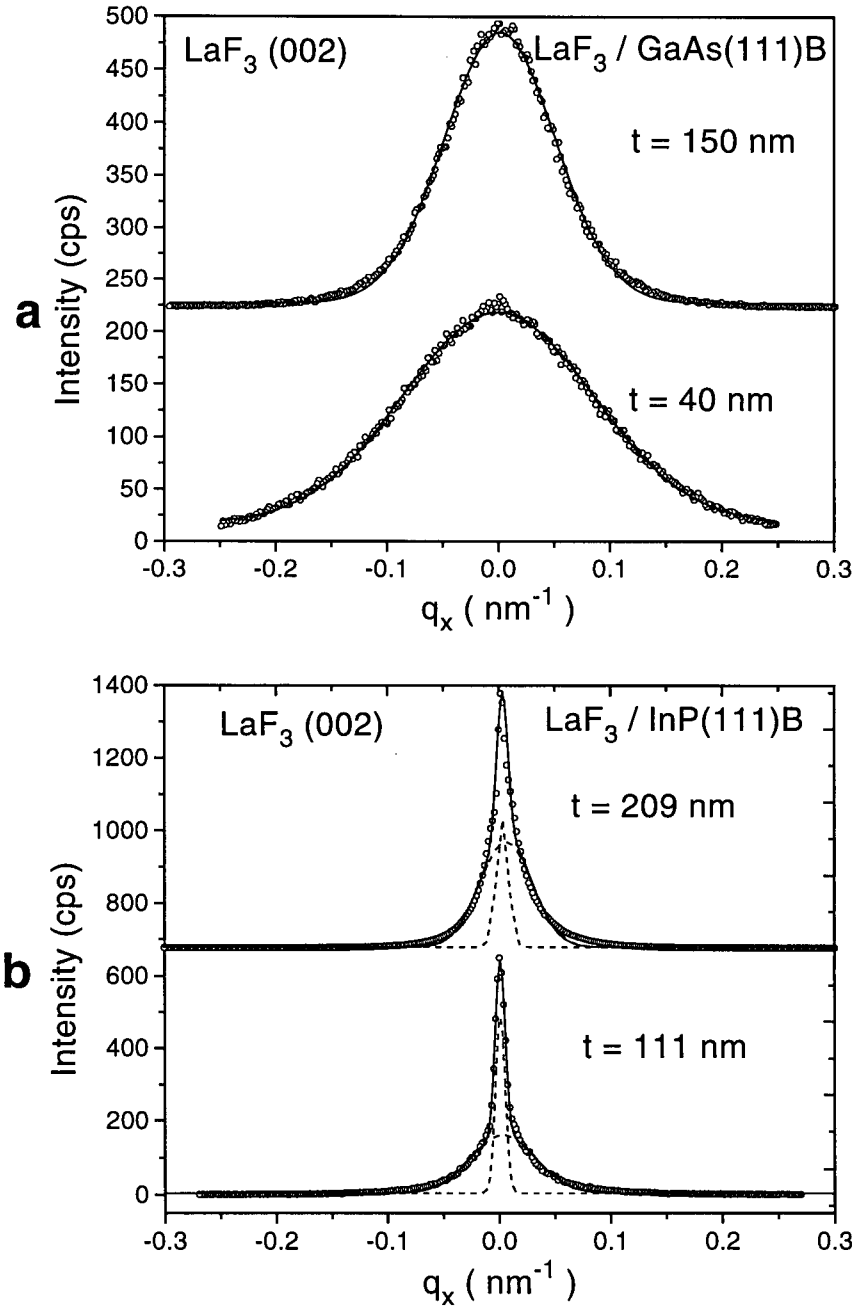


Figure 4.38: X-ray rocking curves of the $LaF_3$(002) Bragg peak for (a) the $LaF_3$/GaAs(111)A and (b) the $LaF_3$/InP(111)B samples with two different thicknesses. Solid lines in (a) are fits of Gaussian to the data. Solid lines in (b) are the fits of two Gaussian functions to the data. Dashed lines are the corresponding individual Gaussian curves for each two Gaussian curve.

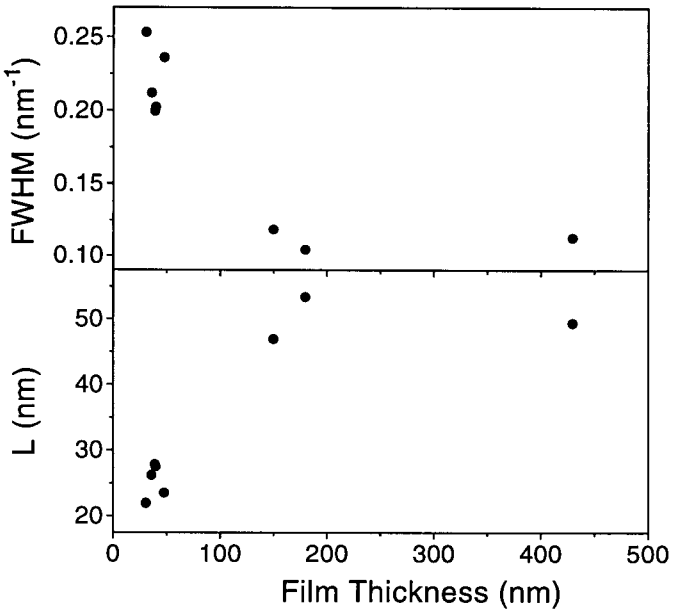


Figure 4.39: Variation of FWHM of the rocking curves and the lateral coherence length with film thickness for the $LaF_3$/GaAs(111)A samples.

Table 4.5: Gaussian FWHM and corresponding lateral coherence lengths $L_x$ for the $LaF_3$/InP(111) samples of different film thicknesses, obtained from the rocking curve measurements. FWHM are obtained using the two-Gaussian function.

| $LaF_3$/InP(111)B thickness (nm) | FWHM (sec) | FWHM (nm$^{-1}$) | L (nm) |
|---|---|---|---|
| 111 | 110 | 0.010 | 540 |
| | 770 | 0.069 | 80 |
| 209 | 180 | 0.013 | 440 |
| | 700 | 0.056 | 100 |

We have also performed a cross-sectional scanning electron microscopy (SEM) on a $LaF_3$/GaAs sample. The SEM image is shown in Fig. 4.40. The cleaved surface shows columnar structures aligned perpendicular to the interface. The columnar defect spacings (50–60 nm) are comparable to the corresponding lateral coherence length measured by rocking curves (47 nm) suggesting that the lateral coherence length represents the separations between the columnar defects.

Columnar structures are commonly observed in polycrystalline thin film growth performed by physical vapor deposition (PVD) such as electron beam deposition and ion sputtering. The structure zone model popularized by Thornton [45] for sputtered films, is widely used in the PVD techniques for predicting the film morphology as a function of growth temperatures. In the structure zone model, the morphology of deposited films is determined by the ratio of the growth temperature $T$ to the melting point of the deposited material, $T_m$. For growth temperature in the approximate range $0.3 \lesssim T/T_m < 0.5$, known as Zone 2, PVD films are found to have a columnar microstructure. The structure results from a tradeoff between diffusive transport processes and shadowing in the presence of an incoming particle flux with a lateral component of the velocity. Due to the roughness on the surface, more particles arrives on the *hills* or the high surface sites than on the *valleys* or the low surface sites which are shadowed by the higher sites. For our $LaF_3$ growth, the temperature $T/T_m$ was $873/1766 \sim 0.5$ for the GaAs substrates and $673/1766 \sim 0.4$ for the InP substrates. These temperature correspond to Zone 2, $T/T_m \gg 0.3$. Thus according to the structure zone model, one would expect a dense columnar structure in which the regions between the columns are filled with the defects. The columnar structure observed in the $LaF_3$ films (see Fig. 4.40) are consistent with the structure predicted by the structure zone model. In the deposition of the $LaF_3$ films, there is a lateral component in the velocity of arriving particles, since the incident beam of particles made an angle 30° with the surface normal. The structure zone model is

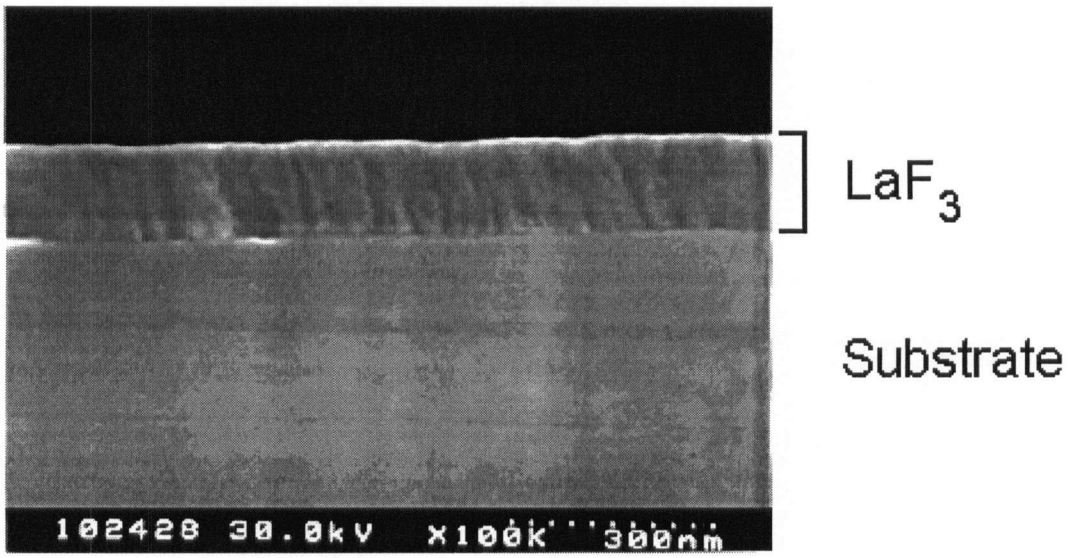


Figure 4.40: Cross sectional SEM image of a $LaF_3$/GaAs(111)A sample with film thickness t = 150 nm. A columnar structure commonly observed in thin film growths, is observed.

not normally applied to the growth of epitaxial films. It is interesting that we observe a similar microstructure in our epitaxial $LaF_3$ films. In the present experiments, we find that the lateral size of the columns is related to the lattice mismatch.

We observed that the $LaF_3$ films on InP which have a smaller lattice mismatch than the $LaF_3$ on GaAs have a longer coherent length or a larger columnar crystal size. The smaller lattice mismatch results in a lower strain in the film which allows larger coherent crystal islands to nucleate, thereby creating larger columns.

From the point of view of epitaxial growth, the columnar defect structure in the $LaF_3$ films should be able to relieve the strain due to the lattice mismatch. In this picture, defects in the fluorides propagate perpendicular to the interface as opposed to along the interface as in the case of covalent semiconductors. The difference may be due to the fact that there are no directional covalent bonds in fluorides and consequently one would expect the strain relieving defects to be quite different.

To see if the lateral coherence lengths are related to the strain relieving defects in the $LaF_3$ films, we estimate the spacing of structural defects required to accomodate the misfit at the growth temperature and compare this with the lateral coherence lengths for the $LaF_3$ films on GaAs and InP. For convenience in the analysis, we assume that the strain relieving defects are misfit dislocations. The spacings for misfit dislocations for the lattice mismatch $\delta$ is given by: $S = b/\delta$ where $b$ is the magnitude of the Burger's vector of dislocation. The defect spacings $S$ were calculated using the lattice mismatch at the growth temperatures. For the $LaF_3$/GaAs(111) system, the defect spacing will be 8 – 16 nm assuming $b = a/2 - a$. The coherence lengths for the $LaF_3$ films on GaAs were 20–60 nm. Similarly, the defect spacing for the $LaF_3$/InP(111) system is 90 – 180 nm. The lateral coherence lengths for this system were 80–540 nm. The estimated defect spacing are comparable to the measured lateral coherence lengths for both systems. We can interpret that the columnar defects are formed at the growth temperature to accomodate the lattice mismatch between the film and the substrate. The defect spacings in the $LaF_3$ films on InP are longer than those on GaAs because the lattice mismatch in the $LaF_3$/InP system is an order of magnitude smaller. The relationship between the lateral coherence lengths and the lattice mismatch at the growth temperatures can be also observed by comparing the ratios of $LaF_3$/GaAs to $LaF_3$/InP for the two values. The ratios of the lateral coherence lengths for the $LaF_3$ films on GaAs and InP substrates are 4–9. The ratio of the coherence length is comparable to the ratio $R$ of the lattice mismatch $\delta$ at the growth temperatures of the two systems: $R = \delta_{GaAs}/\delta_{InP} = 4.5\%/0.41\% \simeq 11$.

## 4.4 Summary

We have investigated the structural properties of $LaF_3$ and $ErF_3$ films grown on III-V semiconductors. We have shown by X-ray diffraction that the $LaF_3$ and $ErF_3$ films

on GaAs and InP are single crystals. The epitaxial growth of $LaF_3$ films on InP is demonstrated for the first time. In the $LaF_3$/GaAs(111)A and $LaF_3$/InP(111)B systems, we have shown that the trigonal $a \times a$ plane of the $LaF_3$ crystal is aligned parallel to the (111) hexagonal face of GaAs and InP substrates by X-ray diffraction and LEED. This result is in agreement with LEED and RHEED study of the $LaF_3$/GaAs(111) system by Sinharoy *et al.* [5].

In the $ErF_3$/GaAs(111)B system, the orthogonal $a \times c$ plane of the $ErF_3$ film is found to be oriented parallel to the (111) plane of the GaAs substrate by XRD. The result is consistent with the the LEED study of $GdF_3$ deposited on Ge(111) and GaAs(111)B substrates by Jenkins *et al.* [10].

We observed a columnar structure in the $LaF_3$ film grown on a GaAs(111) substrate. The $LaF_3$ film growth was done in the temperature range, Zone 2 in which the film is expected to have a dense columnar structure. The columnar structure results from the competition between the diffusive transport process and the shadowing in the presence of an incoming particle flux with a lateral component of velocity. The effect of the lattice mismatch on the column size may be associated with the initial size of the nuclei. The film/substrate interface energy is lower for a smaller lattice mismatch system where the strain is lower. It is hence thermodynamically favorable for a small lattice mismatch system to form larger size nuclei.

From the epitaxial growth point of view, the columnar defects relieve the strain due to the lattice mismatch. The lateral coherence lengths of the $LaF_3$ films on GaAs and InP obtained by X-ray rocking curve measurements were comparable to the defect spacing required to accommodate the lattice mismatch at the growth temperature. The lateral coherence lengths for the $LaF_3$ films on InP were longer than on GaAs, since the lattice mismatch for the $LaF_3$/InP system is lower. In this picture, the columns of coherent crystals are surrounded by regions of defects propagated perpendicular to

the film/substrate interface and that the defects are formed to accommodate the lattice mismatch at the growth temperature. The propagation of defects in fluorides is different from that in semiconductors where the dislocations propagate along the film/substrate interface rather than perpendicular to the interface. This may be because in fluorides as opposed to for the semiconductors. The energy necessary for defects to propagate in the films is lower due to the ionic character of the bonds in fluorides than in the semiconductors.

The columnar structure of $LaF_3$ films is consistent with tensile strains observed in $LaF_3$ films on GaAs by high-resolution X-ray diffraction (HRXRD). We interpret that the tensile strains in the $LaF_3$ films are due to the differential thermal contraction between the fluorides and the semiconductors during cooling. According to our interpretation, the $LaF_3$ films relieve strains due to the lattice mismatch at the growth temperature by formation of columnar regions of defects. $LaF_3$ films have tendencies to contract more than semiconductor substrates during cooling due to their greater thermal expansion coefficients. However, since the $LaF_3$ lattice is registered with the substrate lattice at the interface, if the defects are pinned at the interface, the films are unable to accommodate the differential thermal contractions. This results in tensile strains in the $LaF_3$ films. The tensile strains were not detected in the $LaF_3$ films on InP than on GaAs, since the lattice mismatch is smaller in the $LaF_3$/InP system. This is also consistent with our interpretation, since the number of defects that are pinned at the interface will be lower in $LaF_3$ films on InP than on GaAs, since the lattice mismatch in the $LaF_3$/InP system is smaller. Hence the $LaF_3$ films on InP are able to accommodate the differential thermal contraction during cooling through processes such as defect motions. Consequently there are less strains in the $LaF_3$ films on InP than on GaAs.

We conclude that the lattice mismatch as well as the difference in thermal expansion coefficients between the film and the substrate are important factors in the structural

perfection of deposited fluoride film in the rare-earth trifluoride/III-V semiconductor system.

# Chapter 5

## Surface Morphology

In this chapter, we will examine the surface morphology of the $LaF_3$ films grown on GaAs and InP. The surface and interface roughness in electronic and optoelectronic devices is one of the factors affecting the device performances such as carrier mobilities and optical losses. Therefore it is important to investigate the surface and interface roughness in the fluoride/semiconductor system. Our objective is to determine the surface and interface roughness of the $LaF_3$/GaAs, InP system. Another objective to apply a self-affine surface structural analysis to our fluoride/semiconductor system and to see if it can provide an insight into physical mechanisms by which fluorides grow on semiconductors.

Self-affine surfaces are invariant under anisotropic transformations. That is if we enlarge a self-affine surface in a direction, for example in the $x$-direction, differently than in the other direction, for example in the $z$-direction, then the surface looks the same. The scaling of a self-affine surface is schematically illustrated in Fig. 5.41. Consider that the height of a self-affine surface is described by a function $h(x)$ where $x$ is the horizontal direction of the surface. If we enlarge the height function $h(x)$ horizontally by a constant factor $b$ ($x \rightarrow bx$), the $h(x)$ is enlarged by a factor $b^\alpha$ vertically ($h \rightarrow b^\alpha h$) where $\alpha$ is the *roughness* or scaling exponent. In other words, the $h(x)$ has the following property:

$$h(x) \propto b^{-\alpha} h(bx) \tag{5.13}$$

The self-affine description of surfaces can be used to study the growth phenomena of

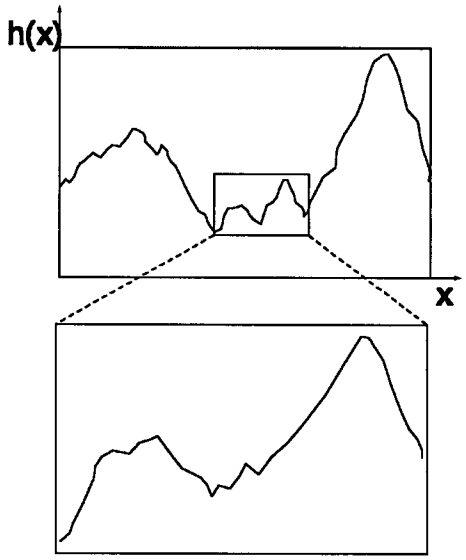


Figure 5.41: Schematic illustration of the scaling of a self-affine surface. If we enlarge a self-affine surface horizontally in a direction, for example in the $x$-direction, differently than in the other direction, for example in the $z$-direction, then the surface looks the same.

the surfaces. The self-affine surfaces which have same or similar mechanisms of formation, have same scaling exponents. The self-affine surfaces which scale in a similar way do not necessary have a same structure in microscopic detail, but have some essential factors that are common during their formations. The physical mechanisms by which self-affine surfaces are formed can be described by various theoretical models. These theoretical models also have scaling properties or have scaling exponents associated with them. Therefore by measuring the scaling exponents of the system of our interest from measurable quantities and by comparing the measured exponents with those predicted by theoretical models, we can learn about the mechanisms of formation of that system. The self-affine surface description is a convenient way to parameterise surface structures and to compare experiments with theoretical models.

To determine the scaling exponents from experiments, we assume that the surface

height $h(x)$ is Gaussian distributed about a mean height as shown in Fig. 5.42 for a case of one-dimensional surfaces. We describe the height-height correlation function of the surface by a function of the form [49, 46]:

$$C(x) = \langle z(0)z(x)\rangle = \sigma^2 e^{-(x/\xi)^{2\alpha}} \tag{5.14}$$

where $z(x) = h(x) - \langle h(x)\rangle$, $\sigma = \sqrt{\langle z(x)^2\rangle}$, the rms width of the surface, $\alpha$ is the roughness exponent and $\xi$ is the correlation length of the surface roughness. The roughness exponent gives a quantitative measurement of the roughness of the function $h(x)$. The lower the value of $\alpha$, the more jagged the surface looks or there will be more high-frequency, low amplitude contributions to the surface profile. The higher the value of $\alpha$, the more smooth the surface looks. The correlation length $\xi$ measures the length scale of the surface structure of the system studied. Two points separated by a distance longer than the correlation length $\xi$ are not correlated and hence, the structures of the length scale $\xi$ can be considered random. For a two-dimensional surface, the $x$ in Eqn. 5.14 is replaced by: $r = \sqrt{x^2 + y^2}$.

The rms width or rms roughness $\sigma$ of a self-affine surface scales with the time $t$ and the sample size $L$. At time $t$ less than the saturation time $t_x$, $t \ll t_x$, the $\sigma$ scales as $\sigma \propto t^\beta$ where $\beta$ is the *growth exponent.* At $t \gg t_x$, the rms roughness $\sigma$ is independent of time and scales as $\sigma \propto L^\alpha$ where $L$ is the sample size and $\alpha$ is the *roughness exponent.* It is usually assumed that the growth rate is linear in time so that the film thickness is used as $t$ in the above relationships. For $t \ll t_x$, the correlation length $\xi$ of the surface roughness scales as $\xi \propto t^{1/z}$ where $z$ is the *dynamic exponent* given by $z = \alpha/\beta$. For $t \gg t_x$, the correlation length $\xi$ is proportional to the sample size i.e. $\xi \propto L$.

In this study, the scaling exponents $\alpha$, $\beta$, the surface roughness $\sigma$ and the correlation length $\xi$ for the $LaF_3$ films grown on GaAs and InP substrates are obtained using the X-ray specular and diffuse scattering, and the atomic force microscopy (AFM). The scaling

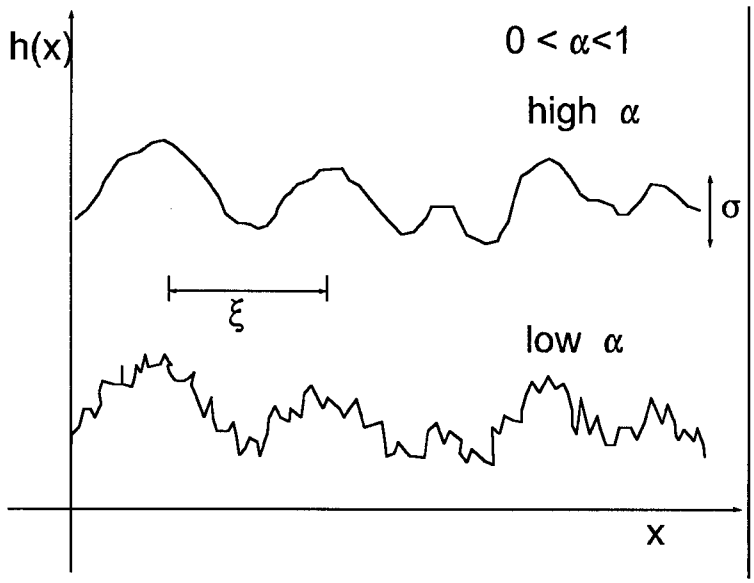


Figure 5.42: Schematic illustration of a self-affine surface showing the parameters that describe it. The surface height is assumed to be Gaussian distributed around a mean height. The $\sigma$ is the rms width of the surface, the $\alpha$ is the roughness exponent and the $\xi$ is the correlation length of the surface roughness. The roughness exponent gives a quantitative measurement of the roughness of the function $h(x)$. The lower the value of $\alpha$, the more jagged the surface looks or there will be more high-frequency, low amplitude contributions to the surface profile. The higher the value of $\alpha$, the more smooth the surface looks. The $\xi$ measures the length scale of the surface structure of the system studied. Two points separated by a distance which is more than the correlation length $\xi$ are not correlated and hence, the structures of the length scale $\xi$ can be considered random.

exponents for the system are compared with the ones predicted by known growth models.

## 5.1 X-ray Scattering

In X-ray scattering experiments, samples are illuminated by a beam of X-rays and the intensity of scattered X-rays is measured. We have used a Cu K$\alpha$ radiation as the X-ray source. The geometry for X-ray scattering experiments is schematically illustrated in Fig. 5.43. In the figure, the $\mathbf{k_1}$ and $\mathbf{k_2}$ are the wavevectors of incident and detected beams respectively. The $\theta_1$ and $\theta_2$ are the angles of incidence and detection. The transfervector $\mathbf{q}$ is defined as $\mathbf{q} \equiv \mathbf{k}_2 - \mathbf{k}_1$. The direction parallel to the interface in the plane of incidence is $x$ and the direction perpendicular to the plane of the interface is $z$. The $y$ direction is perpendicular to the plane of incidence ($x$-$z$ plane). A narrow slit is used at the detector. The angle subtended by the detector slit is $\Delta\theta_2 = 0.0014$ rad. The slit is wide in the $y$ direction.

The rms interface width $\sigma$ and the film thickness $t$ are obtained from the specular intensity of X-rays (intensity when the angle of detection is equal to the angle of incidence) using the recursive method for stratified layers by Parratt [47]. The effect of the roughness is implemented using the expression for the specular reflectivity $R$ by Nevot and Croce [48]:

$$R = R_f e^{-q_z q_z^t \sigma^2} \tag{5.15}$$

In the expression, $q_z$ and $q_z^t$ are the components of the transfervectors, perpendicular to the plane of the interface for the layer above and below the interface respectively. The $\sigma$ is the rms width of the interface and $R_f$ is the fresnel reflectivity for an ideal interface. The method by which the specular reflectivity is calculated, is described in detail in Appendix C.

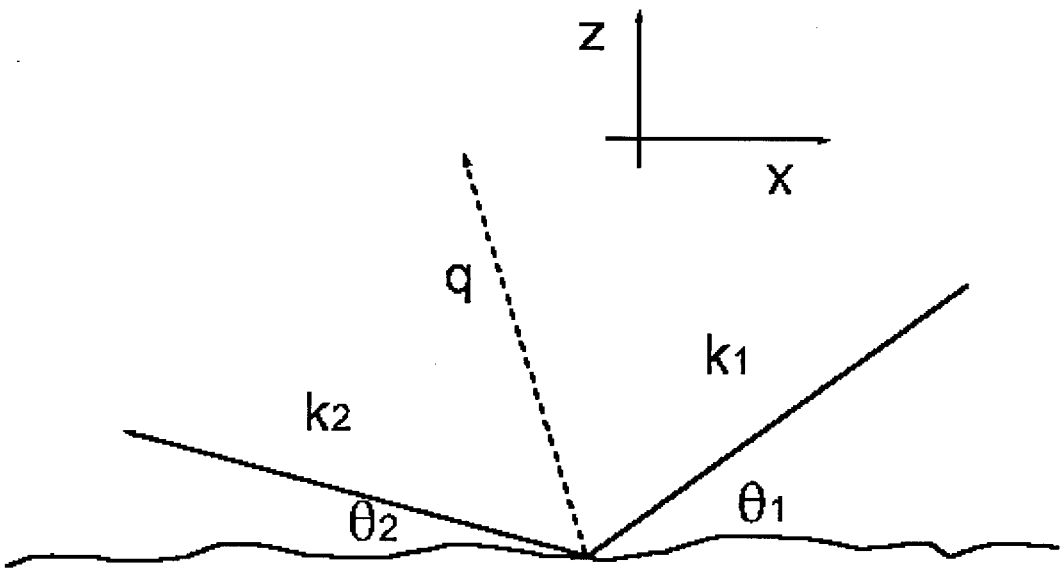


Figure 5.43: Schematic illustration of X-ray experiment geometry. The $\mathbf{k_1}$ and $\mathbf{k_2}$ are the wavevectors of incidence and detected beams respectively. The $\theta_1$ and $\theta_2$ are the angles of incidence and detection. The transfervector $\mathbf{q}$ is defined as $\mathbf{q} \equiv \mathbf{k}_2 - \mathbf{k}_1$. The direction parallel to the interface in the plane of incidence is $x$ and the direction perpendicular to the plane of the interface is $z$. The $y$ direction is perpendicular to the plane of incidence ($x$-$y$ plane). A narrow slit is used at the detector. The angle subtended by the detector slit is $\Delta\theta_2 = 0.0014$ rad. The slit is wide in the $y$ direction.

The X-ray diffuse intensity for a single interface is given by Sinha *et al.* [49]:

$$\frac{I_{diff}}{I_0} = \frac{2\pi\Delta\theta_2|\Delta\rho|^2}{k_0 \sin\theta_1}|T(k_1)|^2|T(k_2)|^2\frac{e^{-[q_z^{t\,2}+q_z^{t\,*2}]\sigma^2/2}}{|q_z^t|^2}\int[e^{|q_z^t|^2C(x)}-1]e^{iq_x x}dx \qquad (5.16)$$

where $I_0$ is the incident intensity, $\theta_1$ and $\theta_2$ are the angles of incidence and detection, $k_1$ and $k_2$ are the wavevectors of the incident and detected beams, $\Delta\theta_2$ is the angle subtended by the detector slit, $k_0 = 2\pi/\lambda$ is the wavevector of the Cu K$\alpha$ radiation, $\Delta\rho$ is the density difference at the interface, $q_z$ and $q_x$ are the transfer vectors perpendicular and parallel to the interface. Since a narrow slit ($\Delta\theta_2 = 0.0014$ rad) is used at the detector, the intensity is integrated from $+\infty$ to $-\infty$ in the $y$-direction (the direction perpendicular to the plane of incidence). The diffuse intensity is related to the correlation length $\xi$ and the roughness exponent $\alpha$ through the correlation function $C(x) = \langle z(0)z(x)\rangle = \sigma^2 e^{-(x/\xi)^{2\alpha}}$. The fluoride/semiconductor system in this study involves two interfaces: air/film and film/substrate interfaces. The diffuse intensities were thus calculated using the expression of the diffuse intensity for two interfaces similar to Eqn. 5.16, given by Sinha *et al.* [50]. The calculation of diffuse intensity for two interfaces is described in Appendix C.

For each sample, the roughness exponent $\alpha$ is first determined from a *longitudinal scan* using the asymptotic limit for the diffuse intensity from Eqn. 5.16. The asymptotic limit for the diffuse intensity of Eqn. 5.16 when $q_z \gg 1/\sigma$ and $q_x \ll 1/L_x$, where $L_x$ is the lateral size of the sample, is given by [49]:

$$I(q_z) \propto q_z^{-(3+1/\alpha)}\sigma^{-1/\alpha} \qquad (5.17)$$

The correlation length $\xi$ is next obtained from a *transverse diffuse scan* using the expression of the diffuse intensity for two interfaces in Appendix C with the values of $\sigma$ and $\alpha$ determined from the specular and longitudinal diffuse scan. The paths of the longitudinal and transverse diffuse scans in reciprocal space are illustrated in Fig. 5.44. The specular scans are along the $q_z$ axis.

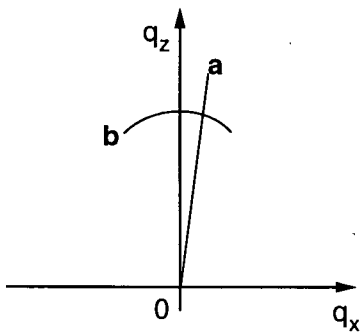


Figure 5.44: Schematic illustrations of (a) longitudinal and (b) transverse scans in reciprocal space.

## 5.2 Variation of the rms surface roughness $\sigma$ with film thickness and the growth exponent $\beta$

The rms interface width $\sigma$ is determined from X-ray specular reflectivity. The geometry of a specular scan is illustrated in Fig. 5.45. The reflectivity $R$ as a function of the momentum transfer perpendicular to the film/substrate interface $q_z$ for the $LaF_3$/GaAs(111)B system is plotted in Fig. 5.46. The calculated specular reflectivities are shown by solid lines in the figure. The rms surface roughness $\sigma$ determined by the fit of the specular reflectivity ranged between 0.5 and 1.0 nm. The film/substrate interfacial roughness determined also from the recursive method for stratified layers [47], varied from 1.0 to 1.5 nm. No trend was observed in the variation of film/substrate interface roughness with thickness. The variation of the rms surface roughness $\sigma$ with film thickness $t$ is plotted in Fig. 5.48. The growth exponent $\beta$ determined from the linear fit of $\log\sigma$ vs. $\log t$ plot using the scaling relationship $\sigma \propto t^{\beta}$ is found to be $\beta = 0.18 \pm 0.16$. If we exclude the data point for the sample with film thickness $t = 150$ nm, the value is $\beta = 0.22 \pm 0.06$.

The specular scans for the $LaF_3$/InP(111)B samples are shown in Fig. 5.47. The rms surface roughness determined from the specular reflectivity fit ranged between 0.5 to

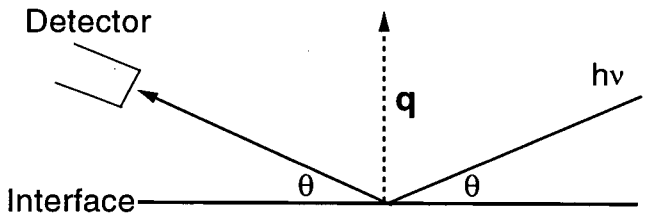


Figure 5.45: Schematic illustrations of the geometry of specular scans in the plane of incidence.

0.8 nm, but no significant trend was observed. The film/substrate interfacial roughness determined also from the fit specular reflectivity using the recursive method for stratified layers [47], ranged between 0.7 to 0.8 nm and no trend was detected with the thickness. The growth exponent $\beta$ for this system is determined as $\beta = -0.1 \pm 0.2$.

## 5.3 Roughness exponent $\alpha$ and the correlation length $\xi$

A longitudinal diffuse scan is a $\theta$–$2\theta$ scan at an off-specular condition obtained by tilting the detector by a small angle away from the specular angle. The geometry of a longitudinal diffuse scan is illustrated in Fig. 5.49. Typical longitudinal diffuse scans for the $LaF_3$/GaAs(111)A and $LaF_3$/InP(111)B samples at off-set angles of $\Delta\theta = 0.09°$ and 0.18° are shown in Fig. 5.50. The off-set angles are larger than the aperture size of the detector which is 0.08°. The solid lines in the figure are linear regressions for determining the roughness exponent $\alpha$ using the asymptotic limit for the diffuse intensity in Eqn. 5.17.

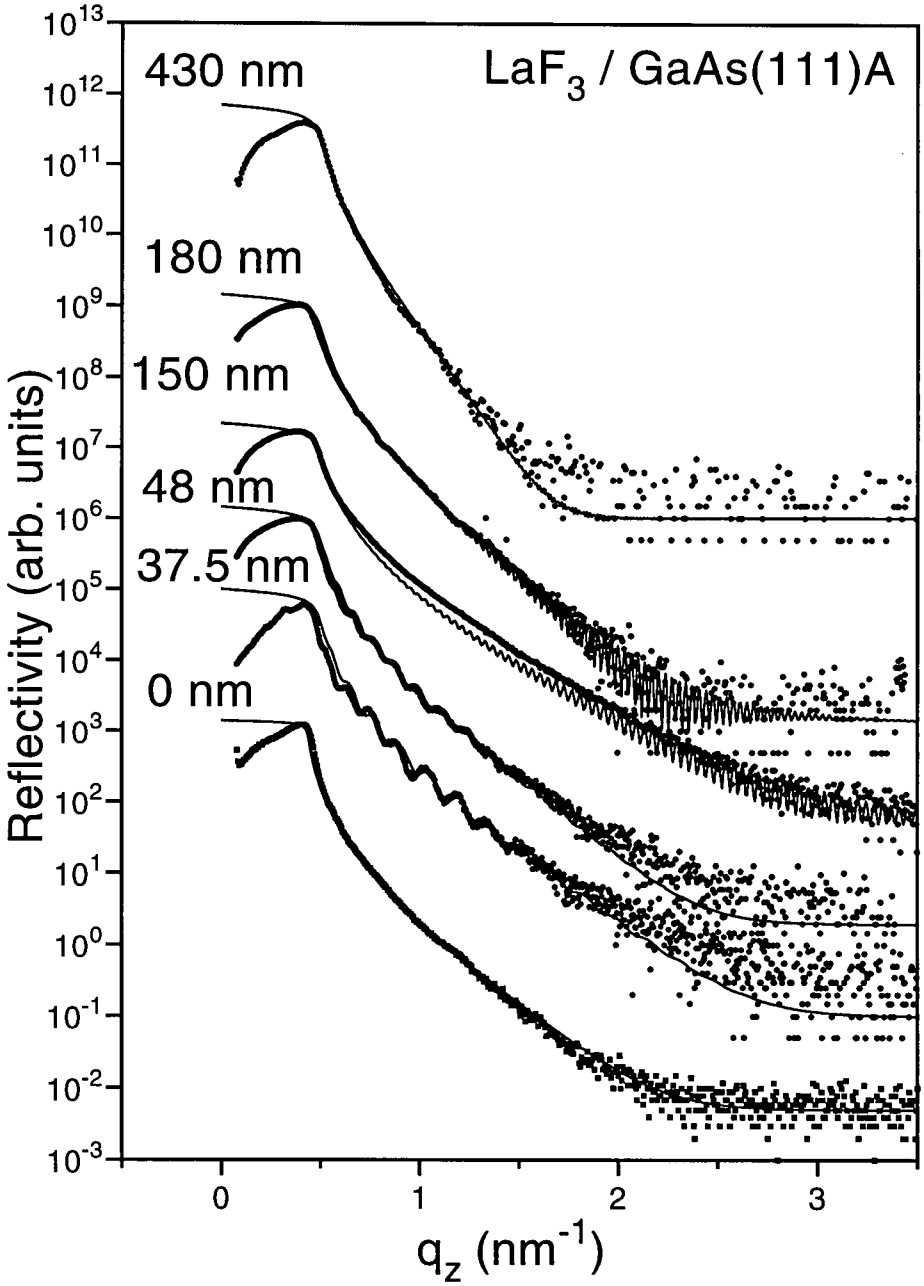


Figure 5.46: Specular reflectivities of $LaF_3$/GaAs(111)A samples. The film thickness is indicated for each sample. The solid lines are the fits of the stratified layer models to the data.

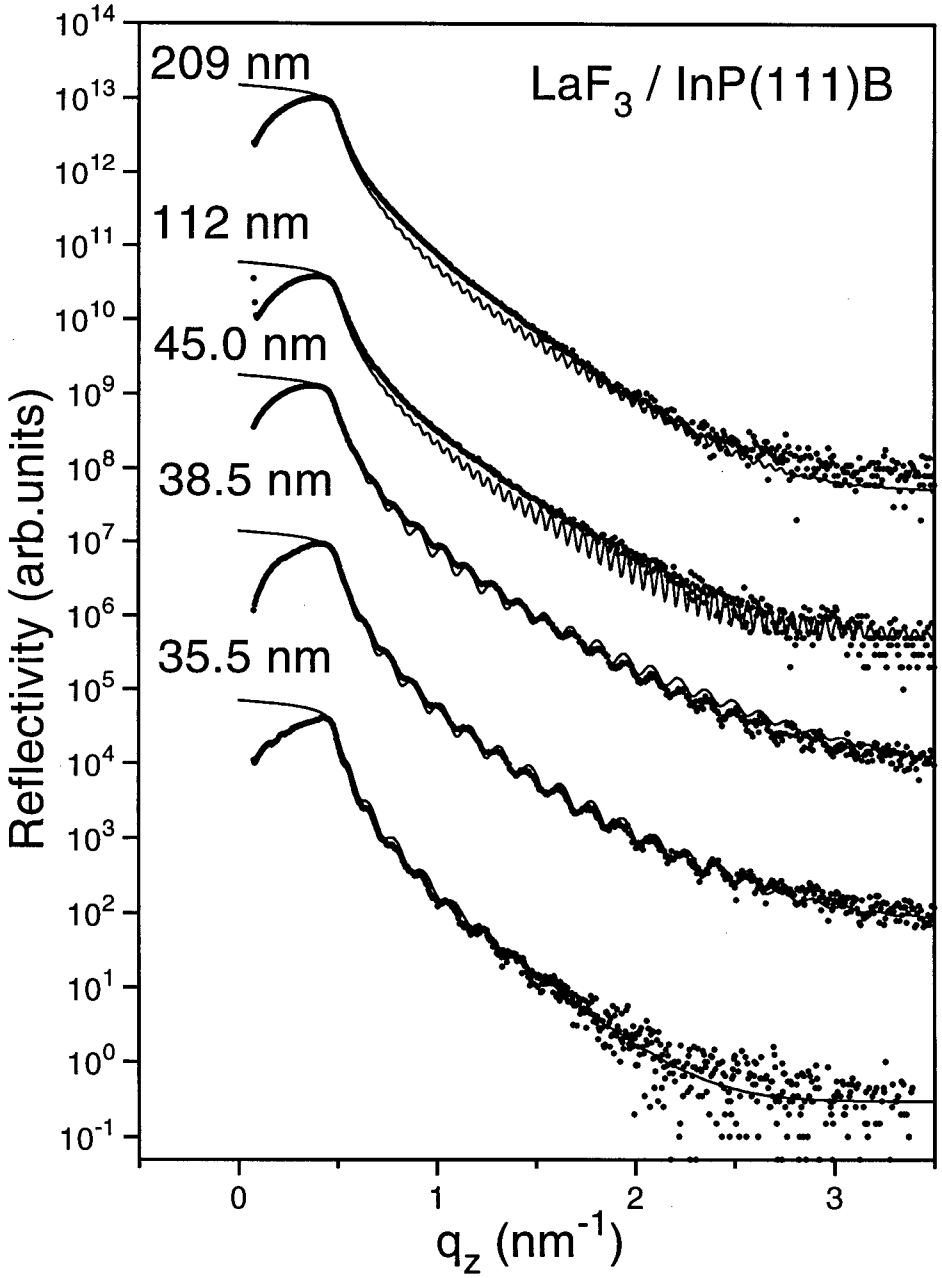


Figure 5.47: Specular reflectivity scans of $LaF_3$/InP(111)B samples. The film thickness $t$ is indicated for each sample. The solid lines are the fits of the stratified layer models to the data.

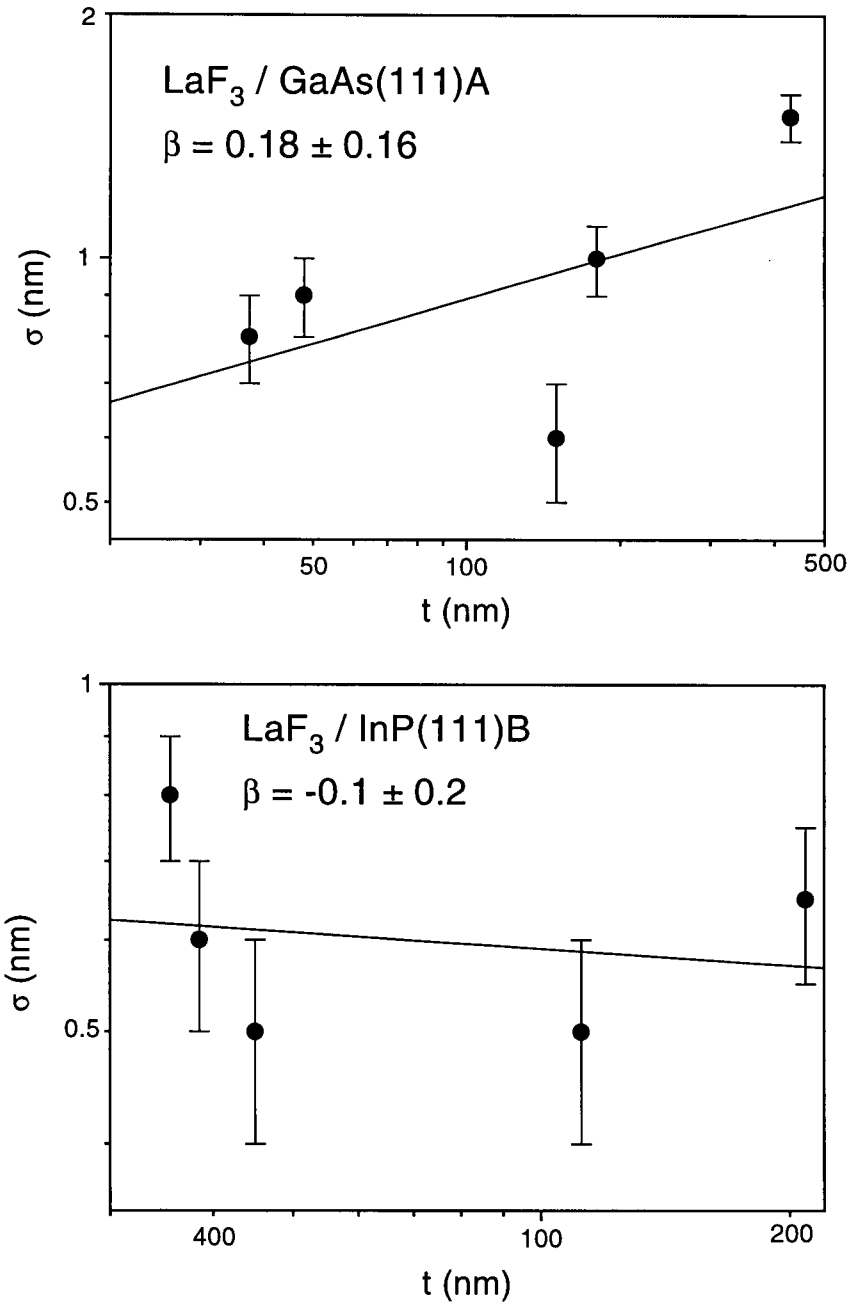


Figure 5.48: Film/air interface width $\sigma$ vs. film thickness $t$ for the $LaF_3$/GaAs(111)A (top) and $LaF_3$/InP(111)B (bottom) systems. The growth exponents $\beta$ determined from the linear fits of the data were $\beta = 0.18 \pm 0.16$ for the $LaF_3$/GaAs(111)A system and $\beta = -0.1 \pm 0.2$ for the $LaF_3$/InP(111)B system.

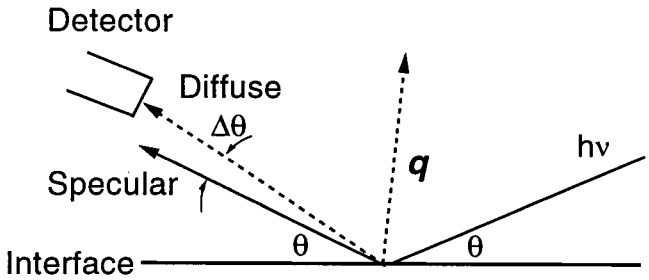


Figure 5.49: Schematic illustration of the geometry of longitudinal diffuse scans in the plane of incidence. The detector is positioned at an angle $\Delta\theta$ away from the specular beam and then a $\theta$–$2\theta$ scan is performed.

The linear fits are obtained near the region $q_z = 1$–$2$ nm$^{-1}$. Corresponding length scales for the two off-set angles are listed in Table 5.6. The roughness exponent $\alpha$ obtained from the scans are also listed in Table 5.6. The errors in the roughness exponents are from the linear regression and do not include the systematic errors which are expected to be larger.

The values of roughness coefficients were different at the two off-set angles within the same system. However, the roughness exponents $\alpha$ at each off-set angle of the $LaF_3$/GaAs(111)A and $LaF_3$/InP(111)B systems are equal within the experimental accuracy. The roughness exponent $\alpha$ determined by analysing the specular reflectivity in the same way for the $LaF_3$/GaAs and $LaF_3$/InP samples shown in Fig 5.50 were $\alpha = 0.3 \pm 0.1$. The roughness exponent $\alpha$ determined at $\Delta\theta = 0.09°$ lies between 0.3 and 0.4 and the exponents determined at $\Delta\theta = 0.18°$ lies between 0.5 and 0.7 for the $LaF_3$ films on both GaAs(111) and InP(111) substrates.

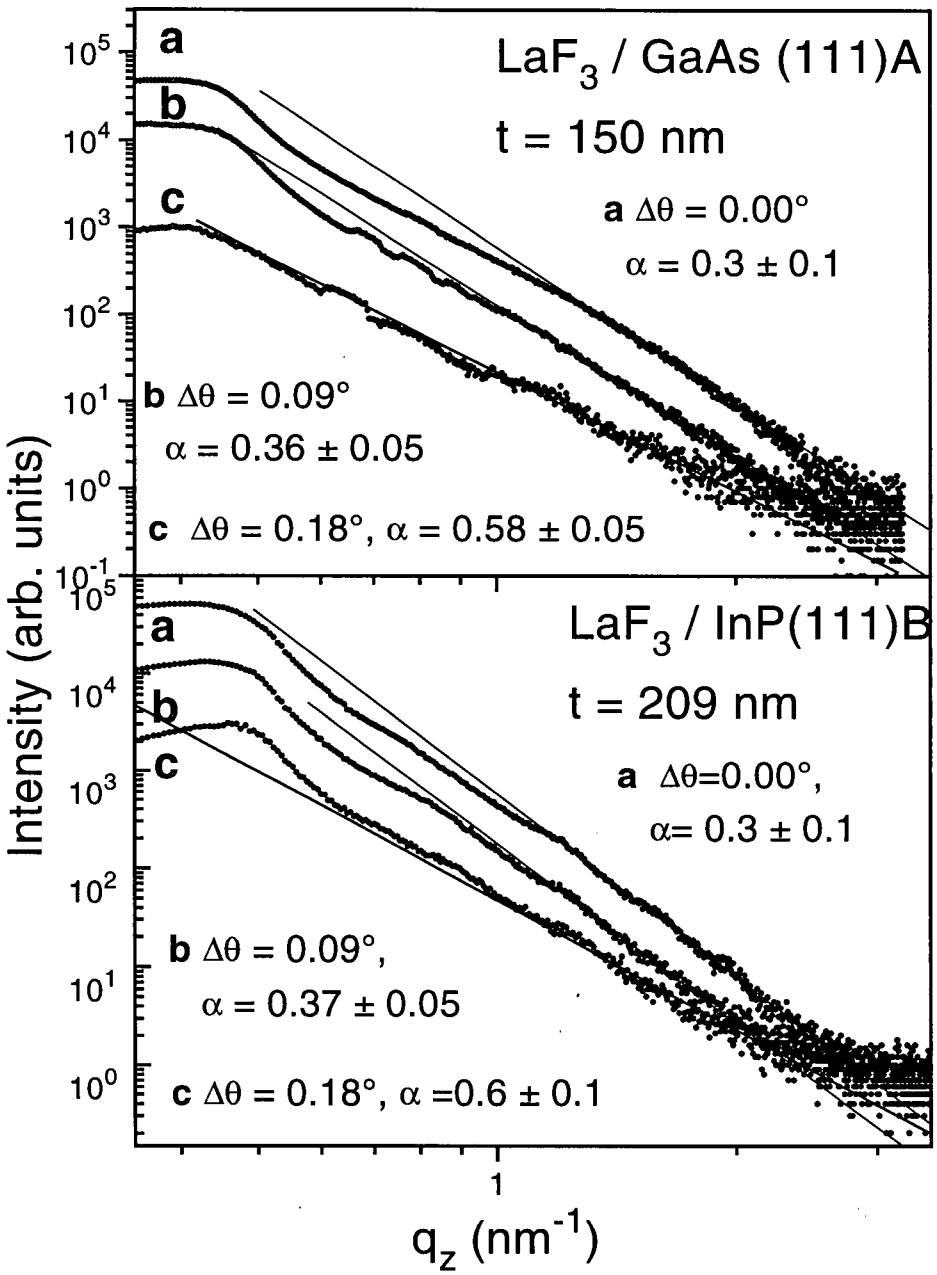


Figure 5.50: Longitudinal diffuse scans taken at an offset angle $\Delta\theta = 0.09°$ and 0.18° for (a) $LaF_3$/GaAs(111)A, t = 150 nm and (b) $LaF_3$/InP(111)B, t = 209 nm. Solid lines are the linear fits to the data.

Table 5.6: Roughness exponent $\alpha$ obtained from the longitudinal diffuse scans for $LaF_3$/GaAs(111)A and $LaF_3$/InP(111)B samples. The range in the x-component of the transfer vector, $q_x$ and corresponding length scale $L_x$ where the longitudinal scans were performed, are also listed.

| Film thickness (nm) | | $\alpha$ | |
|---|---|---|---|
| | $\Delta\theta$ | 0.09° | 0.18° |
| | $q_x$ range ($10^{-3}$ nm$^{-1}$) | 0.7–1.5 | 1.6 – 3.0 |
| | $L_x$ range (nm) | 4000–8000 | 2000–4000 |
| $LaF_3$/GaAs(111)A | | | |
| 37.5 | | $0.36 \pm 0.05$ | $0.66 \pm 0.04$ |
| 48 | | $0.38 \pm 0.05$ | $0.54 \pm 0.05$ |
| 150 | | $0.36 \pm 0.05$ | $0.58 \pm 0.05$ |
| 180 | | $0.36 \pm 0.06$ | $0.6 \pm 0.1$ |
| $LaF_3$/InP(111)B | | | |
| 111 | | $0.37 \pm 0.06$ | $0.53 \pm 0.05$ |
| 209 | | $0.37 \pm 0.07$ | $0.6 \pm 0.1$ |

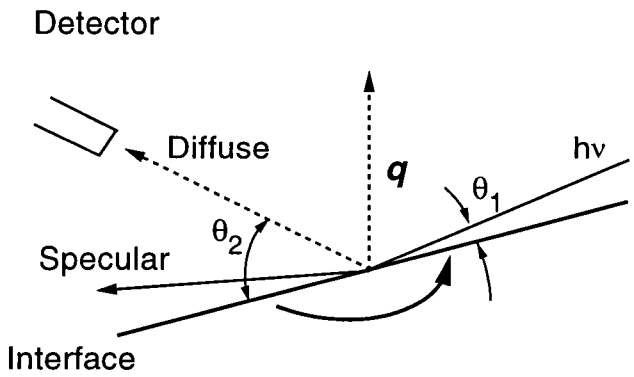


Figure 5.51: Schematic illustration of the geometry of a transverse diffuse scan in the plane of incidence. A transverse scan is performed by rotating the sample around the specular reflection with source-detector angle $2\theta$ fixed.

The correlation lengths $\xi$ are obtained from the transverse diffuse scans using the expression for the X-ray diffuse intensity for two interfaces (see Appendix C) [50]. A transverse diffuse scan is analogous to a rocking curve for a Bragg reflection and is obtained by rotating the sample around the specular reflection with source-detector angle $2\theta$ fixed. The geometry of a transverse diffuse scan is illustrated in Fig. 5.51.

The transverse diffuse scans for $LaF_3$/GaAs(111)A and $LaF_3$/InP(111)B samples are shown in Fig. 5.52. The peak at $q_x = 0$ in each scan is specular reflection. The two peaks at both sides of the specular beam are often referred to as the *Yoneda wings*. They arise when one of the incident or detected beam is at the total reflection condition.

The transverse diffuse scans are the most sensitive to the correlation length $\xi$. The solid and dashed lines in the figure are the calculated diffuse intensities with minimum and maximum values of correlation lengths, using the values of $\sigma$ and $\alpha$ obtained from the specular and the longitudinal diffuse scans. The fits of the transverse diffuse scans

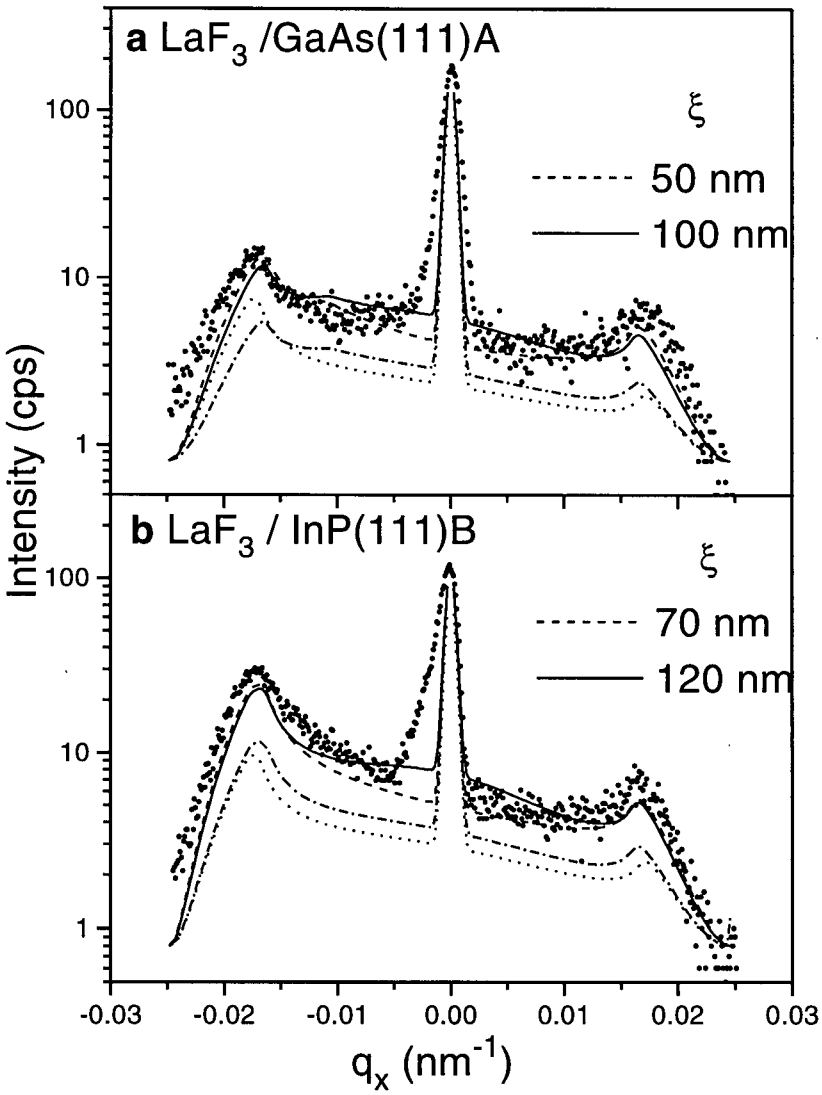


Figure 5.52: Transverse X-ray diffuse scans with $2\theta = 2°$ for (a) the $LaF_3$/GaAs(111)A sample with t = 150 nm and (b) the $LaF_3$/InP(111)B sample with t = 210 nm. The solid and dashed lines are the calculated diffuse intensity using the expression for diffuse intensities for two interfaces given by Sinha *et al.* in Ref. [50]. The coefficients used are (a) $\sigma_0 = 0.5$ nm (film/air), $\sigma_1 = 1.5$ nm (film/substrate) (b) $\sigma_0 = 0.65$ nm, $\sigma_1 = 1.5$ nm for the rms interface roughness and $\alpha = 0.6$ for the roughness exponent for both samples with the cut-off lengths $\xi$ indicated. The dash-dot lines are the diffuse intensities assuming the two interfaces are uncorrelated, using the same parameters as the correlated interfaces with (a) $\xi = 75$ nm and (b) $\xi = 85$ nm. The dotted lines are the diffuse intensities calculated assuming there is only one interface (film/air) using (a) $\sigma = 0.5$ nm, $\alpha = 0.6$, $\xi = 75$ nm and (b) $\sigma = 0.65$ nm, $\alpha = 0.6$ and $\xi = 85$ nm.

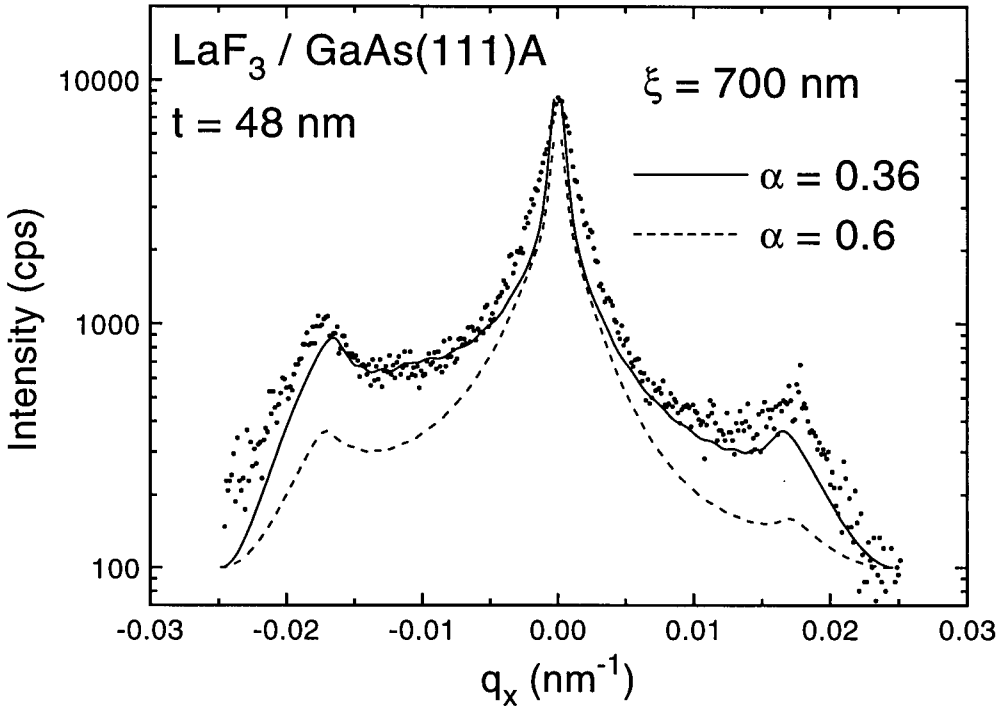


Figure 5.53: Transverse X-ray diffuse scans with $2\theta = 2°$ for the $LaF_3$/GaAs(111)A samples with film thickness $t = 48$ nm. The solid and dashed lines for each sample are the calculated diffuse intensity using the expression for diffuse intensities for two interfaces given by Sinha *et al.* in Ref. [50] with two different roughness exponents $\alpha = 0.36$ and $\alpha = 0.6$ respectively. The coefficients used are $\sigma_0 = 0.9$ nm (film/air), $\sigma_1 = 1.5$ nm (film/substrate) for the rms interface roughness and $\xi = 700$ nm for the correlation length with the roughness exponents indicated.

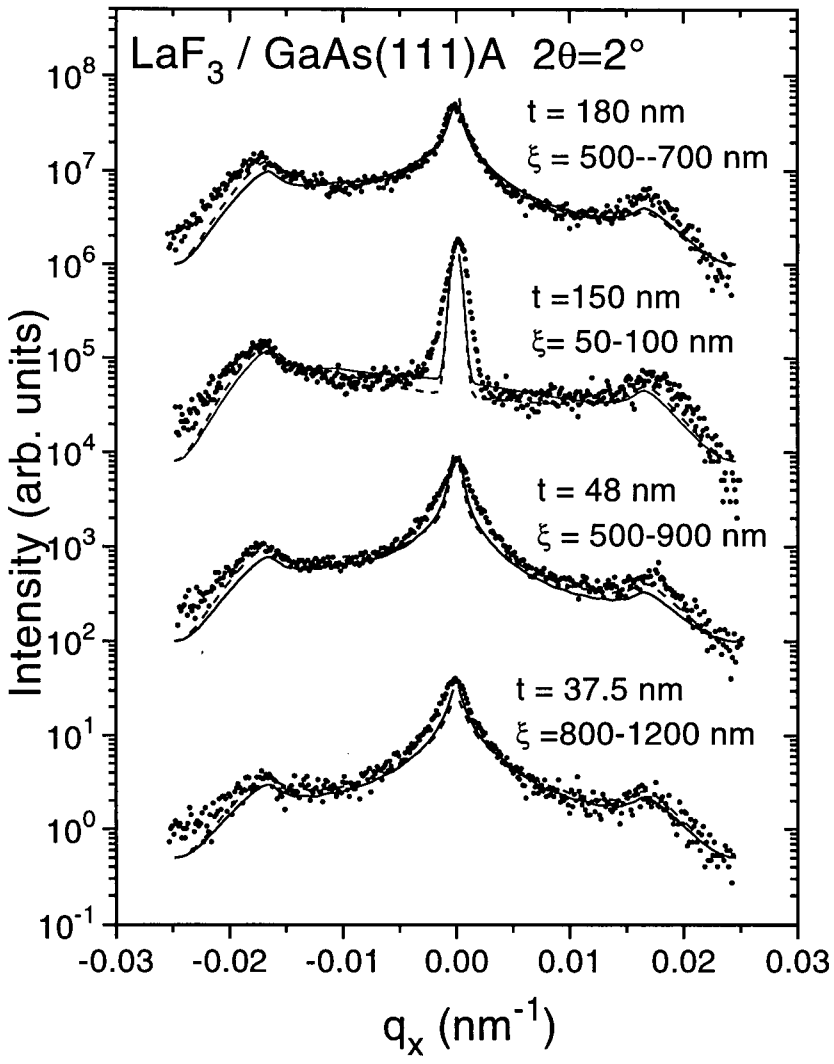


Figure 5.54: Transverse X-ray diffuse scans with $2\theta = 2°$ for the $LaF_3$/GaAs(111)A samples. The thickness $t$ and the range of correlation lengths $\xi$ obtained from the fit of diffuse intensities are indicated in the figure. The solid and dashed lines for each sample are the calculated diffuse intensity using the expression for diffuse intensities for two interfaces given by Sinha *et al.* in Ref. [50] with two different correlation lengths $\xi$. The roughness exponents $\alpha$ used in the calculation are $\alpha = 0.36$ except for the $t = 150$ nm sample whose exponent was $\alpha = 0.6$. The results of the fit are listed in Table 5.7. The coefficients used are $\sigma_0 = 0.9$ nm (film/air), $\sigma_1 = 1.5$ nm (film/substrate) for the rms interface roughness and $\xi = 700$ nm for the correlation length with the roughness exponents indicated.

were performed using the roughness exponent $\alpha$ obtained from the longitudinal diffuse scans performed at $\Delta\theta = 0.09°$ and $0.18°$. An example of the fit for a $LaF_3$/GaAs(111)A sample using roughness exponents obtained at two off-set angles are shown in Fig. 5.53. For the sample shown in Fig. 5.53, a better fit was obtained using the roughness exponent at $\Delta\theta = 0.09°$, $\alpha = 0.36$ than using the $\alpha$ at $\Delta\theta = 0.18°$, $\alpha = 0.6$. For some samples, we obtained better fits using the values of $\alpha$ determined at the off-set angle $\Delta\theta = 0.18°$. The estimated correlation lengths $\xi$, the roughness exponents $\alpha$ are listed in Table 5.7. The rms interface roughness $\sigma$ used in the fits are also listed. For all calculations, the rms interface roughnesses obtained from the specular reflectivity fits were used.

The importance of the diffuse intensities from the buried film/substrate interface can be seen from the diffuse intensities calculated using only the film/air interface shown in Fig. 5.52. In the calculation, the correlation length $\xi$ was assumed to be the same for the air/film and the film/substrate interfaces. The two interfaces are also assumed to be correlated i.e. the interference occurs between the diffuse beams from the two interfaces. The validity of this assumption can be seen from the diffuse intensities calculated for two uncorrelated interfaces shown in Fig. 5.52.

The correlation lengths for the two $LaF_3$/InP(111)B samples determined from the fit of the transverse diffuse scan were 30–60 nm and 70–120 nm. The estimated correlation length $\xi$ for the $LaF_3$/GaAs(111)A samples were longer ranging between 500 and 1200 nm except for the sample with $LaF_3$ film thickness, $t = 150$ nm, whose estimated correlation length was 50 – 100 nm. The difference between the longer correlation lengths for the $LaF_3$/GaAs samples and the correlation lengths of the $LaF_3$/InP samples and of the $t = 150$ nm $LaF_3$/GaAs sample is almost an order of magnitude. The $\alpha$ associated with longer correlation lengths were 0.36–0.38 whereas the $\alpha$ associated with shorter correlation lengths were 0.5–0.6.

The transverse scan was also performed on the atomic hydrogen etched bare GaAs(111)A

substrate. The correlation length $\xi$ determined from the fit of the transverse diffuse intensity was 300–500 nm using the value of roughness exponent $\alpha = 0.34$ obtained from the longitudinal diffuse scan. This result suggests that the longer correlation length for the $LaF_3$ film surface is associated with the surface structure of the GaAs substrates propagated through the $LaF_3$ film. The shorter correlation lengths for the $LaF_3$/InP samples and the 150 nm $LaF_3$/GaAs sample are likely associated with the surface structure of the film which is related to the characteristics of the films such as defects and the strain in the film. The comparison of the correlation lengths of the $LaF_3$/GaAs(111) samples and the GaAs substrate indicate that the correlation lengths determined in the present analysis represent the correlation lengths of the surface features which are dominant or which have greater rms roughness. We did not detect any trends in the correlation length as a function of film thickness.

## 5.4 Atomic Force Microscopy

Atomic force microscopy was performed to further investigate the surface morphology of the $LaF_3$ films on III-V semiconductors. The scaling exponents for the surface morphology of the $LaF_3$ films are obtained from AFM images and are compared with the X-ray scattering results.

### 5.4.1 Method

The correlation length $\xi$ and the roughness exponent $\alpha$ were obtained from the height-height correlation function $C(x, y)$ calculated from the AFM images using Eqn. 5.14, $C(r) = \sigma^2 e^{-(r/\xi)^{2\alpha}}$. The two dimensional height-height correlation function $C(x, y)$ is related to the height-height correlation in reciprocal space or power spectral density

Table 5.7: Correlation length $\xi$ obtained from the transverse diffuse scans for $LaF_3$/GaAs(111)A and $LaF_3$/InP(111)B samples. The values of rms interface roughness and roughness exponent $\alpha$ obtained from the specular and the longitudinal diffuse scans, used in the calculation are also listed. The correlation length $\xi$ was assumed to be the same for the air/film and the film/substrate interfaces and the two interfaces are assumed to be correlated.

| film thickness (nm) | rms roughness air/film $\sigma_0$ (nm) | rms roughness film/substrate $\sigma_1$ (nm) | $\alpha$ | $\xi$ (nm) |
|---|---|---|---|---|
| $LaF_3$/GaAs(111)A | | | | |
| 37.5 | 0.8 | 1.2 | $0.36 \pm 0.05$ | 800–1200 |
| 48 | 0.9 | 1.5 | $0.38 \pm 0.05$ | 500–900 |
| 150 | 0.5 | 1.5 | $0.6 \pm 0.1$ | 50–100 |
| 180 | 1.1 | 1.2 | $0.36 \pm 0.06$ | 700–1000 |
| $LaF_3$/InP(111)B | | | | |
| 111 | 0.5 | 0.6 | $0.53 \pm 0.05$ | 30–60 |
| 209 | 0.65 | 1.5 | $0.6 \pm 0.1$ | 70–120 |

$S(q_x, q_y)$ through:

$$C(x,y) \iff S(q_x, q_y) \tag{5.18}$$

$$C(x,y) = \frac{1}{2\pi}\int\int_{-\infty}^{\infty} S(q_x, q_y) e^{-i(q_x x + q_y y)} dq_x dq_y \tag{5.19}$$

The power spectral density $S(q_x, q_y)$ is given by:

$$S(q_x, q_y) = H(q_x, q_y)H(-q_x, -q_y) \tag{5.20}$$

$$= |H(q_x, q_y)|^2$$

$$= |\int\int_{-L/2}^{L/2} h(x,y) e^{i(q_x x + q_y y)} dxdy|^2 \tag{5.21}$$

where $H(q_x, q_y)$ is the Fourier Transform of the surface height $h(x,y)$ and $L$ is the width of the AFM image. In the last step, the property of the Fourier transform, $H(-q_x, -q_y) = H^*(q_x, q_y)$ for real $h(x,y)$ was used.

We have used a two-dimensional FFT routine in Ref. [78] to perform the Fourier transforms of the AFM images. First the two dimensional arrays of surface height $h_{n_x,n_y}$ from the AFM image was Fourier transformed to yield $H_{m_x,m_y}$ where $n_{x,y}$ and $m_{x,y}$ are the indices for the arrays. In the program, the frequency $f = q/2\pi$ rather than the wavevector $q$ was used for simplicity in programming. The height in reciprocal space at $\mathbf{f}$, $H(f_x, f_y)$ is approximated through:

$$H(f_x, f_y) \simeq \Delta_x \Delta_y H_{n_x,n_y} \tag{5.22}$$

$$= \Delta^2 H_{n_x,n_y} \tag{5.23}$$

where $\Delta_{x,y} = \Delta$ is the pixel size or the width of each pixel in the image. Then, the power spectral density is given by:

$$S(f_x, f_y) = \frac{1}{A}|H(f_x, f_y)|^2 \tag{5.24}$$

$$\simeq \frac{1}{(N\Delta)^2}|\Delta^2 H_{n_x,n_y}|^2 \tag{5.25}$$

$$= \frac{\Delta^2}{N^2}|H_{n_x,n_y}|^2 \tag{5.26}$$

where $A = (N\Delta)^2$ is the area of the AFM image and $N$ is the number of pixels in one of the directions (N=512 in our case). Finally, the correlation function $C(x, y)$ was obtained through:

$$\begin{aligned} C(x,y) &\simeq \Delta_{fx}\Delta_{fy}[S(f_x, f_y)]_{FFT} && (5.27)\\ &= \frac{1}{(N\Delta)^2}[\frac{\Delta^2}{N^2}|H_{n_x,n_y}|^2]_{FFT} && (5.28)\\ &= [\frac{1}{N^4}|H_{n_x,n_y}|^2]_{FFT} && (5.29) \end{aligned}$$

where $\Delta_{fx,fy} = \frac{1}{N\Delta}$ is the spacings in reciprocal space between $H_{n_x,n_y}$ and $[\,]_{FFT}$ indicates the FFT of the expression in the bracket.

The mean square fluctuation in surface height $g(r)$ is given by [49]:

$$\begin{aligned} g(r) &= \langle[z(x', y') - z(x, y)]^2\rangle \\ &= 2\sigma^2 - 2C(r) && (5.30)\\ &= 2\sigma^2[1 - e^{-(\frac{r}{\xi})^{2\alpha}}] && (5.31) \end{aligned}$$

where $r = \sqrt{x^2 + y^2}$. The radial average of $C(x, y)$, $C(r)$ was taken to obtain $g(r)$ using Eqn. 5.31. The radial average is performed by integrating the two dimensional $C(x, y)$ over an annulus of radius $r$.

In this study, the height-height correlation in reciprocal space or the power spectral density (PSD), $S(q)$, the correlation function $C(r)$ and the mean square fluctuation $g(r)$ are obtained from the AFM images. The roughness exponent $\alpha$ is first determined from $g(r)$ using Eqn. 5.31 for small $r$:

$$g(r) \simeq 2\sigma^2(\frac{r}{\xi})^{2\alpha} \quad (5.32)$$

Next, the correlation length $\xi$ is determined from the height-height correlation $C(r)$ using $C(r) = \sigma^2 e^{-(r/\xi)^{2\alpha}}$ in Eqn 5.14.

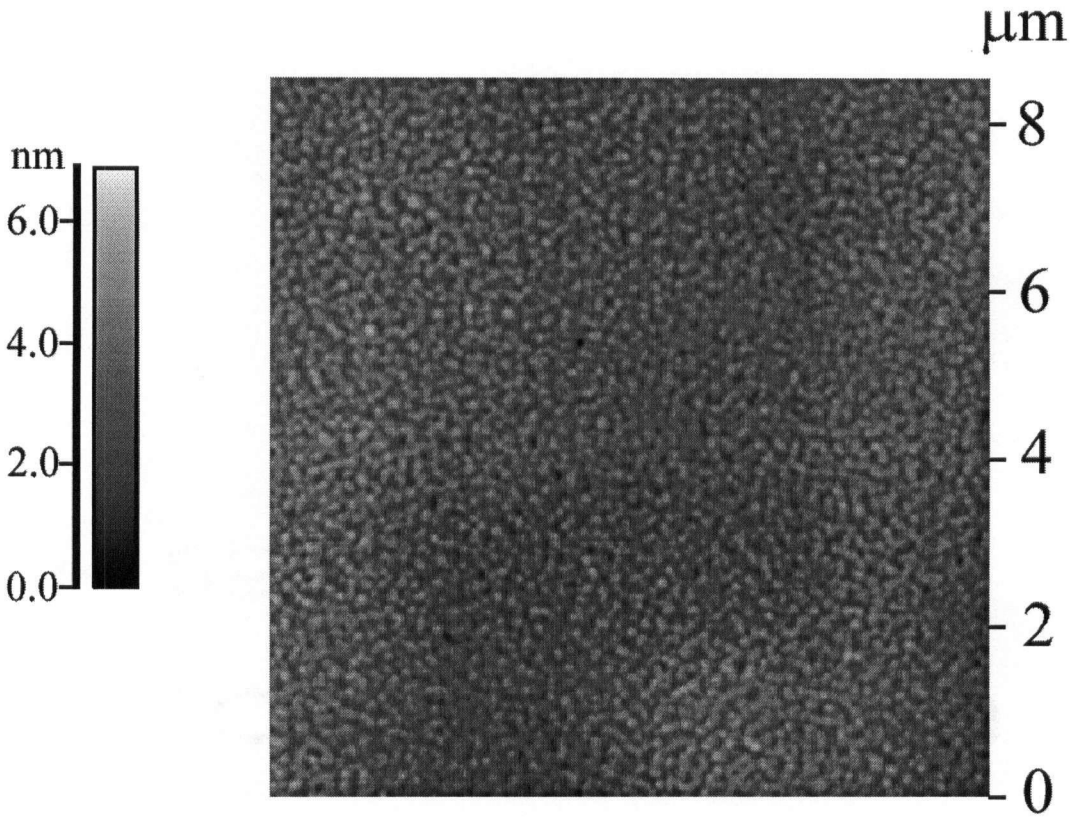


Figure 5.55: AFM images of a $LaF_3$/GaAs(111)A sample with film thickness t = 150 nm.

### 5.4.2 Results

AFM images of $LaF_3$/GaAs(111)A and $LaF_3$/InP(111)B samples are shown in Fig. 5.55 and 5.56 .

The radial averages of power spectral density, $S(q)$ where $q = \sqrt{q_x^2 + q_y^2}$ for the $LaF_3$/GaAs(111)A and $LaF_3$/InP(111)B samples are shown in Fig. 5.57. We observe a shoulder near $L_0 = 0.03$ nm$^{-1}$ in $S(q)$ for the $LaF_3$/GaAs(111)A sample and a shoulder near $L_0 = 0.02$ nm$^{-1}$ in $S(q)$ for the $LaF_3$/InP(111)B sample. Each characteristic

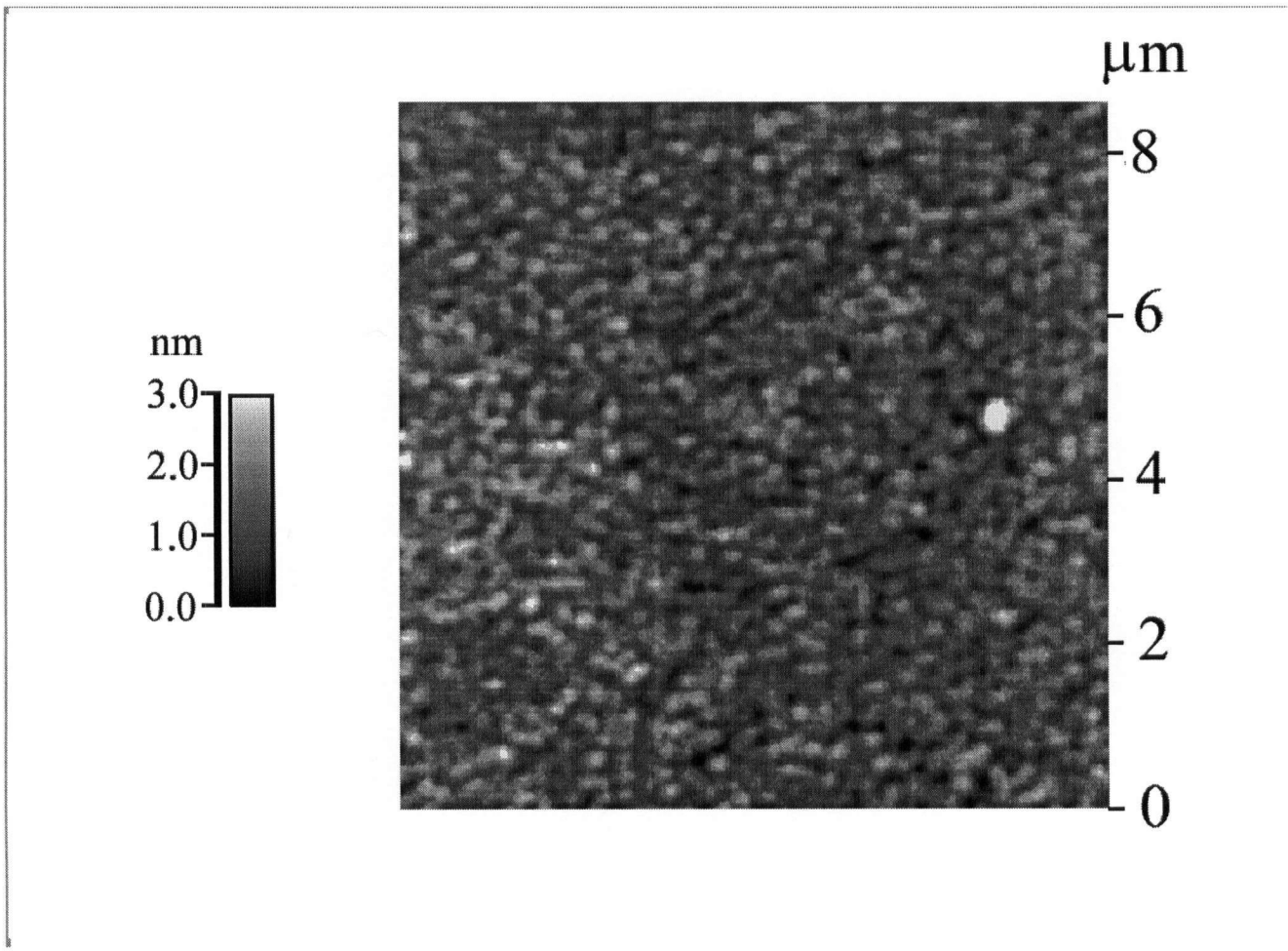


Figure 5.56: AFM images of a $LaF_3$/InP(111)B sample with film thickness 209 nm.

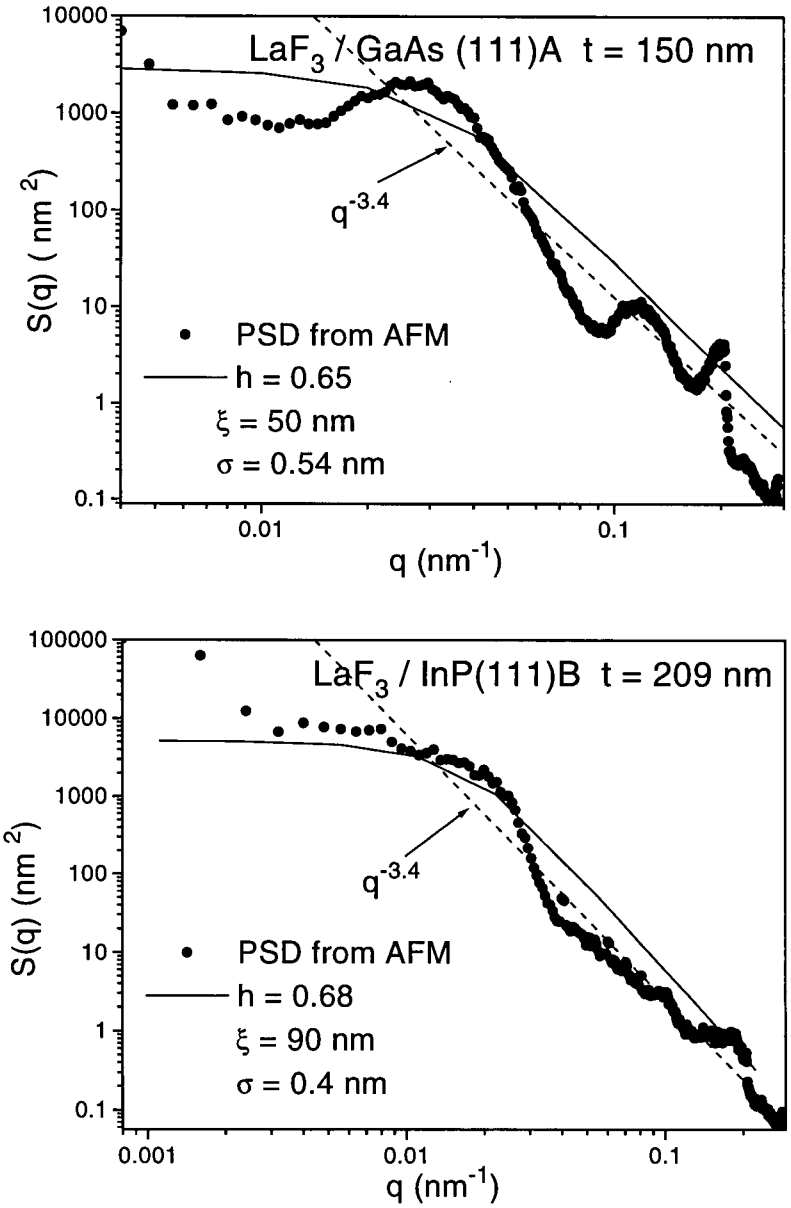


Figure 5.57: Height-height correlation in reciprocal space S(q) obtained from the AFM images of (top) the $LaF_3$/GaAs(111)A sample with film thickness t = 150 nm and (bottom) the $LaF_3$/InP(111)B sample with film thickness t = 209 nm. The dashed lines are the function $S(q) \sim q^{-z}$ with $z = 3$. The solid lines are the height-height correlation $S(q)$ obtained by Fourier transforming the the height-height correlation $C(r)$ using $C(r) = \sigma^2 e^{-(r/\xi)^{2\alpha}}$ in Eqn 5.14.

Table 5.8: Characteristic $q$ values and corresponding characteristic lengths $L_0$ observed in the height-height correlation $S(q)$ for $LaF_3$/GaAs(111)A and $LaF_3$/InP(111)B. The peak to peak distances $D$ of the circular features observed in the AFM images are also listed.

| | $q_0$ ($nm^{-1}$) | $L_0 = 2\pi/q_0$ (nm) | D (nm) |
|---|---|---|---|
| $LaF_3$/GaAs(111)A | 0.03 | 210 | 100–200 |
| $LaF_3$/InP(111)B | 0.018 | 350 | 250–450 |

wavevector $q_0$ corresponds to a length in real space $L_0 = 2\pi/q_0$. The characteristic $q_0$ and the corresponding lengths $L$ for the $LaF_3$/GaAs(111)A and $LaF_3$/InP(111)B samples are listed in Table 5.8. The characteristic length for the $LaF_3$/InP(111)B sample, $L_0 = 350$ nm is longer than the length for the $LaF_3$/GaAs(111)A sample, $L_0 = 210$ nm. We also list the peak to peak distances $D$ of the circular features observed in the AFM images in Fig. 5.55 and 5.55 in Table 5.8 for comparison. The characteristic lengths $L_0$ are comparable to the peak to peak distances $D$.

In the PSDs of both $LaF_3$/InP and $LaF_3$/GaAs samples in Fig. 5.57, small features are observed in the region above $q \simeq 0.1$ $nm^{-1}$. If we assume that a surface structure needs at least three pixels corresponding to $q = 2\pi/45 = 0.14$ $nm^{-1}$, to be identified, any features in the region above $q \simeq 0.1$ $nm^{-1}$ do not reflect the surface structures of the samples. Hence we interpret that the features in the PSDs in the regions above $q \simeq 0.1$ $nm^{-1}$ are due to noises at the resolution limit of the AFM and not due to the surface structures of the samples.

The mean square fluctuation $g(r)$ and height-height correlation $C(r)$ obtained from the AFM images for the $LaF_3$/GaAs(111)A and $LaF_3$/InP(111)B samples are shown in

Table 5.9: Rms surface width $\sigma$, the roughness exponent $\alpha$ and the correlation length $\xi$ for the $LaF_3$/GaAs(111)A, $LaF_3$/InP(111)B samples and for the atomic-H etched GaAs(111)A substrate obtained from the AFM images. The film thicknesses $t$ are also listed. The X-ray results for the same samples are listed for comparison.

| | $t$ (nm) | | $\sigma$ (nm) | $\alpha$ | $\xi$ (nm) |
|---|---|---|---|---|---|
| $LaF_3$/GaAs(111)A | 150 | AFM | $0.58 \pm 0.05$ | $0.65 \pm 0.05$ | $50 \pm 9$ |
| | | X-ray | $0.5 \pm 0.1$ | $0.58 \pm 0.05$ | 50 – 100 |
| $LaF_3$/InP(111)B | 209 | AFM | $0.4 \pm 0.1$ | $0.68 \pm 0.06$ | $90 \pm 10$ |
| | | X-ray | $0.4 \pm 0.1$ | $0.6 \pm 0.1$ | 70 – 120 |
| GaAs(111)A | – | AFM | $1.0 \pm 0.1$ | $0.37 \pm 0.05$ | – |
| | | X-ray | $0.9 \pm 0.1$ | – | 300 – 500 |

Fig. 5.58. The solid lines in the plot of $g(r)$ are the linear regressions to determine the roughness exponents $\alpha$ using Eqn. 5.31. The solid lines in $C(r)$ are the fits of height-height correlation in Eqn. 5.14 to determine the correlation length $\xi$. The value of the roughness exponent $\alpha$ was fixed to the values determined by linear regression of $g(r)$ during the fits. The AFM microscopy was also performed on the atomic hydrogen etched bare GaAs(111)A substrate and is shown in Fig. 5.59. The mean square fluctuation $g(r)$ and the height-height correlation $C(r)$ obtained from the AFM images are also shown in Fig. 5.59.

The values of $\alpha$, $\sigma$ and $\xi$ determined from the AFM images are listed in Table 5.9. The results from the X-ray scattering are also listed for comparison. The values of rms surface roughness $\sigma$ and the correlation length $\xi$ measured by AFM and X-ray scattering

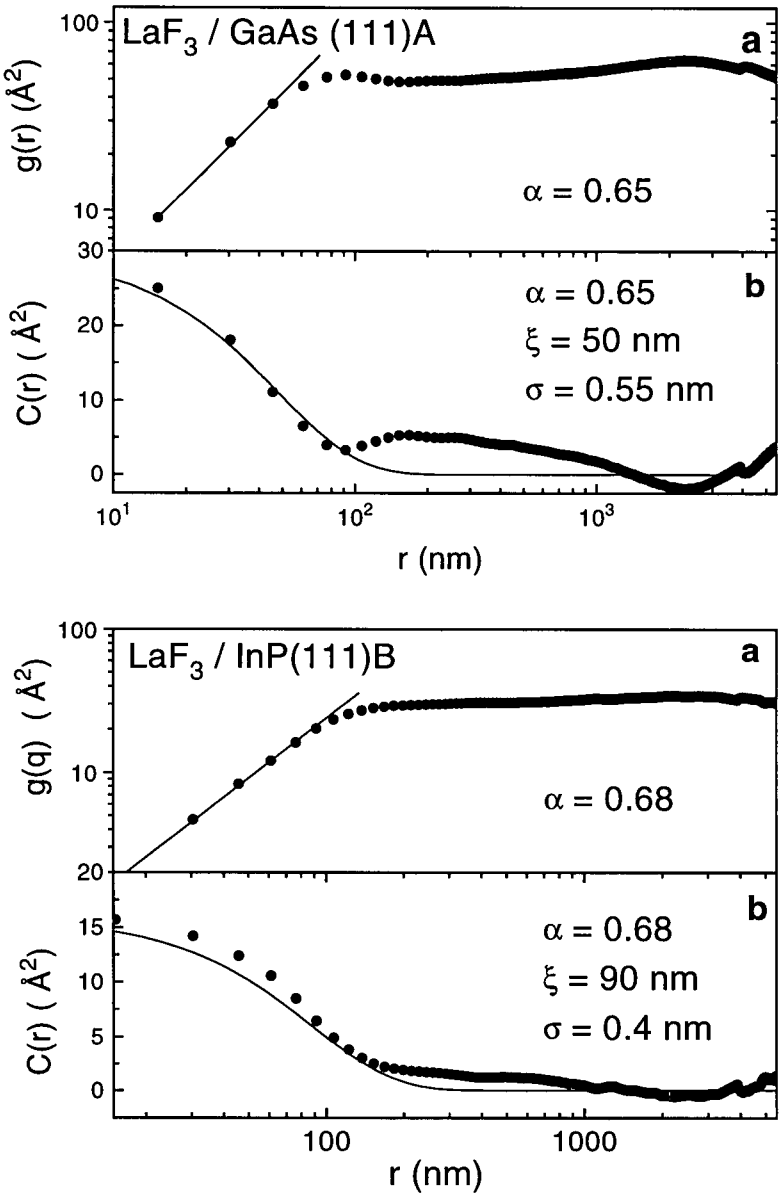


Figure 5.58: (a) Mean square fluctuation $g(r)$ and (b) height-height correlation function $C(r)$ computed from the AFM image of the $LaF_3$/GaAs(111)A (top) and $LaF_3$/InP(111)B (bottom) samples. The solid lines in (a) are the linear regression to obtain the roughness exponent $\alpha$. The solid lines in (b) are the calculated correlation function $C(r) = \sigma^2 e^{-(\frac{r}{\xi})^{2\alpha}}$ using the values of parameters indicated.

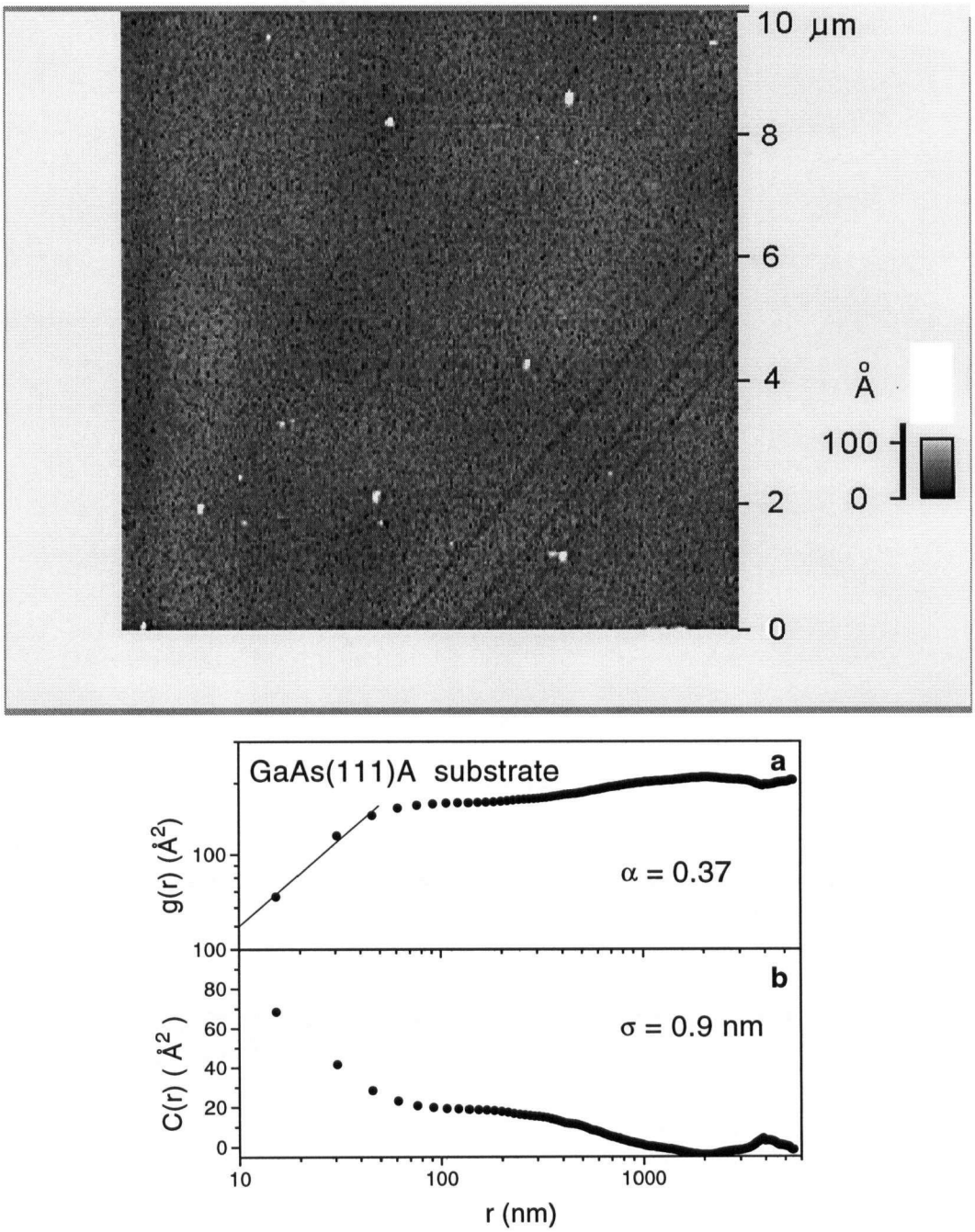


Figure 5.59: AFM image of the atomic hydrogen etched GaAs(111)A substrate (top). The lower figure shows (a) the mean square fluctuation $g(r)$ and (b) the height-height correlation $C(r)$ computed from the AFM image. The lines in the AFM image are polishing marks from the manufacturer. The solid line in (a) is the linear regression to obtain the roughness exponent $\alpha$.

are equal within the uncertainties of the measurements. The correlation length for the $LaF_3$/InP(111)B sample is longer than that for the $LaF_3$/GaAs(111)B sample by about a factor of two. The roughness exponents $\alpha$ measured by AFM agree with the values of $\alpha$ measured by X-ray scattering.

Close inspection of the height-height correlation $C(r)$ in Fig. 5.58 shows some features near $r = 1000$ nm in both samples. This implies that there are more than one characteristic length scale in the surface topography of the film. The AFM results support our interpretation of the presence of the two ranges of correlation lengths obtained in the analysis of the X-ray transverse diffuse scans for the $LaF_3$/GaAs(111)A system. The two ranges of correlation lengths $\xi$ correspond to the two surface features present on each $LaF_3$ film. The value of correlation length obtained by X-ray scattering is that of the surface feature which is dominant or in other words, the feature which has a larger surface roughness amplitude than others.

## 5.5 Discussion

### 5.5.1 Relationship between the bulk film structure and the surface morphology

In this section we investigate the relationship between the crystal structures inside the film and the surface morphology of the films in the $LaF_3$/semiconductor system. We compare in Table 5.10, the bulk lateral coherence lengths $L_x$ determined by X-ray rocking curve measurements in Chapter 4 with the surface correlation lengths $\xi$ determined from the AFM images. For the $LaF_3$/GaAs(111)B sample, the coherence length ($L_x = 47$ nm) in the film obtained by XRD is equal to the correlation length ($\xi = 50$ nm) measured by AFM within the experimental accuracy. For the $LaF_3$/InP(111)B sample, the shorter bulk coherence length of the two lengths determined by rocking curve measurements

Table 5.10: Comparison of the bulk lateral coherence length $L_x$ measured by X-ray rocking curve, the surface correlation length $\xi$ and the characteristic length $L$ determined from the AFM images for the $LaF_3$/GaAs(111)A and $LaF_3$/InP(111)B samples.

| | Bulk Coherence Length $L_x$ (nm) Rocking Curve | Surface Correlation Length $\xi$ (nm) AFM |
|---|---|---|
| $LaF_3$/GaAs(111)A | 47 | $50 \pm 9$ |
| $LaF_3$/InP(111)B | 100 | $90 \pm 10$ |

($L_x = 100$ nm) is equal within the uncertainty of the measurements to the surface correlation length ($\xi = 90 \pm 10$ nm).

The comparison is consistent with the columnar structures in the $LaF_3$ films on GaAs observed by scanning electron microscopy in Fig. 4.40. We interpreted in Chapter 4 that the bulk coherent lengths from X-ray rocking curves represent the spacings between the columnar regions of defects. The comparison between the bulk coherence lengths and the surface correlation length confirms that the bulk coherence lengths represent the columnar defect spacings. The comparison also shows that the columnar structure propagates through the $LaF_3$ films and is revealed on the film surface. In other words, the surface structures of the $LaF_3$ on GaAs and InP reflect the coherent domains underneath them. In Chapter 4, we also argued that the columnar defects are formed to accommodate the lattice mismatch between the fluoride and the semiconductor at the growth temperature. The observed relationship between the surface and the bulk coherence lengths suggests that the surface structures of the films are associated with the strain relieving defects formed during film growth. The lattice mismatch in the $LaF_3$/InP system (0.41%) is

smaller than that in the $LaF_3$/GaAs system (4.5 %). Therefore the surface coherence lengths are longer for $LaF_3$ films on InP than films on GaAs, since the defect spacings are longer in the $LaF_3$ films on InP. The study of the surface morphology of $LaF_3$ films on semiconductors as well as the bulk crystallinity of the fluoride films showed that the strain relieving defects are vertical regions around the periphery of coherent columns.

### 5.5.2 Continuum equation describing film growth

The values of exponents obtained for the $LaF_3$/GaAs(111)A and $LaF_3$/InP(111)B samples obtained by X-ray scattering and the exponents predicted by continuum models are summarized in Table 5.11. The similarity between the values of growth exponents and the roughness exponents for the two systems suggest that their growth processes are similar despite the difference in the growth temperature and lattice mismatch. The growth exponent and the roughness exponent measured X-ray scattering are closest to the value ($\beta = 0.20$, $\alpha = 0.67$) predicted by the VLD model [53, 54]. In the following discussion of continuum models, the surface height $h$ is assumed to be in the moving frame of reference i.e. $h = h' - Ft$ where $h'$ is the surface height in the inertia frame, $F$ is the deposition flux and $t$ is the time.

The Edward-Wilkinson (EW) model is described by the equation of the form [56]:

$$\frac{\partial h(\mathbf{x},t)}{\partial t} = \nu\nabla^2 h + \eta(\mathbf{x},t) \tag{5.33}$$

It has shown by Herring [57] that the term $\nu\nabla^2 h$ describes the mass transport through evaporation-recondensation. We expect that the desorption (evaporation) to be negligible in the MBE growth. The presence of a Schwoebel barrier [58] also lead to a $\nu\nabla^2 h$ term. A Schowebel barrier is a potential barrier at the edge of an island or a step which prevents the particles approaching to an edge of the island to jump off the edge. The term $\eta(\mathbf{x},t)$ describes the noise due to the fluctuations in the deposition of atoms.

Table 5.11: Comparison of the scaling exponents obtained by X-ray scattering and the growth model.

| | Growth Exponent $\beta$ | Roughness Exponent $\alpha$ |
|---|---|---|
| $LaF_3$/GaAs(111)A | $0.2 \pm 0.2$ | $0.6 \pm 0.1$ |
| $LaF_3$/InP(111)B | $0.0 \pm 0.1$ | $0.6 \pm 0.1$ |
| Wolf and Villain [55] (WV) | 0.25 | 1 |
| Villain [53], Lai and Das Sarma [54] (VLD) | 0.20 | 0.67 |
| Kardar and Parizi and Zhang [52] (KPZ) | 0.24 | 0.38 |
| Edward and Wilkinson [56] (EW) | 0 | 0 |

In the KPZ model, a nonlinear term $\frac{\lambda}{2}(\nabla h)^2$ is added to the EW equation [52]:

$$\frac{\partial h(\mathbf{x},t)}{\partial t} = \nu\nabla^2 h + \frac{\lambda}{2}(\nabla h)^2 + \eta(\mathbf{x},t) \tag{5.34}$$

The KPZ equation is non-conservative and describes the lateral growth in the direction parallel to the interface. The lateral growth is present in the case where the deposited particles arrive isotropically. In the case of the MBE growth, the particles arrive as a beam of molecules. Hence we do not expect the process described by the KPZ model to play an important role.

In the Wolf and Villain (WV) model [55], the evolution of the surface height $h(\mathbf{x})$ is described by the linear diffusion equation [55]:

$$\frac{\partial h(\mathbf{x},t)}{\partial t} = -\nu_1\nabla^4 h + \eta(\mathbf{x},t) \tag{5.35}$$

The WV equation is conservative i.e. it obeys the continuity equation:

$$\frac{\partial h(\mathbf{x},t)}{\partial t} + \nabla\cdot\mathbf{j}(\mathbf{x},t) = 0 \tag{5.36}$$

where $\mathbf{j}$ is the surface current driven by the difference in chemical potential $\mu$:

$$\mathbf{j} \propto -\nabla\mu(\mathbf{x},t) \tag{5.37}$$

In the WV equation, the chemical potential $\mu$ is proportional to the surface curvature $\nabla^2 h$ which increases with increasing number of neighbors or the chemical bonds that a particle may form at that site. Hence the $-\nu_1\nabla^4 h$ term describes the surface diffusion whose current is controlled by the local chemical potential or the chemical bonds between the particles and the surface. We expect the process described by the term $-\nu_1\nabla^4 h$ to be important in our MBE growth, since the chemical bonds between the particles on the surface and the surface of the film play an important role in the formation of the $LaF_3$ films. We also expect that the diffusion of the fluoride molecules to play an important

role in the surface relaxation at the growth temperature of the films for the reason below. The melting temperature of $LaF_3$ or the temperature required for the $LaF_3$ molecules to diffuse in the bulk $LaF_3$ is 1493°C. If we assume that the interaction energy between a $LaF_3$ molecule on the surface and the bulk $LaF_3$ is half of the energy for the molecules in the bulk $LaF_3$, we expect that the temperature required for the $LaF_3$ molecules to diffuse on the surface to be half of the melting point. The depositions of $LaF_3$ were performed at 600°C for GaAs and 400°C for InP, approximately half of the melting point of $LaF_3$. The surface diffusion process described by the term $-\nu_1\nabla^4 h$ is more important at a shorter length scale or a large $q$ value as compared to the evaporation-condensation process described by the $\nu\nabla^2 h$ term in the KPZ and the EW models.

In the VLD model, a nonlinear term is added to the WV equation which results in [53, 54]:

$$\frac{\partial h(\mathbf{x},t)}{\partial t} = -\nu_1\nabla^4 h + \lambda_1\nabla^2(\nabla h)^2 + \eta(\mathbf{x},t) \tag{5.38}$$

The renormalization group analysis of the equation [53, 54] results in the values of exponent $\beta = 0.20$ and $\alpha = 0.67$. The values are closest to the experimental values obtained for the $LaF_3$ growth on GaAs and InP ($\beta = 0.2 \pm 0.2$, $\alpha = 0.6 \pm 0.1$, see Table 5.11). A numerical simulation of the one-dimensional discrete model belonging to the same universality class (the same scaling exponents) as the VLD model was introduced by Lai and Das-Sarma [54]. The Lai and Das-Sarma model is a discrete *solid on solid* model in which a particle arriving on a surface is allowed to move to a nearest kink site (a site with two neighbours) with high binding energy to lower its energy or to increase its number of neighbors. The model also allows the process where a atom in a kink site can break its two bonds and jump either up or down to a nearest kink site having a lower energy. The process described by the discrete model is shown schematically in Fig. 5.60.

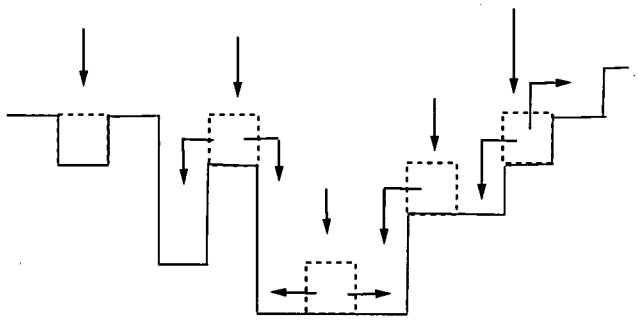

Figure 5.60: Schematic illustration of the surface relaxation mechanism described by the one dimensional discrete model by Lai and Das Sarma [54] which belong to the same universality class as the continuum model by Villain [53], Lai and Das Sarma [54] from Ref. [63].

In summary, the most appropriate theoretical model which describes the kinetic process of our $LaF_3$ growth is the VLD model. The evaporation-recondensation process described by the EW equation does not play a major role in the MBE growth. We expect the lateral growth process described by the KPZ model to be negligible in the MBE growth because of the directionality of arriving particles. In both the WV and VLD models, the surface diffusion controlled by the local chemical potential is the most important process in the surface relaxation. In our MBE growth condition, we expect the surface diffusion to play a major role in the surface relaxation. The scaling exponents for our $LaF_3$ growth were closer to those predicted by the VLD model than those predicted by the WV model. This is anticipated because the WV model is a special case of the more general VLD model.

Other experimental results which showed similar values of roughness exponents $\alpha$ to

our values of $\alpha$ ($\alpha = 0.6$) determined for $LaF_3$ on GaAs and InP include the deposition of Ag on Si ($\alpha = 0.70$) [59] using X-ray scattering and STM, the growth of Cu on Cu(100) studied by He atom beam scattering [60] ($\alpha = 0.6 - 1$) and Si on Si ($\alpha = 0.68$) studied by STM [61].

### 5.5.3 Dynamical scaling

The scaling relation of the surface morphology can also be observed from the power spectral density (PSD) $S(q)$. According to the *Family–Vicsek* dynamic scaling relationship, the PSD $S(q)$ scales as [64]:

$$S(q) = q^{-d-2\alpha} f(\frac{t}{q^{-z}}) \tag{5.39}$$

where $d$ is the dimension of the interface ($d = 2$ in our case), $z$ is the dynamical exponent, $t$ is the time and $f(t/q^{-z})$ is the scaling function. For the growth model by Villain [53], Lai and Das Sarma [54] (VLD), the dynamical exponent $z$ is related to the roughness exponent $\alpha$ through [54]: $z = 2\alpha + d$. Also the function $f(t/q^{-z}) \sim$ constant for $t/q^{-z} >> 1$ or for a large $q$. In this case, the PSD $S(q)$ obeys the power law of the form: $S(q) \propto q^{-z}$. For the VLD model the dynamical exponent is $z = \alpha/\beta = 0.67/0.20 \simeq 3.4$. We have plotted the power law $S(q) \propto q^{-z}$ with $z = 3.4$ in Fig. 5.57. The scaling relation $S(q) \propto q^{-z}$ is consistent for the regions above cut-offs ($q > q_0$) for both the $LaF_3$/GaAs(111)A and $LaF_3$/InP(111)B samples.

In order to estimate the cut-off wavevector $q$ in $S(q)$, the correlation function $C(r)$ described by Eqn 5.14 are Fourier transformed through:

$$S(q) = 2\pi \int_0^\infty C(r) J_0(qr) r dr \tag{5.40}$$

$$= 2\pi \int_0^\infty \sigma^2 e^{-(\frac{r}{\xi})^{2\alpha}} J_0(qr) r dr \tag{5.41}$$

where $J_0$ is the Bessel function of the zeroth order, $\sigma$ is the rms interface width, $\xi$ is the correlation length and $\alpha$ is the roughness exponent. The values of $S(q)$ for the

$LaF_3$/GaAs(111)A and $LaF_3$/InP(111)B samples studied by AFM are evaluated numerically using the values of the roughness coefficient $\alpha$, the cut-off length $\xi$ and the rms surface roughness $\sigma$ obtained from the AFM images. Calculated height-height correlation $S(q)$ using the values of $\sigma$, $\xi$ and $\alpha$ determined from the fit of the correlation function $C(r)$ are shown in Fig. 5.57.

The cut-off wavevector $q_0$ for $S(q)$ were $q_0 \simeq 0.04$ nm$^{-1}$ for the $LaF_3$/GaAs(111)B sample and $q_0 \simeq 0.02$ nm$^{-1}$ for the $LaF_3$/InP(111)B sample. Below the cut-off wavevector $q_0$, the height-height correlation $S(q)$ is nearly constant. Above the cut-off wavevector, the variation of the calculated $S(q)$ agrees with that of the PSD $S(q)$ obtained from the AFM images and also the dynamic scaling relationship $S(q) \propto q^{-z}$ where $z = 3.4$.

## 5.6 Summary

The surface morphology of $LaF_3$ films grown on III-V semiconductors were investigated by X-ray scattering and AFM. The surface correlation lengths of the $LaF_3$ films obtained by X-ray scattering and the bulk coherence lengths from X-ray rocking curve measurements were comparable to each other. The result is consistent with columnar defect structures of $LaF_3$ films observed in Chapter 4. We interpreted that the defects are formed to accommodate the lattice mismatch at the growth temperature. That is the lateral sizes of coherent regions in $LaF_3$ films are associated with the lattice mismatch of the system at the growth temperature. The comparison of the surface correlation lengths and the bulk coherence lengths for the $LaF_3$/GaAs, InP system suggest that the surface structures of $LaF_3$ films on semiconductors reflect the columnar structures underneath them. The surface coherence length for $LaF_3$ films on InP was longer than on GaAs since the lattice mismatch is smaller in the $LaF_3$/InP system at the growth temperature. The surface structures of the $LaF_3$ films are also associated with the strain relieving defects formed

to accomodate the lattice mismatch at the growth temperature. The surface coherence lengths from X-ray scattering and AFM, the bulk coherence lengths from X-ray rocking curves as well as cross sectional SEM showed that the strain relieving defects are vertical regions separating the columns of coherent crystals and the surface structures reflect the columnar structures underneath them.

The surface morphology of the $LaF_3$ films on GaAs and InP was analysed using the self-affine surface model. The scaling exponents determined were closest to those predicted by the Villain-Lai-Das Sarma model [53, 54].

# Chapter 6

## Semiconductor/Fluoride/Semiconductor Growth

Growth of semiconductor-fluoride multilayer structures has been investigated by a number of researchers due to their applications in optical and electronic devices. Most of the research has been concentrated on semiconductor growth on difluorides such as $CaF_2$ and $SrF_2$. Representative work on III-V semiconductor growth on difluoride/semiconductor structures include InP/(Ca, Sr)$F_2$/InP(100) [67], GaAs/(Ca, Sr)$F_2$/GaAs(100) [68], GaAs /(Ca, Sr)$F_2$/Si(100) [69] and GaAs/$CaF_2$/Si(111) [70]. In this chapter, the growth of InP and GaAs on the rare-earth trifluoride/III-V semiconductor structures: $LaF_3$/InP(111)B, $LaF_3$/GaAs(111) and $ErF_3$/GaAs(111), are studied.

Previous studies of semiconductor/difluoride/semiconductor structures have shown that the semiconductors [41] have a tendency to form islands due to the lower surface energy of the difluoride ($CaF_2$ and $BaF_2$) which varies from 0.3 to 0.5 J/m$^2$ [32, 33] depending also on the orientation of the material as compared to the surface energy of semiconductors (Si and GaAs) which ranges from 0.8 to 3.2 J/m$^2$ [34].

As we discussed in Chapter 3, the condition for wetting for systems of a film on a substrate is [31]:

$$\gamma_s > \gamma_f + \gamma_{sf} \tag{6.42}$$

where $\gamma_s$, $\gamma_f$ and $\gamma_{sf}$ are the free energy for substrate/air, film/air and film/substrate interfaces respectively. In fluoride/semiconductor systems, we expect that the film/substrate interface free energy $\gamma_{sf}$ to be lower than either $\gamma_s$ or $\gamma_f$. Since the surface free energy of fluorides is generally lower than that of semiconductors or $\gamma_{semiconductors} > \gamma_{fluoride}$,

neglecting the film/substrate interface energy, the condition for the wetting is satisfied for fluoride films on semiconductors. In Chapter 3, we showed by angle dependent photoemission spectroscopy that the fluoride films cover semiconductor substrates as we expected. For a semiconductor on fluoride system, we expect the semiconductors to form islands when deposited on fluorides, since the condition for wetting is not satisfied.

The fluoride layers were grown by molecular beam epitaxy on GaAs(111)A and InP(111)B substrates as described in Chapter 2. After the fluoride film growth, the samples were transferred, without being exposed to air, to an adjacent chamber for the GaAs or InP growth. Typical substrate temperature was 500°C during the InP growth and 600°C during the GaAs growth as measured by the diffuse reflectance spectroscopy [71]. The V/III flux ratio was $As_2/Ga\sim$ 4 for the GaAs growth and $P_2/In\sim$ 12 for the InP growth. The X-ray diffraction experiments were done ex-situ using a Cu K$\alpha$1 ($\lambda$ = 1.5405 Å) rotating anode X-ray source and a high resolution four crystal (double-axis) diffractometer (BEDE 200).

## 6.1 Results

### 6.1.1 Formation of InP and GaAs islands on the fluoride/semiconductor structures

The growth of InP and GaAs were performed on the $LaF_3$, $ErF_3$/III-V semiconductor structures. An AFM image of the surface of a InP/$LaF_3$/InP(111)B sample is shown in Fig.6.61. Islands with a lateral size of 300 – 500 nm are observed in the image. The density of the islands is estimated to be $1 \times 10^9$ cm$^{-2}$. Note that the most of the edges of the islands have angles of approximately 60 or 120°. The InP islands shape reflects the trigonal $a \times a$ face structure of the $LaF_3$ film consistent with the orientation of the $LaF_3$ film grown on GaAs(111) [5].

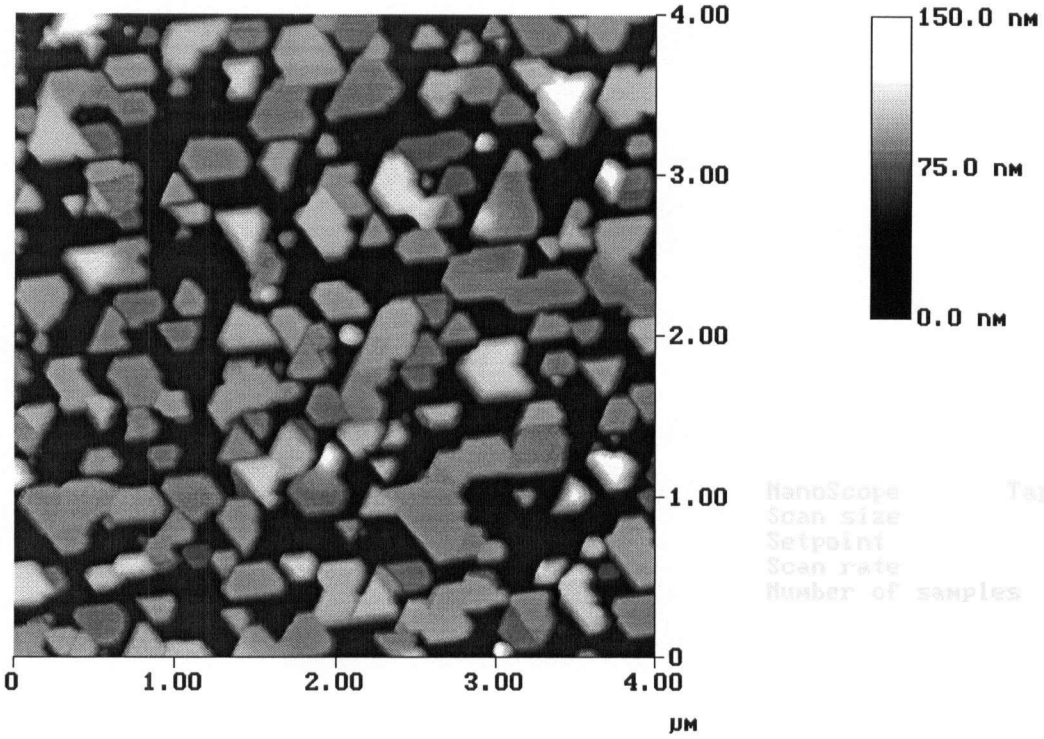


Figure 6.61: AFM image of the surface of InP/$LaF_3$/InP(111)B sample. InP islands whose edges have an angle of 60 or 120° are observed. The shape of the islands reflects the trigonal $a \times a$ face of the $LaF_3$ layer underneath the InP islands.

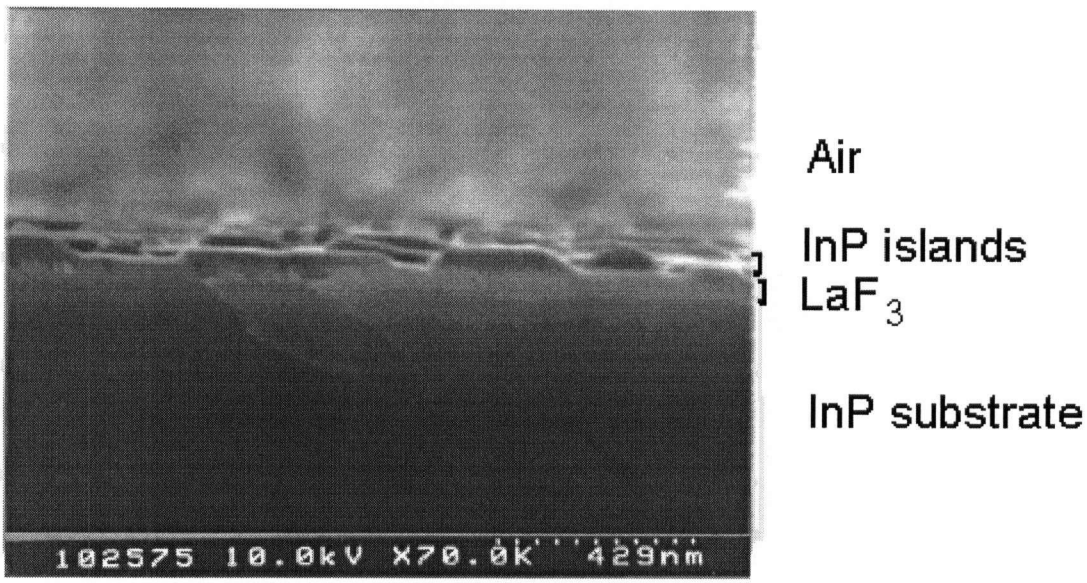


Figure 6.62: Cross-sectional SEM image of the InP/$LaF_3$/InP(111)B sample in Fig. 6.61. The InP islands are faceted suggesting that they are single crystals. The thickness of InP islands ranges between 30 and 40 nm.

In order to further investigate the surface morphology of the InP/$LaF_3$/InP(111)B sample, scanning electron microscopy was performed. A cross sectional SEM image of the InP/$LaF_3$/InP(111)B sample near the edge of the sample is also shown in Fig. 6.62. The $LaF_3$ layer is 35 nm thick as measured from the interference fringes of the (002) $LaF_3$ X-ray diffraction peak. The InP islands have a faceted shape which suggests that they are single crystal, with thickness between 30 and 40 nm. Since the growth of InP lasted for 6 min., the growth rate is 5 to 7 nm/min.

The formation of InP islands was also observed on the $LaF_3$/GaAs(111)A structure. The cross sectional SEM image of a $LaF_3$/ InP/ $LaF_3$/ GaAs(111)A sample is shown in Fig. 6.63. The InP islands are 200–300 nm wide and 200–300 nm in height. The growth time of InP was 7 min. yielding an island growth rate of 30–40 nm/min.

AFM images of a InP/$LaF_3$/GaAs(111)A sample at three different magnifications are shown in Fig. 6.64 to 6.66. InP islands 70–130 nm in diameter are observed in the AFM


Figure 6.63: Cross sectional SEM image of a $LaF_3$/InP/$LaF_3$/GaAs(111)A sample showing InP island size is 200–300 nm across and 200–300 nm high.

images. The density of the islands is approximately $4 \times 10^9$ cm$^{-2}$.

Growth of GaAs on a $ErF_3$/GaAs(111)A structure was also studied. An AFM image of the surface of the GaAs/$ErF_3$/GaAs(111)A structure is shown in Fig. 6.67. The image shows rectangular shape islands, between 100 and 300 nm wide. Their shape is different than that of the InP islands on the $LaF_3$ film which had parallelogram or triangular shape with edge angles of 60 or 120°. The rectangular shape of the GaAs islands reflects the orthorhombic face of $ErF_3$ consistent with the LEED study of the orthorhombic rare-earth fluoride deposited on a semiconductor substrate [10] where the orthorhombic $a \times c$ face of the fluoride films was found to be aligned parallel to the (111) hexagonal face of the semiconductor substrates.

### 6.1.2 Chemical nature of islands

In order to verify that the islands are in fact the semiconductors that we expect, we have performed the X-ray photoelectron spectroscopy on one of the InP/$LaF_3$/InP(111)B

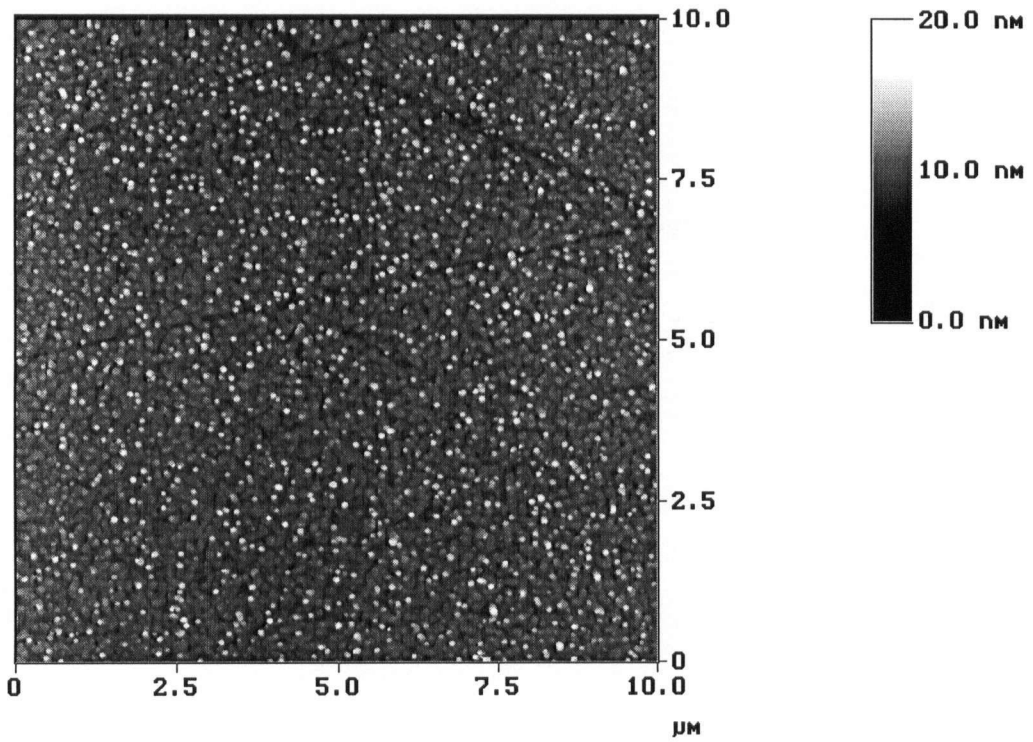


Figure 6.64: AFM image of the surface of a InP/$LaF_3$/GaAs(111)A sample ($10\mu m \times 10\mu m$).

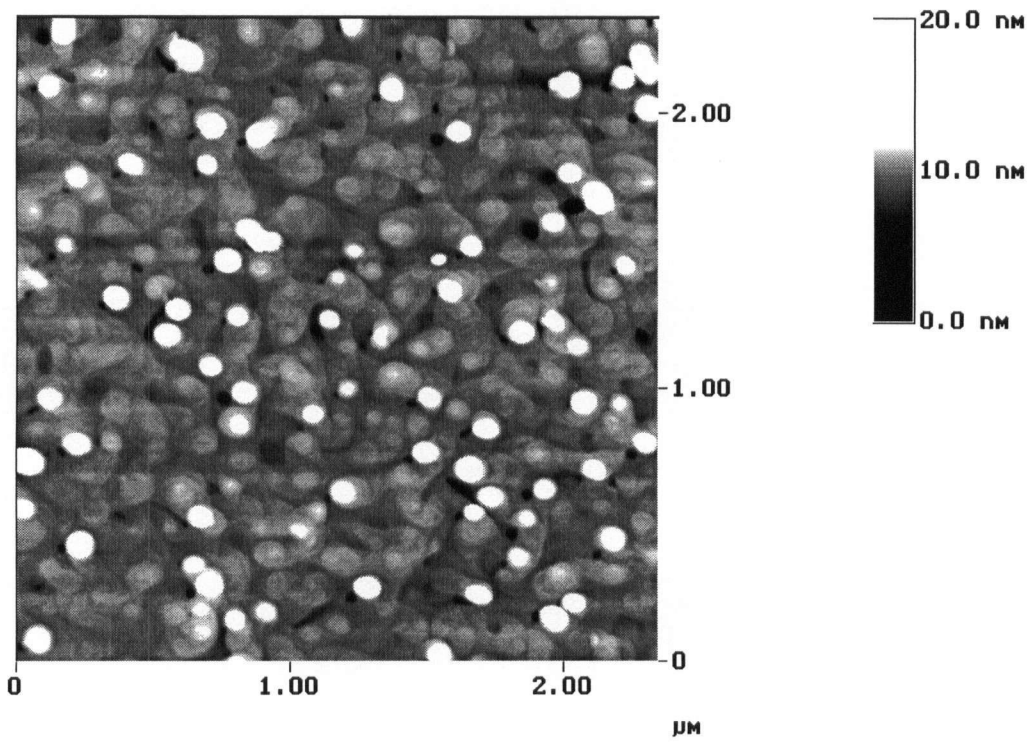


Figure 6.65: AFM image of the surface of the InP/$LaF_3$/GaAs(111)A sample in Fig. 6.64 ($2.4\mu m \times 2.4\mu m$).

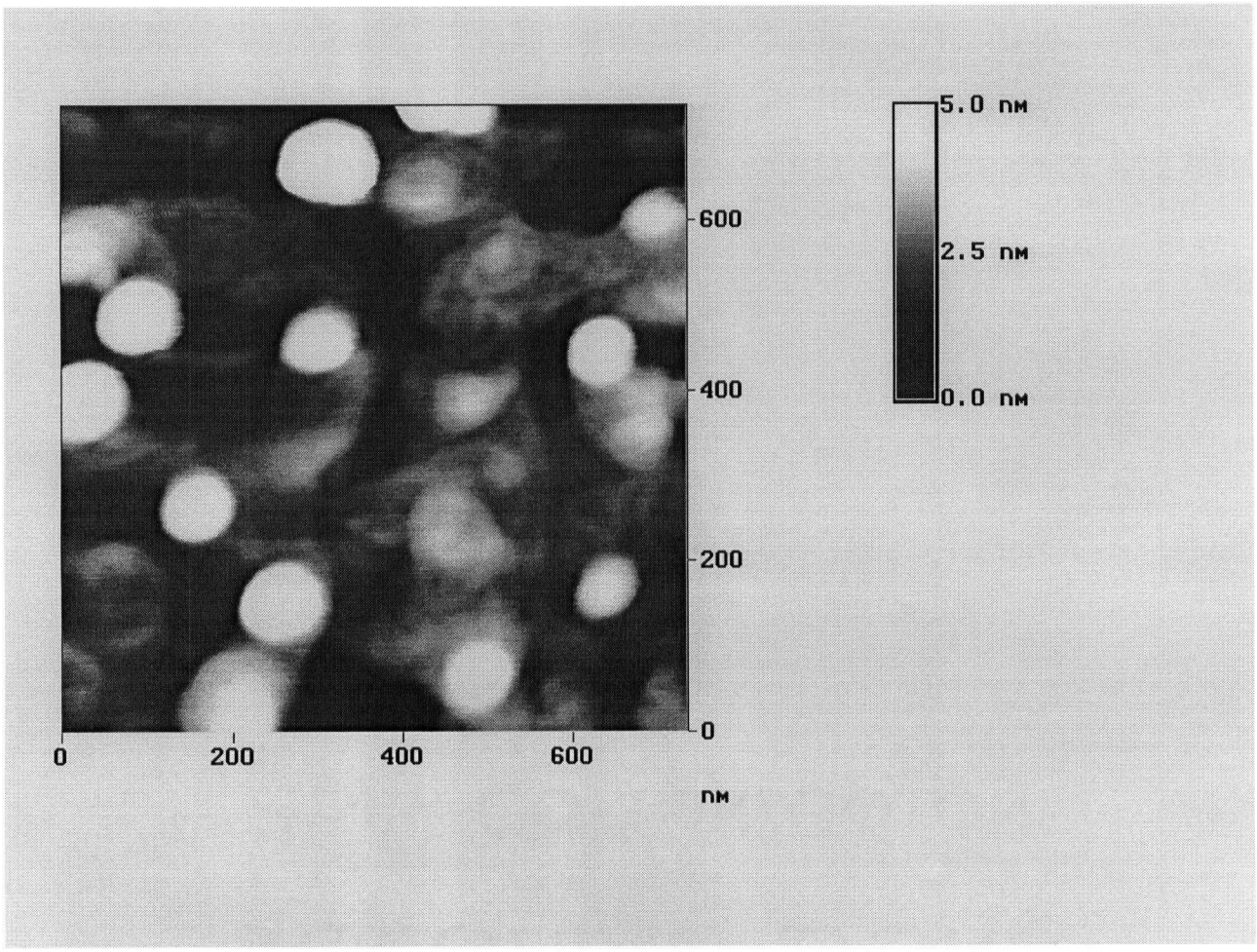


Figure 6.66: AFM image of the surface of the $InP/LaF_3/GaAs(111)A$ sample in Fig. 6.64 ($0.7\mu m \times 0.7\mu m$).

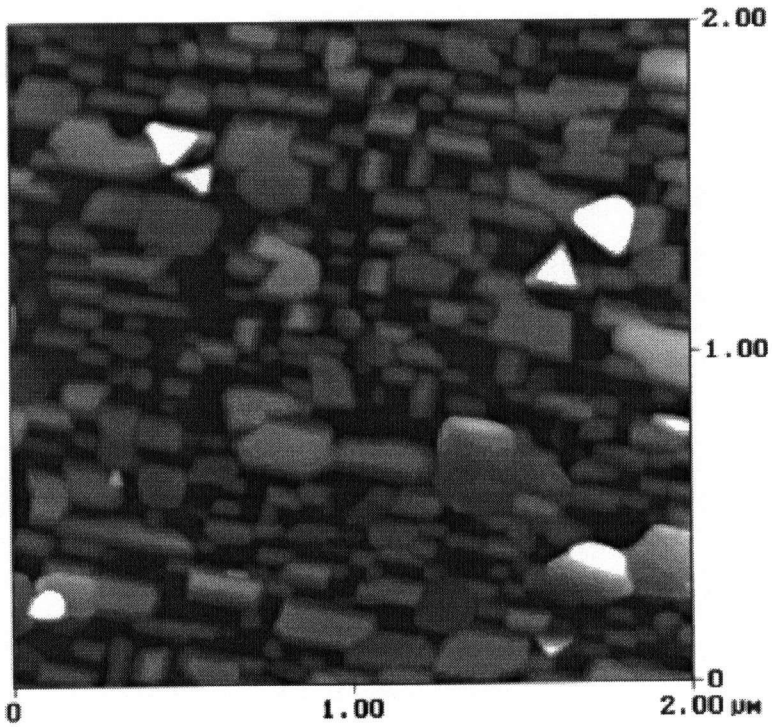


Figure 6.67: AFM image of a GaAs/$ErF_3$/GaAs(111)A sample showing rectangular shape GaAs islands.

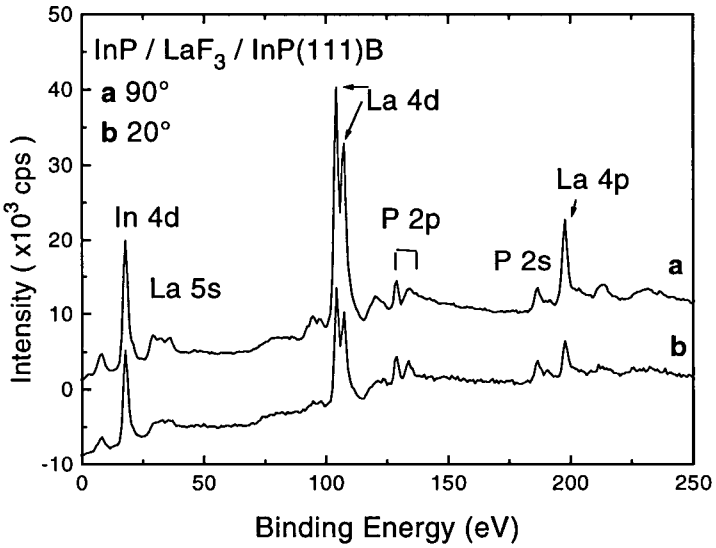


Figure 6.68: X-ray photoelectron spectra of the $InP/LaF_3/InP(111)B$ sample taken at the take-off angle of 90° and 20°. The intensity of $LaF_3$ photoelectron peaks relative to the InP peaks decreases with decreasing take-off angle.

samples (the sample shown in Fig. 6.61). The photoelectron spectra taken at two different take-off angles, 90° and 20°, are shown in Fig. 6.68. The photoelectron spectra show both InP and $LaF_3$ peaks as indicated in the figure. The intensity of the $LaF_3$ photoelectron peaks relative to the InP intensities decreases with decreasing take-off angle.

In order to express the intensity ratio of the island peak (InP) to the peak from the layer underneath ($LaF_3$) as a function of the take-off angle $\theta$, assume the islands have width $L$ and thickness $d$ as shown in Fig. 6.69. Further assume that the separation between the islands is $L$. At the photoelectron take-off angle $\theta$, an area of width $x$ is shadowed by the islands. The inelastic mean free path in InP for the kinetic energy of $E_k = 1500$ eV is $\lambda = 2.5$ nm [25]. For the $InP/LaF_3/InP(111)B$ sample studied, the thickness of the InP islands is estimated to be $t = 40 - 70$ nm from the SEM micrograph. Since $t \gg \lambda(E_k)$, the intensities from the InP islands and the $LaF_3$ layer are proportional to their respective exposed surface areas. Therefore the intensity of a photoelectron peak

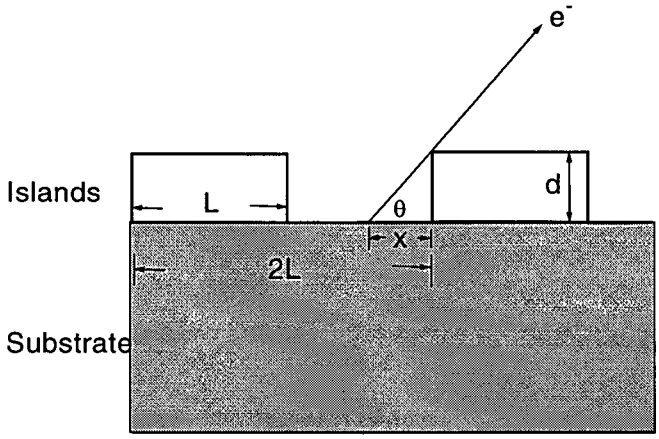


Figure 6.69: Schematic illustration showing a substrate covered by islands of width L and thickness d and the photoelectron collected at take-off angle $\theta$.

from the InP islands is proportional to $L + x$ and the intensity from the $LaF_3$ layer is proportional to $L - x$. Consequently the intensity ratio of an InP island peak to a $LaF_3$ peak is:

$$\frac{I_{InP}}{I_{LaF_3}} = \frac{I^{\infty}_{InP}}{I^{\infty}_{LaF_3}} \frac{L + d/\tan\theta}{L - d/\tan\theta} \tag{6.43}$$

where $I^{\infty}_{InP,LaF_3}$ is intensity of the photoelectrons from the sample of thickness $t \gg \lambda(E_k)$ where $\lambda(E_k)$ is the inelastic mean free path of the photoelectrons with kinetic energy $E_k$. According to Eqn. 6.43, the intensity ratio of the InP to the $LaF_3$ peaks increases with increasing value of $1/\tan\theta$.

In Fig. 6.70, the intensity ratio of In 4d to La 4d core levels is plotted as a function of $1/\tan\theta$. The intensity ratio increases with increasing value of $1/\tan\theta$ (more grazing take-off angle), confirming that InP islands are above the $LaF_3$ layer. The fit of Eqn. 6.43 is also plotted in Fig. 6.70. The value of $d/L$ was determined as $d/L = 0.1$ from the fit. Since the island thickness $d$ was 30–40 nm as estimated from the SEM image, the island

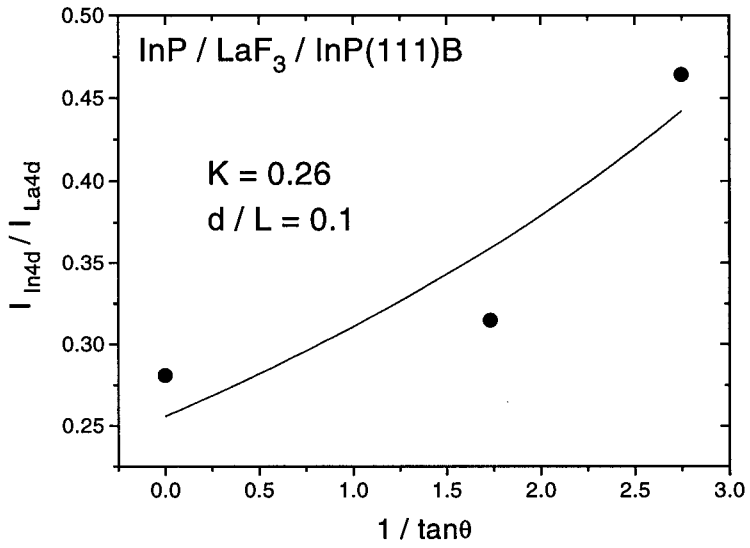


Figure 6.70: Intensity ratio of In 4d to La 4d core levels as a function of $1/\tan\theta$ for the $InP/LaF_3/InP(111)B$ sample. The intensity ratio increases indicating that InP is on top of the $LaF_3$ layer. The solid line is a fit of Eqn. 6.43. The value of $K$ was determined as $K = I^{\infty}_{In4d}/I^{\infty}_{La4d} = 0.26$. The ratio $d/L$ was determined as $d/L = 0.1$.

width and the island spacing $L$ is estimated as $L \simeq 300$–$400$ nm. The estimated value of $L$ is in good agreement with the AFM value, $L = 300$–$500$ nm.

X-ray specular reflectivity was also measured on the $InP/LaF_3/GaAs(111)A$ sample and is shown in Fig. 6.71. The specular reflectivity shows two peaks one at $q_z = 0.23$ nm$^{-1}$ and other at $q_z = 0.42$ nm$^{-1}$. The critical angle of $LaF_3$, $\theta_c = \sqrt{2\delta} = 0.00563$ rad corresponds to the $q_z$ value of $q_{zc} = 2k\sin\theta_c = 0.459$ nm$^{-1}$ where $k = 2\pi/\lambda = 40.8$ nm$^{-1}$ and $\lambda = 0.15405$ nm is the wavelength of the Cu K$\alpha$ radiation. Similarly, the $q_z$ value corresponding to the critical angle of InP is $q_z = 0.421$ nm$^{-1}$. The specular reflectivity measures the density variation along the $z$ direction. Since the top InP layer in the $InP/LaF_3/InP$ sample was comprised of islands, the average density in the x-y plane is lower than that of InP. If the InP island coverage was approximately 50 %, critical angle for total external reflection would be at $\theta = \sqrt{2\delta_{InP}/2} = 0.00398$ rad or at

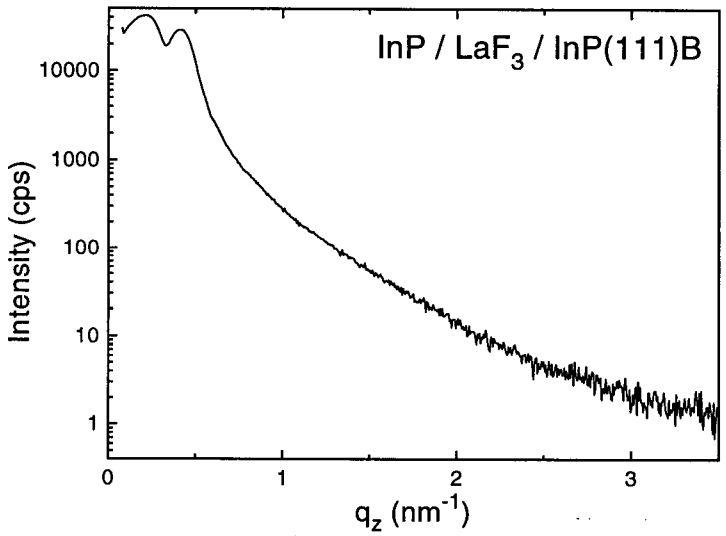


Figure 6.71: X-ray specular reflectivity of the InP/$LaF_3$/InP(111)B sample. The specular reflectivity shows two peaks one at the position corresponding to the critical angle of InP and another corresponding to the critical angle of $LaF_3$. This is particular to the island growths.

$q_z = 2k \sin\theta_c = 0.33$ nm$^{-1}$ roughly in agreement with the $q_z$ value of the peak at a lower $q_z$. We interpret the peak at higher $q_z$ as the reflection from the InP/$LaF_3$ interface. X-ray specular reflectivity is consistent with the islands observed in the AFM and SEM images being InP and the coverage of the islands being approximately 50 %.

### 6.1.3 Crystallinity and strains in the InP islands on fluoride structures

In order to see the crystallinity of the InP islands and the strains in the islands, we have performed the X-ray diffraction. A HRXRD $\theta$–$2\theta$ scan showing the InP(111) peak and the $LaF_3$(002) peak is shown in Fig. 6.72 for the InP/$LaF_3$/InP(111)B sample in the AFM image in Fig. 6.61. A $\theta$–$2\theta$ scan from a $LaF_3$/InP(111)B sample is also shown in Fig. 6.72 for comparison. The FWHM of the InP(111) peak from the InP/$LaF_3$/InP(111)B sample 85 arcsec, is more than double of FWHM$\sim$ 25 arcsec. of the InP(111) peak from the

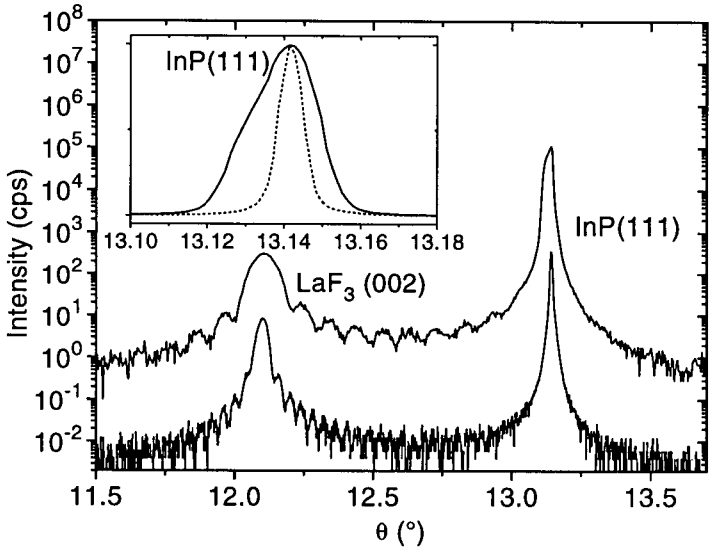


Figure 6.72: HRXRD $\theta$–$2\theta$ scan of a InP/$LaF_3$/InP(111)B sample (top). A $\theta$–$2\theta$ scan from a $LaF_3$/InP(111)B sample is also shown (bottom). The inset shows the enlarged InP(111) peaks revealing the broadening.

$LaF_3$/InP(111) sample.

Since the broadening was observed in the sample with InP islands on a fluoride film, but not in the samples with only fluorides on semiconductors, the presence of InP islands must be associated with the broadening. We were able to fit the broadened peak with two Gaussian functions. The separations of two components was $\Delta\theta = -0.012 \pm 0.003°$, as shown in the inset in Fig. 6.72. The intensity of the smaller peak is too large to interpret it as arising from a layer of 40 nm thick islands. One interpretation is that the broadening is caused by an inhomogeneous strain in the InP substrate. As we have observed by X-ray diffraction in Chapter 4, the strains develop in the $LaF_3$ films on semiconductors during cooling due to the differential thermal contractions between the film and the substrate. The $LaF_3$ films have tendencies to contract more than the semiconductor substrates because of their larger thermal expansion coefficients. In the InP island system on fluorides, the InP islands act like clamps to prevent the $LaF_3$ films from contracting

according to the thermal contraction of the fluoride, but instead, help the $LaF_3$ films to contract according to the thermal contraction of the InP substrate. As a result, parts of the $LaF_3$ films where there are no InP islands on top, would have tendencies to contract more than the parts with InP islands on top in order to compensate the loss of contraction. This inhomogeneous contractions of the $LaF_3$ films can cause an inhomogeneous strain in the InP substrate.

If we assume that the larger component of the InP peak is unstrained, then from the separation of the two component, we can estimate the strains in the component of the substrate. The separation of the peak corresponds to a strain perpendicular to the interface of $\varepsilon_\perp = 0.0009 \pm 0.0002$. For a stress in the $\langle \bar{1}\bar{1}2 \rangle$ direction, the relationship between the in-plane strain $\varepsilon_\parallel$ and the perpendicular strain $\varepsilon_\perp$ (along the $\langle 111 \rangle$ direction) is given by [37]:

$$\varepsilon_\parallel = -\frac{1}{2}\frac{C_{11} + 2C_{12} + 4C_{44}}{C_{11} + 2C_{12} - 2C_{44}}\varepsilon_\perp \tag{6.44}$$

where $C_{ij}$ are the elastic constants of InP, $C_{11} = 10.11 \cdot 10^{10}$ N m$^{-2}$, $C_{12} = 5.61 \cdot 10^{10}$ N m$^{-2}$ and $C_{44} = 4.56 \cdot 10^{10}$ N m$^{-2}$ [76]. The in-plane strain $\varepsilon_\parallel$ is thus calculated as $\varepsilon_\parallel = -0.0015 \pm 0.0003$, which is compressive. This is consistent with our interpretation in which parts of the InP substrate are compressively strained.

Powder X-ray diffraction was performed on a InP/$LaF_3$/GaAs(111) sample and is shown in Fig 6.73. The $\theta$–$2\theta$ scan shows the (004) reflection of the $LaF_3$ film, the (222) reflection of the GaAs substrate and a small peak which we interpret as the InP(222) peak. The GaAs(222) as well as the $LaF_3$(004) peak show doublets corresponding to Cu K$\alpha$1 and Cu K$\alpha$2.

The width of the X-ray diffraction peaks can be interpreted as being associated with the size of the coherent crystals. The Bragg peak of the InP islands on the $LaF_3$/InP(111) structure in the HRXRD in Fig. 6.72 as well as those observed in the powder XRD

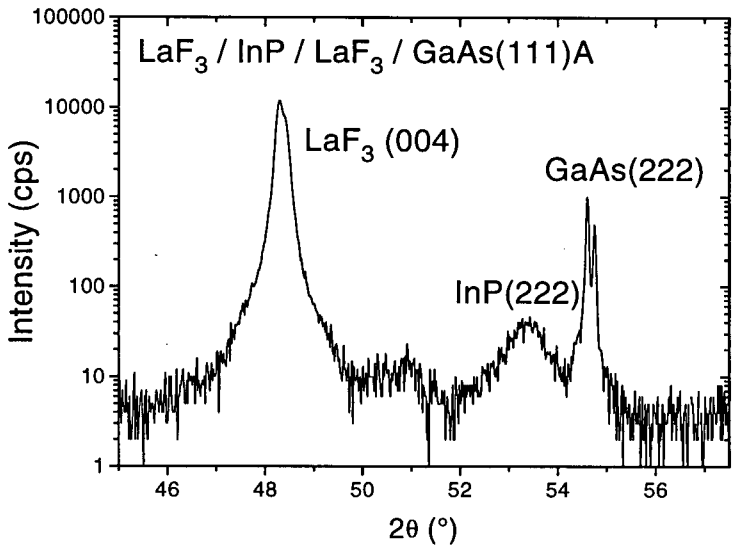


Figure 6.73: $\theta$-$2\theta$ scan of the InP/$LaF_3$/GaAs(111)A sample using a powder X-ray diffractometer. It shows $LaF_3$(004) reflection, GaAs(222) reflection from the substrate and a small peak which we interpret as the InP(222) reflection from the InP islands.

of the same sample were significantly narrower than those of the InP islands on the $LaF_3$/GaAs(111) structure. The comparison suggests that the crystal size for the InP islands on $LaF_3$/InP is larger than the crystal size for the InP islands on $LaF_3$/GaAs. The result is consistent with the longer lateral coherence lengths of the $LaF_3$ films grown on InP substrates as compared to that of the $LaF_3$ films grown on GaAs substrates.

### 6.1.4 Self-affine surface structure analysis of the InP islands on $LaF_3$

In Chapter 5, the structure of laterally homogeneous surfaces (fluoride thin films, semiconductor substrates) was analysed in terms of a scale invariant, self-affine, structure model. In this section we apply the same analysis to the laterally inhomogeneous semiconductor island systems, and show that we obtain comparable quality fits to the height-height correlation function as in the homogeneous systems.

The morphology of the InP islands on $LaF_3$ was investigated by AFM. The roughness

exponent $\alpha$ which appears in the scaling relationship: $\sigma \propto L^{\alpha}$, was determined from AFM images. The height-height correlation function $C(r)$ and the mean square fluctuation $g(r)$ were directly computed from the height information from AFM images as described in Chapter 5. The roughness exponent was determined from the mean square fluctuation $g(r)$ for small $r$ given in Eqn. 5.32:

$$g(r) \simeq 2\sigma^2(\frac{r}{\xi})^{2\alpha} \tag{6.45}$$

The correlation length $\xi$ and the rms interface width $\sigma$ is determined by fitting Eqn. 5.14: $C(r) = \sigma^2 e^{-(r/\xi)^{2\alpha}}$ to the correlation function $C(r)$ computed from the AFM image. The $\alpha$ was fixed to the value obtained from the fit to $g(r)$.

The mean square fluctuation $g(r)$ and the correlation function $C(r)$ computed from the AFM image in Fig. 6.61 for the $InP/LaF_3/InP(111)B$ sample, are shown in Fig. 6.74. The roughness exponent $\alpha$ for the $InP/LaF_3/InP(111)B$ sample was determined as: $\alpha = 0.73 \pm 0.03$ from the fit of Eqn. 5.32 to $g(r)$. The correlation length $\xi$ and the rms surface roughness $\sigma$ were found to be $\xi = 68.7 \pm 0.6$ nm and $\sigma = 17.5 \pm 0.06$ nm respectively. If we assume that the islands have a sinusoidal shape, the estimated thickness $d$ of the InP islands is approximately $d \simeq 2\sqrt{2}\sigma = 50$ nm which is similar to the value estimated from the SEM image in Fig. 6.62, $t = 30 - 40$ nm. The correlation length $\xi$ is approximately quarter of the islands size (300-500 nm).

The roughness exponent $\alpha$ was also determined for the $InP/LaF_3/GaAs(111)A$ sample shown in Fig. 6.65. The height-height correlation $C(r)$ and the mean square fluctuation $g(r)$ computed from the AFM image in Fig. 6.65 are shown in Fig. 6.75. The linear fit of Eqn. 5.32 to $g(r)$ to obtain the roughness exponent $\alpha$ and the fit of the correlation function in Eqn. 5.14, $C(r) = \sigma^2 e^{-(\frac{r}{\xi})^{2h}}$, to determine the correlation length $\xi$ and the rms surface roughness $\sigma$, are also shown in the figure. The roughness exponent $\alpha$ was determined as $\alpha = 0.76 \pm 0.03$ from the fit. The correlation length $\xi$ and the rms surface

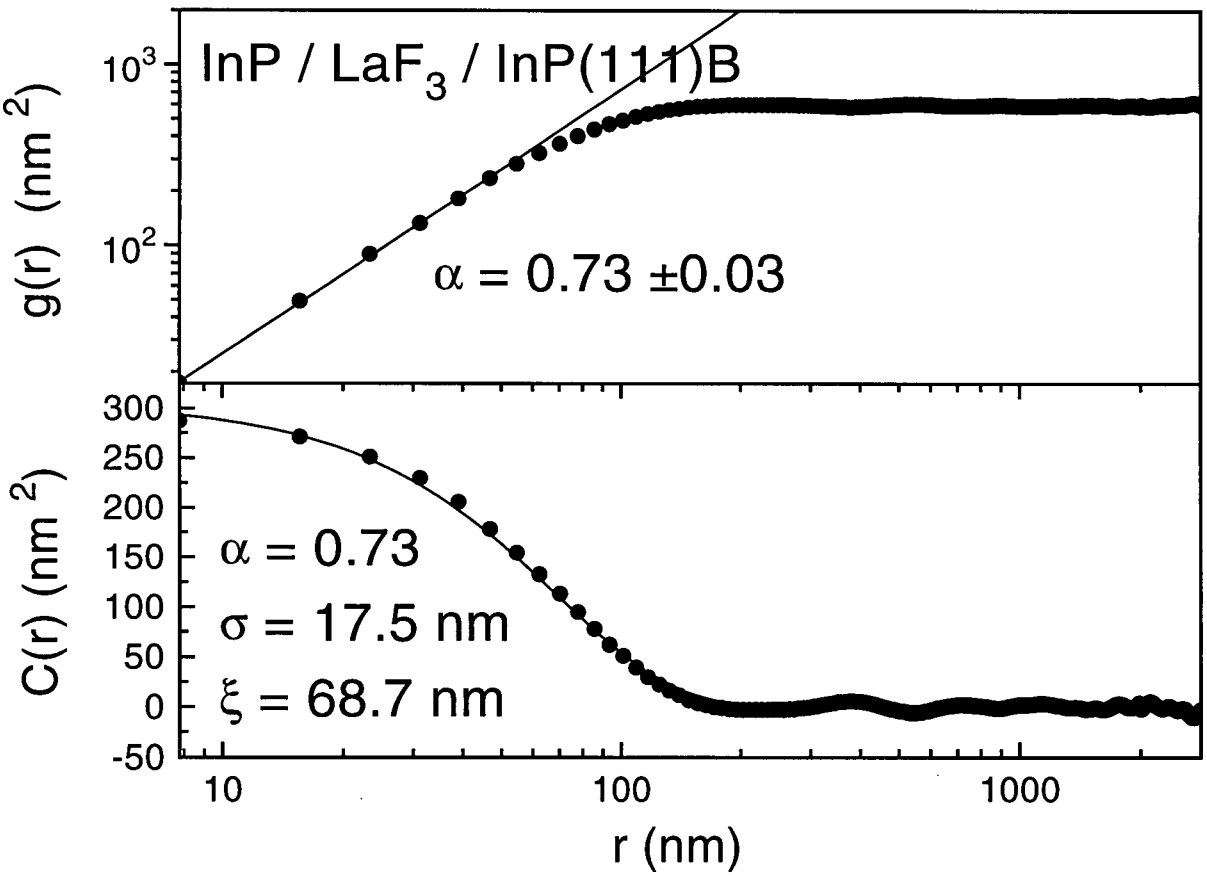


Figure 6.74: The mean square fluctuation $g(r)$ (a) and the height-height correlation $C(r)$ (b) obtained from the AFM image of the $InP/LaF_3/InP(111)B$ sample in Fig. 6.61. The solid line in (b) is the linear fit of Eqn. 5.32 to $g(r)$ to determine the roughness exponent $\alpha$. The roughness exponent $\alpha$ was determined as $\alpha = 0.73 \pm 0.03$ from the fit. The solid line in (b) is the fit of a function $C(r) = \sigma^2 e^{-(\frac{r}{\xi})^{2\alpha}}$ to the height-height correlation $C(r)$ obtained from the AFM image.

Table 6.12: Comparison of the roughness exponent $\alpha$ for the $InP/LaF_3/GaAs$, InP system with those of the $LaF_3/GaAs$, InP system.

| | Roughness Exponent $\alpha$ |
|---|---|
| $InP/LaF_3/InP(111)B$ | $0.73 \pm 0.03$ |
| $InP/LaF_3/GaAs(111)A$ | $0.76 \pm 0.03$ |
| $LaF_3/GaAs(111)A$ | $0.6 \pm 0.1$ |
| $LaF_3/InP(111)B$ | $0.6 \pm 0.1$ |

roughness $\sigma$ were determined as $\xi = 32$ nm and $\sigma = 3.2$ nm. The correlation length $\xi$ is about half of the diameter of the islands observed in the AFM image as expected.

We compare the roughness exponents $\alpha$ obtained for the $InP/LaF_3/GaAs$, InP system with those of the $LaF_3/GaAs$, InP system in Table 6.12. The roughness exponents $\alpha$ of the $InP/LaF_3/InP$ system and the $InP/LaF_3/GaAs$ system are close to each other, suggesting that the growth kinetics of the InP islands are similar in both systems. The roughness exponents for the $InP/LaF_3/GaAs$, InP system and those of the $LaF_3/GaAs$, InP system are also similar to each other.

The power spectral density (PSD) $S(q)$ of the $InP/LaF_3/InP$, GaAs(111) systems were also computed from the AFM image and are shown in Fig. 6.76. The Fourier transforms of the correlation function: $C(r) = \sigma^2 e^{-(r/\xi)^{2\alpha}}$ using the parameters obtained from the fits of correlation functions from AFM are also plotted in Fig. 6.76. This is plotted to estimated the cut-off in $q$ as we have discussed in Chapter 5. The PSDs for both $LaF_3$ on InP and GaAs showed power law behaviours: $S(q) \propto q^{-z}$ with $z \sim 4$ above the cut-offs

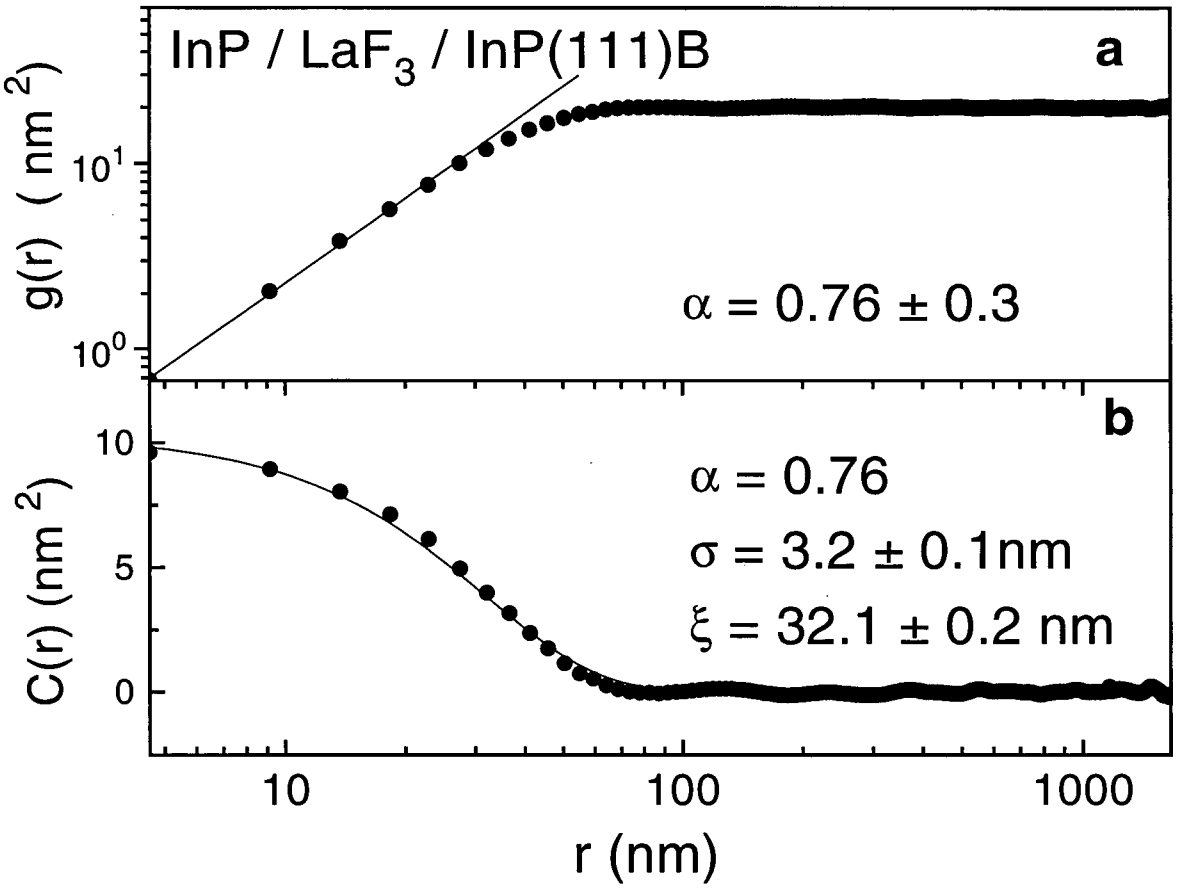


Figure 6.75: The mean square fluctuation $g(r)$ (b) and the height-height correlation $C(r)$ (a) obtained from the AFM image in Fig. 6.65. The solid line in (a) is the linear fit to $g(r)$ to determine the roughness exponent $\alpha$. The solid line in (b) is the fit of a function $C(r) = \sigma^2 e^{-(\frac{r}{\xi})^{2h}}$ to the correlation $C(r)$ obtained from the AFM image. The parameters obtained from the fits are indicated in the figure.

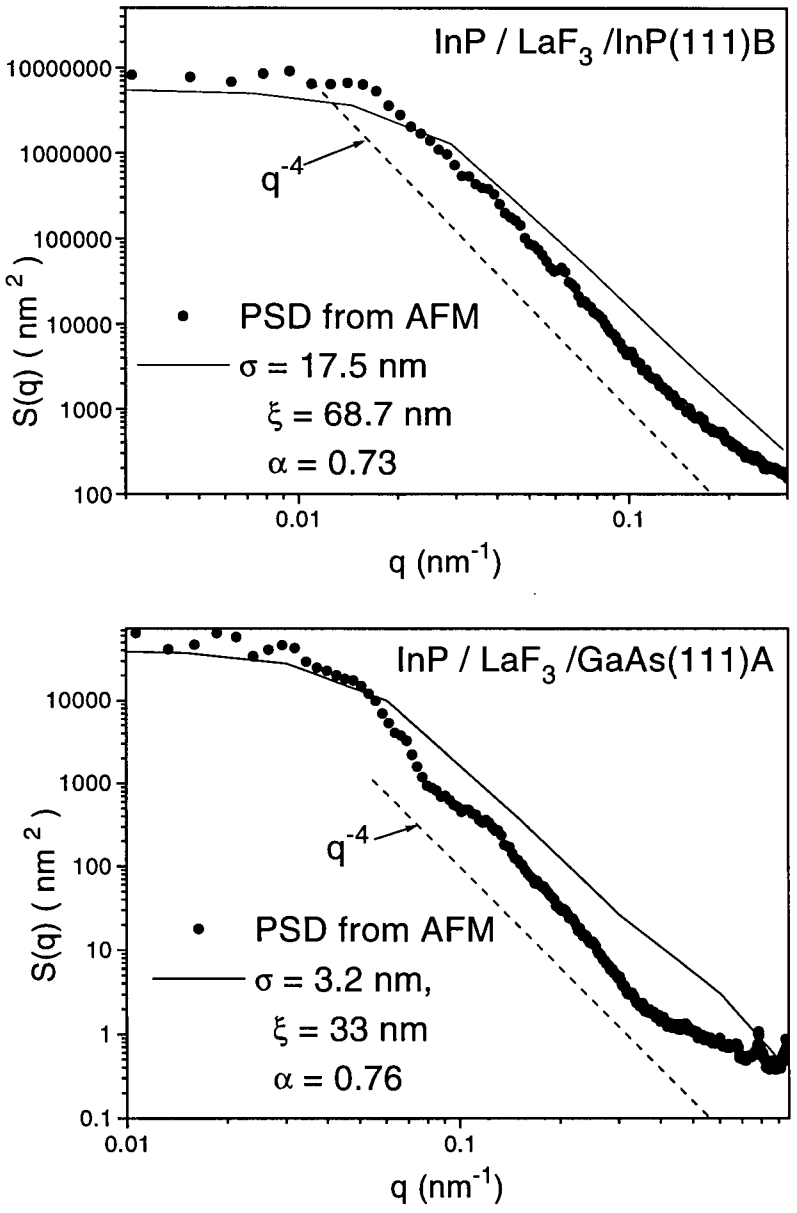


Figure 6.76: The PSD $S(q)$ for the $InP/LaF_3/InP(111)B$ sample (top) and the $InP/LaF_3/GaAs(111)A$ sample (bottom) shown in the AFM images in Fig. 6.61 and Fig. 6.65. The solid lines show the Fourier transforms of the correlation function $C(r)$ from the fits in Fig. 6.74 and 6.75. The dashed lines are the power law $q^{-z}$ where $z = 4$

$(q > q_0)$.

## 6.2 Summary

In this chapter, the growth of semiconductor/rare-earth fluoride/semiconductor structure has been investigated. The formation of the three-dimensional InP islands on the $LaF_3$/InP, GaAs(111) structures was observed. The island formation was expected because of the lower surface energy of the fluoride as compared to that of the semiconductors. The formation of GaAs islands was also observed on the $ErF_3$/GaAs(111)A structure. GaAs did not grow on $LaF_3$/GaAs(111) with the present growth condition (growth temperature of 600°C, III-V ratio of $As_2/Ga \sim 4$) likely due to the large mismatch (+3.8 %) between GaAs and $LaF_3$. The result shows that the lattice mismatch is an important factor in the fabrication of semiconductor/rare-earth trifluoride/semiconductor structure.

A strained InP component was observed by HRXRD in the InP/$LaF_3$/InP(111)B system. We interpret the component as parts of the InP substrate strained due to the differential thermal contraction between the InP islands, the $LaF_3$ layer and the InP substrate.

The self-affine surface structure analysis of the InP islands on $LaF_3$ was carried out by atomic force microscopy. We have obtained a comparable quality fits for the height-height correlation function of this system as in the homogeneous $LaF_3$ on semiconductor system in Chapter 5. The result shows that the self-affine surface structure analysis can also be applied to a laterally inhomogeneous semiconductor island system namely the InP/$LaF_3$/InP structure.

In order for the epitaxial rare-earth trifluoride films to be used in the device application, the growth conditions must be improved. Mixing other rare-earth fluorides into the fluoride layer to lattice match the semiconductor film or growing lattice matched

semiconductor layers on the fluoride layer may improve the quality of the semiconductor layers. The present study shows some promises towards a use of epitaxial rare-earth trifluoride films in the III-V semiconductor technologies.

# Chapter 7

## Conclusion

Epitaxial growth of the $LaF_3$ and $ErF_3$ films on GaAs(111) and InP(111) substrates by molecular beam epitaxy has been investigated. High-resolution X-ray diffraction showed a $LaF_3$(002) peak 100 arcsec in width aligned with (111) direction of the InP substrate indicating a high quality epitaxial growth. The epitaxial growth of $LaF_3$ films on InP was demonstrated for the first time.

We observed columnar structures in the $LaF_3$ films deposited on GaAs and InP by scanning electron microscopy. The columnar structure is consistent with the structure zone model by Thornton [45]. The growth of the $LaF_3$ films was done in the temperature range where the films are expected to have a dense columnar microstructure.

From the epitaxial film growth point of view, the columnar structure is that the columnar defect structures are formed to relieve the strains due to the lattice mismatch at the growth temperature and that the strain relieving defects are regions surrounding columns of coherent crystals. The lateral bulk coherence lengths in the $LaF_3$ films obtained from X-ray rocking curve measurements were comparable to the defect spacings required to accommodate the lattice mismatch at the growth temperature. The lateral coherence lengths are longer in $LaF_3$ films on InP than on GaAs consistent with the smaller lattice mismatch at the growth temperature in $LaF_3$ on InP.

We showed that the surface correlation lengths of $LaF_3$ films on GaAs and InP obtained by X-ray diffuse scattering were equal within the experimental accuracy to the lateral bulk coherence lengths from X-ray rocking curves. This result is consistent with

the strain relieving columnar defect structures of the $LaF_3$ films on semiconductors. The coherent crystals in the $LaF_3$ films propagate perpendicular to the interface. Consequently the columnar structures are reflected in the surface structure. The surface correlation lengths were longer for $LaF_3$ films on InP than on GaAs because the lattice mismatch at the growth temperature is smaller for $LaF_3$ on InP.

The residual tensile strains observed in $LaF_3$ films on GaAs were in agreement with the strain relieving defect interpretation of columnar structures of the films. According to our interpretation that the strains due to the lattice mismatch are relieved by formation of defects surrounding columns of coherent crystals. During cooling, the $LaF_3$ films have tendencies to contract more than the semiconductor substrates because of the larger thermal expansion coefficients of fluorides. However, if the defects are pinned at the interface, the columns of coherent crystals are unable to accommodate the differential thermal contraction between the film and the substrate. In such case, the columns of coherent crystals in $LaF_3$ films are forced to contract according to the thermal contraction of the semiconductor substrates resulting in the tensile strains in the films. The tensile strains observed by HRXRD were also consistent with the columnar strain relieving defect structure of $LaF_3$ films.

We applied a self-affine surface structural analysis on the fluoride on semiconductor systems using the X-ray diffuse scattering and the atomic force microscopy (AFM). We were able to fit the X-ray diffuse intensities and the height-height correlation functions from atomic force microscopy using a self-affine surface structure model [49]. We obtained a good agreement between the two techniques on the scaling exponents, surface roughness and surface correlation lengths of $LaF_3$ films on semiconductors. The scaling exponents obtained by X-ray scattering and AFM were consistent with the scaling exponents predicted by the Villain-Lai and Das Sarma model [53, 54].

We demonstrated the growth of single crystal InP islands on the $LaF_3$/InP(111)

structure. We showed that the self-affine surface analysis can be applied to a laterally inhomogeneous semiconductor on insulator system, namely InP islands on $LaF_3$. The superior crystal quality of InP islands grown on a $LaF_3$/InP structure as compared to InP islands on a $LaF_3$/GaAs showed that the lattice mismatch between the semiconductor and the fluoride is an important factor in this system. The strain analysis by XRD showed that differential thermal expansions between the semiconductor and the fluoride are also important in this heteroepitaxial semiconductor/fluoride system.

In this study, we demonstrated the growth of epitaxial $LaF_3$ and $ErF_3$ films on (111) GaAs and InP substrates. Epitaxial growths of high quality epitaxial fluoride films on III-V semiconductors are important for applications such as integrated optoelectronic devices. We showed that the $LaF_3$ films on semiconductors possess columnar structures and established the direct relationship between the lattice mismatch in the fluoride/semiconductor system and the columnar defect structures. Characterizing film structures and understanding the origins of formations of the structures are necessary in controlling the film growths and improving the fluoride film qualities. In order for the epitaxial rare-earth trifluoride to be incorporated in the III-V technology, more research is needed. This includes making better semiconductor films on $LaF_3$ and finding a condition to grow the trifluoride films on (100) semiconductor substrates. Studying electronic and optical properties of trifluoride/semiconductor structures and developing the etching/microfabrication technology using epitaxial fluorides are also useful in the advancement of the epitaxial fluoride technology.

# Appendix A

## Calculation of hydrogen exposures

The hydrogen exposure for a given $H_2$ pressure and a exposure time of atomic hydrogen etching is calculated as follows. Using an ideal gas approximation, the number density $\rho$ of the $H_2$ molecules for a pressure $P$ and a temperature $T$ is given by:

$$\rho = \frac{N}{v} = \frac{P}{kT} \tag{A.46}$$

where $N$ is the number of molecules, $v$ is the velocity of the molecules and $k$ is the Boltzmann constant. For a room temperature $T = 300$ K, $kT = 4 \times 10^{-21} J$. Using the $H_2$ pressure of $P = 1.0 \times 10^{-6}$ mbar, we have:

$$\begin{aligned} \rho &= \frac{P}{kT} \\ &= \frac{1.0 \times 10^{-6} mbar}{4 \times 10^{-21} J} \frac{Nm^{-2}}{10^{-2} mbar} \\ &= 2.5 \times 10^{17}\ H_2 molecules/m^3 \end{aligned} \tag{A.47}$$

Using the equipartition theorem:

$$\frac{1}{2} m v^2 = \frac{1}{2} kT$$

where $m$ is the mass of the $H_2$ molecules and $v$ is the mean velocity of the $H_2$ molecules. Therefore the mean velocity of $H_2$ molecules is given by:

$$\begin{aligned} v &= \sqrt{\frac{kT}{m}} \\ &= \sqrt{\frac{4 \times 10^{-21}}{2 \times 10^{-3}/6 \times 10^{23}}} \\ &= 1.1 \times 10^3\ m/s \end{aligned} \tag{A.48}$$

The rate $\gamma$ of the $H_2$ molecules hitting an unit area is given by:

$$\begin{aligned} \gamma &= \frac{v\rho}{2} \\ &= 1.1 \times 10^3 \cdot 2.5 \times 10^{17}/2 \\ &= 1.4 \times 10^{19}\ H_2 molecules\ sec^{-1} m^{-2} \end{aligned} \tag{A.49}$$

The rate of $H_2$ molecules, hitting the W filament is:

$$\Gamma_{H2} = \gamma A_{fil} \tag{A.50}$$

The rate of atomic hydrogens being produced is given by:

$$\Gamma = \Gamma_{H2}\eta \tag{A.51}$$

where $\eta$ is the dissociation rate of the $H_2$ molecules. The area of the filament with length $L$ and diameter $D$ is: $A_{fil} = \pi DL = \pi(2.5 \times 10^{-4})(0.05) = 4 \times 10^{-5}\text{m}^2$. The dissociation rate $\eta$ of the $H_2$ molecules at the temperature between 1800 and 2000°C is $\eta = 0.3$ [65]. Hence the rate of atomic hydrogens being produced is:

$$\begin{aligned} \Gamma &= \Gamma_{H2}\eta \\ &= 1.4 \times 10^{19} \cdot 4 \times 10^{-5} \cdot 0.3 \\ &= 1.6 \times 10^{14}\ Hatom/sec \end{aligned} \tag{A.52}$$

The rate per unit area of atomic hydrogen reaching the sample situated at the distance $R = 3$ cm away from the filament is:

$$\begin{aligned} I &= \frac{\Gamma}{\pi R^2} \\ &= \frac{1.6 \times 10^{14}}{\pi 3^2} \\ &= 5.7 \times 10^{12}\ Hatoms\ cm^{-2} sec^{-1} \end{aligned} \tag{A.53}$$

Finally, the atomic hydrogen exposure during time $t = 10$ min. is:

$$\begin{aligned} E_H &= It \\ &= 5.7 \times 10^{12} \cdot 10 \cdot 60 \\ &= 3.4 \times 10^{16}\ Hatoms\ cm^{-2} \end{aligned} \tag{A.54}$$

The atomic hydrogen exposure for the $H_2$ molecules with the pressure $P = 1.0 \times 10^{-6}$ mbar and the exposure time 10 min. is estimated as $3 \cdot 10^{16}$ cm$^{-2}$.

## Appendix B

### Estimation of thickness of oxide and carbon layers

The thicknesses of carbon contaminants and oxide layers on a GaAs wafer are calculated using the intensity ratio of photoemission peaks before and after the oxide and carbon contaminant removal by atomic hydrogen etching. We assume that the GaAs substrate is covered with a uniform layer of oxides of thickness $d_2$ and a carbon contaminant layer of thickness $d_1$ as shown in Fig. B.77. The intensity of a substrate peak covered by a uniform layer of thickness $d$ is given by [29]:

$$I_s = I_s^{\infty} e^{-\frac{d}{\lambda(E_k)\sin\theta}} \tag{B.55}$$

where $\lambda(E_k)$ is the inelastic mean free path in the overlayers at the photoelectron energy $E_k$ of the peak, $I_s^{\infty}$ is the intensity of the substrate peak from a substrate of thickness $t \gg (E_k)$ and $\theta$ is the escape angle or the angle between the interface normal and the detector. Therefore the intensity ratio of As 3d substrate peak before and after the oxide/carbon contaminant removal is:

$$\begin{aligned} \frac{I_{As3di}}{I_{As3df}} &= \frac{I^{\infty}_{As3d} e^{-\frac{d_1+d_2}{\lambda(E_k)\sin\theta}}}{I^{\infty}_{As3d}} \\ &= e^{-\frac{d}{\lambda(E_k)\sin\theta}} \end{aligned}$$

where $I_{As3di}$ and $I_{As3df}$ are the intensities of the As 3d core levels before and after the atomic hydrogen etching. The intensity ratio of the bulk GaAs component before and after the hydrogen etching shown in Fig. 2.7 and 2.8 is $I_{As3di}/I_{As3df} = 1.2/16.4 = 0.075$.

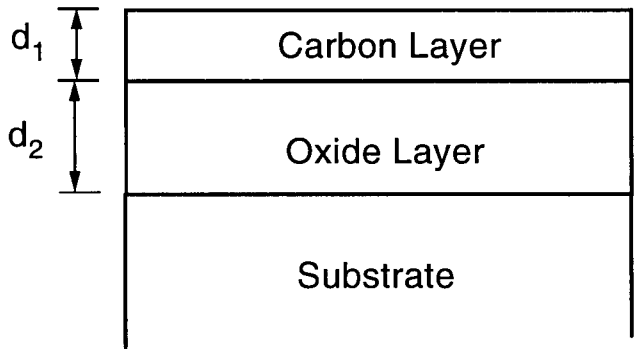


Figure B.77: Schematic illustration of a GaAs wafer covered by a uniform layer of oxides of thickness $d_2$ and the carbon contaminant layer of thickness $d_1$.

The total thickness $d = d_1 + d_2$ of the oxide/carbon contaminant layers is calculated as:

$$d = -ln\frac{I_{As3di}}{I_{As3df}}\lambda \sin\theta \tag{B.56}$$

$$= -\ln 0.075 \times 0.83 \sin 45° \tag{B.57}$$

$$\simeq 1.52\ nm \tag{B.58}$$

We have used the inelastic mean free path of $\lambda = 0.83$ nm at the photoelectron kinetic energy of 50 eV [25] and the escape angle of $\theta = 45°$ in the calculation.

The oxide thickness is estimated using a relationship between the thickness $d$ and the layer/substrate peak ratio $R = I_l/I_s$ given by [29]:

$$\ln[\frac{R}{K} + 1] = \frac{d}{\lambda(E_k)\sin\theta} \tag{B.59}$$

where $K = I_l^\infty/I_s^\infty$ is the intensity ratio of the overlayer and the substrate, both of thickness $t \gg \lambda(E_k)$ . The intensity ratio $R$ of a chemically shifted As oxide component ($As_2O_3$) to a bulk GaAs component is $R = I_{As3doxide}/I_{As3dGaAs} = 4.7/1.2 = 3.9$. The

thickness of oxide layer $d_2$ is thus:

$$d_2 = \lambda_e \sin\theta \ln[\frac{R}{K} + 1] \quad \text{(B.60)}$$

$$= 0.83 \sin 45° \ln[3.9 + 1] \quad \text{(B.61)}$$

$$\simeq 0.9\ nm \quad \text{(B.62)}$$

We assumed $K \simeq 1$ and used the inelastic mean free path of $\lambda_e = 0.83$ nm [25] and the escape angle of $\theta = 45°$ in the calculation. The thickness of the carbon contaminant layer is estimated as $d_1 = d - d_2 = 1.5 - 0.9 = 0.6$ nm.

The thicknesses of the oxide+carbon layer and the $SiO_2$ layer on the InP wafer are calculated from the photoemission intensity ratios. The surface of the InP substrate is assumed to be first covered with a uniform layer of oxide+carbon of thickness $d_2$ followed by an uniform layer of $SiO_2$ of thickness $d_1$. The thickness of the oxide+carbon layer removed by the atomic hydrogen etching is calculated from the intensity ratio of the oxide to the InP components of P 2p core levels using Eqn. B.59:

$$d_2 = \lambda_{InP} \sin\theta \ln[\frac{I_{Po}}{I_{PInP}} + 1] \quad \text{(B.63)}$$

$$= 0.48 \sin 45° \ln[\frac{3.9}{1.8} + 1] \quad \text{(B.64)}$$

$$= 0.4\ nm \quad \text{(B.65)}$$

The inelastic mean free path of $\lambda = 0.48$ nm in InP at 50 eV[25], the escape angle of $\theta = 45°$ and $K = I^{\infty}_{Po}/I_{PInP} \simeq 1$ are used in the calculation.

The thickness of $SiO_2$ layer removed by HF etching is estimated from the intensity ratio of the Si 2p and the P 2p photoemission peaks before the HF etching using Eqn. B.55. The intensity ratio $K$ of the Si 2p core levels from a SiO2 layer of thickness $t \gg E_k$ and the P 2p core levels from an InP wafer of thickness $t \gg E_k$ is approximated as [66]:

$$K = \frac{\sigma_{Si2p}}{\sigma_{P2p}}(\frac{E_{Si2p}}{E_{P2p}})^{-0.34} = \frac{3}{4}(\frac{108}{132})^{-0.34} \simeq 0.8 \quad \text{(B.66)}$$

where $\sigma_{Si2p,P2p}$ are the cross section of the Si 2p and P 2p core levels respectively from Ref. [77], $E_k$ is the kinetic energy of the photoelectrons. In Fig. 2.9, the intensities of the Si 2p and P 2p core levels are $I_{Si2p} = 16.9$ and $I_{P2p} = 1.76$. The thickness of the $SiO_2$ layer is thus estimated as:

$$d_1 = \lambda_{SiO2} \ln[\frac{1}{K}\frac{I_{Si2p}}{I_{P2p}} e^{-\frac{d_2}{\lambda_{InP}\sin\theta}} + 1] \quad \text{(B.67)}$$

$$= 0.8 \ln[\frac{1}{0.8}\frac{16.9}{1.76} e^{-\frac{0.4}{0.48\sin 45^\circ}} + 1] \quad \text{(B.68)}$$

$$= 0.88\ nm \quad \text{(B.69)}$$

The inelastic mean free path, $\lambda_{InP} = 0.48$ nm in InP at 50 eV, $\lambda_{SiO2} = 0.8$ nm in $SiO_2$ [25] and the escape angle $\theta = 45°$ are used in the calculation.

# Appendix C

## X-ray specular and diffuse reflectivity calculation

### C.1 Specular Reflectivity

The film thickness $t$ and the rms surface roughness $\sigma$ are obtained using a recursive method for stratified layers [47]. Consider a system of N stratified layers. A system with two interfaces is illustrated in Fig. C.78 as an example. For a system of $N$ stratified layers, the reflectivity $R_{j+1}$ at the top of the layer $j+1$ is given by a recursion formula:

$$\begin{aligned} R_j &= a_j^4 \frac{(R_{j+1} + F_j)}{(R_{j+1}F_j + 1)} \\ R_{j+1} &= a_j^2 E_{j+1}^r / E_{j+1} \\ F_j &= \frac{f_j(\theta) - f_{j-1}(\theta)}{f_j(\theta) + f_{j-1}(\theta)} \end{aligned} \tag{C.70}$$

where $E_{j+1}$ and $E_{j+1}^r$ are the amplitudes of the electric vectors for the incoming and reflected beams at the interface $j+1$. The amplitude $a_j$ is given by:

$$a_j = e^{(-i\pi f_j(\theta_j) d_j/\lambda)} \tag{C.71}$$

where $d_j$ is the thickness of the layer $j$ and $f_j(\theta)$ is the fresnel coefficient given by:

$$f_j(\theta_1) = (\theta_j^2 - 2\delta_j - 2i\beta_j) \tag{C.72}$$

The computation starts at the substrate level i.e. at $j = N$ by noting that $R_{N+1} = 0$. It ends at the film/air interface $j = 0$ where the reflectivity is $R_0 = E_0^r/E_0$, since $a_0 = 1$. The coefficients $\delta$ and $\beta$ are related to refractive index of the medium $n$ through:

$$n = 1 - \delta - i\beta \tag{C.73}$$

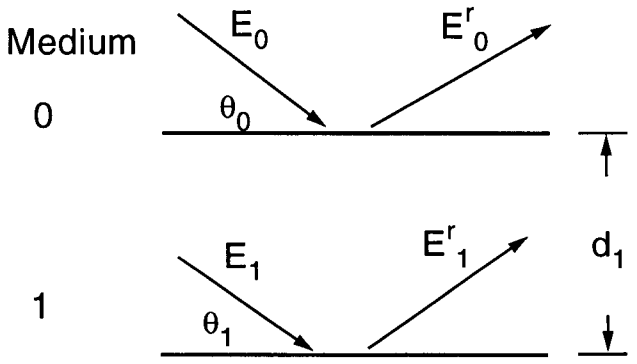


Figure C.78: Schematic illustration of a system with two interfaces. $E_i$ and $E_i^r$ are the amplitudes of the electric vectors of the incoming and reflective beams at interface $i$.

$$\delta + i\beta = \frac{r_e \lambda^2}{2\pi} N_A \sum_k \frac{\rho_k}{M_k} f_k \tag{C.74}$$

where $r_e$ is the electron radius, $\lambda$ is the wavelength of Cu K$\alpha$, $N_A$ is the Avogadro's number, $\rho_k$ is the mass density of $k$ atom in a unit cell in g/cm$^3$, $M_k$ is the atomic mass of the $k$ atom in g/mole. The quantity $f_k$ is given by: $f_{0k} + \Delta f_k' + i\Delta f_k''$. The values of $f_k$ for given ions can be found in *the International X-ray Table.* The value of $r_e N_A / 2\pi$ is given by:

$$\frac{r_e}{2\pi} N_A = \frac{2.818 \times 10^{-13}}{2\pi} 6.022 \times 10^{23} = 2.702 \times 10^{10} (CGS) \tag{C.75}$$

The effect of roughness is implemented using the expression of the reflectivity by Nevot and Croce [48] $R_j = R_{Fj} e^{q_{zj} q_{zj+1} \sigma_j^2}$ where $q_{zj}$ and $q_{zj+1}$ are the transfer vectors perpendicular to the plane of the interface for the layer above and below the interface $j$ respectively, $\sigma_j$ is the rms width of the interface $j$ and $R_F$ is the fresnel reflectivity for an ideal interface. The transfer vector $q_z$ is given by $q_{zj} = 2k_0 sin\theta \simeq 2k_0 f_j(\theta_j)$.

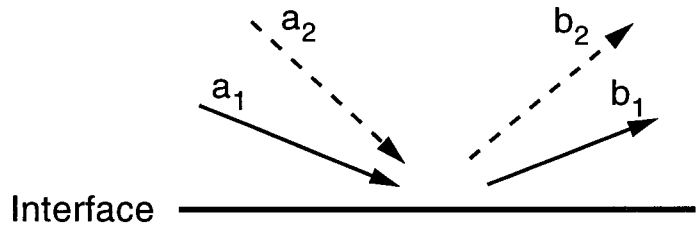


Figure C.79: Schematic illustration of an interfaces showing the incoming vectors with amplitudes $a_1$, $a_2$, and the out going vectors $b_1$, $b_2$. The incident and detected angles are $\theta_1$ and $\theta_2$ respectively.

## C.2 Diffuse Intensity

The *roughness coefficients* $\alpha$ and the correlation length $\xi$ were obtained from X-ray diffuse scattering using the expression for the diffuse intensity given by Sinha *et al.* [50]. The expression uses the distorted wave Born approximation (DWBA). Since the systems studied involve two interfaces, the diffuse intensity for the multilayer interfaces are used. Consider a system of N stratified layers. At an interface, the amplitudes of incoming vectors are defined as $a_1$, $a_2$ and those of the outgoing vectors are defined as $b_1$ and $b_2$ as illustrated in Fig. C.79. The incident and detected angles are $\theta_1$ and $\theta_2$ respectively.

For each interface, we define the transfer vectors $q_z$ and $q_{zp}$ as:

$$\begin{aligned} q_z &= k_{1z} - k_{2z} = k_0(f_1 - f_2) \\ q_{zp} &= k_{1z} + k_{2z} = k_0(f_1 + f_2) \end{aligned} \tag{C.76}$$

where $k_{1z}$ and $k_{2z}$ are the $z$ component of the incident and scattered wavevectors respectively and $k_0$ is the magnitude of the incident wavevector given by $k_0 = 2\pi/\lambda$ where $\lambda$ is the wavelength of the incident radiation. For Cu-K$\alpha$ radiation, the wavelength is $\lambda = 1.5401$Å. The function $f(\theta_j)$ is defined as:

$$f(\theta_j) = (\theta_j^2 - 2\delta - i2\beta)^{1/2} \tag{C.77}$$

where $\delta$ and $\beta$ is related to the refractive index of the medium above the interface, $n$ through $n = 1 - \delta - i\beta$. We also define four coefficients for each interface:

$$\begin{aligned} A_0 &= \frac{a_1 a_2 e^{-iq_0 z}}{q_0} \\ A_1 &= \frac{a_1 b_2 e^{-iq_1 z}}{q_1} \\ A_2 &= \frac{a_2 b_1 e^{-iq_2 z}}{q_2} \\ A_3 &= \frac{b_1 b_2 e^{-iq_3 z}}{q_3} \end{aligned} \tag{C.78}$$

where the four transfervectors are defined as:

$$\begin{aligned} q_0 &= -(k_{1z} + k_{2z}) = -q_{zp} \\ q_1 &= -(k_{1z} - k_{2z}) = -q_z \\ q_2 &= -(k_{2z} - k_{1z}) = q_z \\ q_3 &= -(-k_{1z} - k_{2z}) = q_{zp} \end{aligned} \tag{C.79}$$

The diffuse intensity is then given by:

$$I_{diff}(\theta_1, \theta_2) = \frac{\Delta\theta_2 2\pi}{k_0 \sin\theta_1} \sum_{i,j=0}^{N-1} \sum_{\mu,\nu=0}^{3} \Delta\rho_i (\Delta\rho_j)^* A_\mu(i) A_\nu(j) F_{\mu\nu}(i,j) \tag{C.80}$$

$$F_{\mu\nu}(i,j) = 2e^{-\frac{1}{2}[q_{\mu i}^2 \sigma_i^2 + q_{\nu j}^{*2} \sigma_j^2]} \int_0^\infty [e^{q_{\mu i} q_{\nu j}^* C(X)} - 1] \cos(q_x X) dX$$

where $\theta_1$ and $\theta_2$ are the incident and the scattered angles respectively and $\Delta\theta_2$ is the

angle subtended by the detector. $\Delta\rho_i$ is the density difference at the interface $i$ given by:

$$\Delta\rho_i = \frac{k_0^2}{4\pi}(n_i^2 - n_{i+1}^2) \tag{C.81}$$

where $n_i^2$ is the index of refraction of the medium above the interface given by:

$$n_i^2 = (1 - \delta_i - i\beta_i)^2 \simeq 1 - 2\delta_i - 2i\beta_i \tag{C.82}$$

The density difference at the interface $i$, $\Delta\rho_i$ becomes:

$$\Delta\rho_i = \frac{\pi}{\lambda^2}(-2(\delta_i + i\beta_i) + 2(\delta_{i+1} + i\beta_{i+1})) \tag{C.83}$$

The integral in Eqn. C.80 is evaluated numerically using the Fourier integral routine in Ref. [78].

To evaluate the amplitudes $a_i$ and $b_i$, we first calculate the reflectivity $r_i$ at each interface using the recursion method by Parratt [47]. We then set the amplitude $a_0$ of incident ray to unity and work backswords to determine the rest of the amplitudes.

The amplitudes of the incoming and the outgoing rays are defined as in Fig. C.80. The $a_j$ and $b_j$ are the amplitudes of the incoming and reflective rays at the interface $j$ in the medium above the interface. The $\alpha_{j+1}$ and $\beta_{j+1}$ are the outgoing and the incoming rays at the interface $j$ in the medium below the interface $j$. The outer most medium is defined as 0 with interface 0 below it. The layer thickness for the medium $j$ is $d_j$ and the reflectivity at the interface $j$ is $r_j$.

At the interface $j-1$, the relationship between the rays in the medium $j-1$, $a_{j-1}$, $b_{j-1}$ and the rays in the medium $j$, $\alpha_j$ and $\beta_j$ is:

$$\alpha_j + \beta_j = a_{j-1} + b_{j-1} \tag{C.84}$$

Using $\alpha_j = a_j e^{ik_j d_j}$ and $\beta_j = b_j e^{-ik_j d_j}$:

$$a_j e^{-ik_j d_j} + b_j e^{-ik_j d_j} = a_{j-1} + b_{j-1} \tag{C.85}$$

$$(a_j + b_j e^{-2ik_j d_j}) e^{ik_j d_j} = a_{j-1} + b_{j-1} \tag{C.86}$$

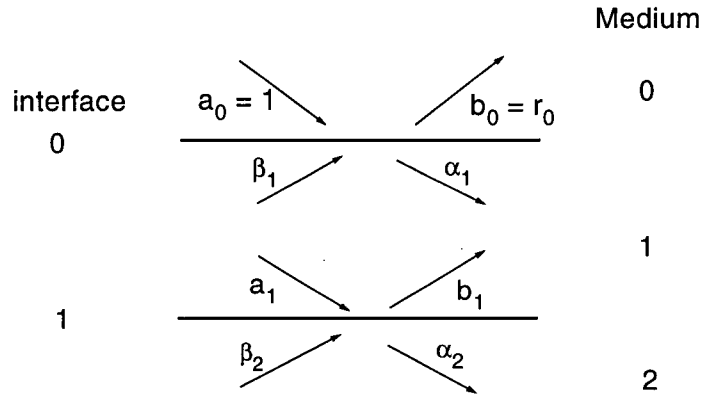


Figure C.80: Schematic illustration of a system with two interfaces. The $a_j$ and $b_j$ are the amplitudes of the incoming and the reflected rays at interface $j$ in the medium above the interface. The $\alpha_{j+1}$ and $\beta_{j+1}$ are the outgoing and incoming rays at the interface $j$ in the medium below the interface $j$.

We also know that $b_j = a_j r_j$ and $R_j = r_j e^{-2ik_j d_j}$:

$$a_j(1 + R_j)e^{ik_j d_j} = a_{j-1} + b_{j-1} \tag{C.87}$$

Finaly we obtain the amplitude $a_j$ as:

$$a_j = \frac{(a_{j-1} + b_{j-1})e^{-ik_j d_j}}{1 + R_j} \tag{C.88}$$

## Bibliography


[1] H. D. Müller and J. Schneider *Appl. Phys. Lett.* **57** 2422 (1990).

[2] R. A. McFarlene, M. Lui and D. Yap, *IEEE J. Select. Topics Quantum Electron.* **1** 82 (1995).

[3] Z. Shi, H. Zogg, P. Müller, I. D. Jung and U. Keller *Appl. Phys. Lett.* **69** 3474 (1996).

[4] H. Zogg *Appl. Phys. Lett.* **49** 933 (1986).

[5] S. Sinharoy, R. A. Hoffman, A. Rohatgi, R. F. C. Farrow and J. H. Rieger *J. Appl. Phys.* **59** 273 (1986).

[6] R. Strumpler, D. Guggi and H. Lüth *Thin Solid Films* **198** 221 (1992).

[7] S. Sinharoy, R. A. Hoffman, J. H. Rieger, W. J. Takei and R. F. C. Farrow *J. Vac. Sci. Technol.* B **3** 722 (1985).

[8] C. Malten, S. Cramm, K. M. Colbow and W. Eberhardt, *J. Vac. Sci. Technol.* A **12** 418 (1994).

[9] K. M. Colbow, Y. Gao, T. Tiedje, J. R. Dahn, J. N. Reimers, S. Cramm, *J. Vac. Sci. Technol.* A **10** 765 (1992).

[10] L. C. Jenkins, C. L. Griffiths, A. Hughes, J. Richards and R. H. Williams *J. Vac. Sci. Technol.* B **11** 1541 (1993).

[11] S. Sinharoy, R. A. Hoffman, R. F. C. Farrow and J. H. Rieger, *J. Vac. Sci. Technol.* A **3** 2123 (1985).

[12] A. Zalkin, D. H. Templeton and T. E. Hopkins *Inorg. Chem.* **5** 1466 (1966).

[13] R. W. G. Wyckoff *Crystal Structures* Vol. II (Wiley, New York) (1964).

[14] R. E. Thoma and G.D. Brunton *Inorg.Chem.* **5** 1937 (1966).

[15] Y. S. Touloukian, R. K. Kirby, R. E. Taylor and T. Y. R. Lee *Thermophysical properties of matter* v. 13 *Thermal Expansion of Nonmettallic Solids* IFI/Plenum, New York (1970).

[16] G. Hass, J. B. Ramsey and R. Thun *J. Opt. Soc. Am.* **49** 116 (1959).

[17] J. B. Mooney *Infrared Physics* **6** 153 (1966).

[18] W. Micklethwaite, Firebird Semiconductor, private communication.

[19] C. Lavoie in *Light Scattering Measurements of Surface Morphology during Molecular Beam Epitaxy Growth of GaAs-based Semiconductors* Ph. D. Thesis, The University of British Columbia (1994).

[20] G. Landgren, R. Ludeke, Y. Jugnet, J. F. Morar and F. J. Himpsel *J. Vac. Sci. Technol.* B **2** 351 (1984).

[21] S. Gourrier, P. Friedel and P. K. Larsen *Surf. Sci.* **152/153** 1147 (1985).

[22] P. Pianetta, I. Lindau, C. M. Garner and W. E. Spicer *Phys. Rev. B.* **18** 2792 (1978).

[23] G. K. Wertheim, M. A. Butler, K. W. West and D. N. E. Buchanan *Rev. Sci. Instrum.* **45** 1369 (1974).

[24] L. Sorba, M. Pedio and S. Nannarone *Phys. Rev. B* **41** 1100 (1990).

[25] S. Tanuma, C. J. Powell and D. R. Penn *Surface and Interface Analysis* **17** 927 (1991).

[26] W. R. Hunter and S. A. Malo *J. Phys. Chem. Solids* **30** 2739 (1969).

[27] S. Ritchie, S. R. Johnson, C. Lavoie, J. A. Mackenzie, T. Tiedje, R. Streater *Surf. Sci.* **374** 418 (1997).

[28] R. Z. Bachrach Synchrotron Radiation Research: advances in surface and interface science Vol. 2 R. Z. Bachrach Ed., Plenum Press, NewYork (1992).

[29] C. S. Fadley *Prog. Surf. Sci.* **16** 275 (1984).

[30] S. Hasegawa, Y. Nagai, T. Onishi, G. Honjo, *Surf. Sci.* **109** 353 (1981).

[31] A. W. Adamson *Physical Chmistry of Surfaces* 4th ed. John Wiley & Sons, New York (1982).

[32] J. Gilman *J. Appl. Phys.* **31** 2208 (1960).

[33] P. W. Tasker *J. de Physique.* **C6** C6-488 (1980).

[34] C. Messmer and C. Biello *J. Appl. Phys.* **52** 4623 (1981).

[35] Y. Gao in *Photoelectron Experiments and Studies of XANES in Alkaline-Earth and Rare-Earth Fluorides* Ph. D. Thesis, The University of British Columbia (1994).

[36] L. D. Landau and E. M. Lifshitz *Theory of Elasticity* 3rd ed. Pergamon Press, New York (1986).

[37] J. F. Nye in *Physical Properties of Crystals* Oxford University Press, London (1960).

[38] R. Laiho, M. Lakkisto and T. Levola *Phil. Mag.* A **47** 235 (1983).

[39] Shin Hashimoto, J. -L. Peng, W. M. Gibson, L. J. Schowalter and R. W. Fathauer *Appl. Phys. Lett.* **47** 1071 (1985).

[40] J. W. Matthews *in Materials Science Series: Epitaxial Growth, Part B*, J. W. Matthews Ed., Academic Press, New York, 559 (1975).

[41] L. j. Schowalter and R. W. Fathauer *CRC Critical Reviews in Solid State and Materials Sciences* **15** 367 (1989).

[42] P. Kidd, P. F. Fewster and N. L. Andrew *J. Phys. D.* **28** A133 (1995).

[43] See for example A. Mak, K. W. Evans-Lutterodt, K. Blum, D. Y. Noh, J. D. Brock, G. A. Held, and R. J. Birgeneau *Phys. Rev. Lett.* **66** 2002 (1991).

[44] P. Gay, P. H. Hirsch and A. Kelly *Acta Metal.* **1** 316 (1953).

[45] J. A. Thornton *Ann. Rev. Mater. Sci.* **7** 239 (1977).

[46] B. B. Mandelbrot *The Fractal Geometry of Nature* W.H. Freeman, New York (1992).

[47] L. G. Parratt *Phys. Rev.* **95** 359 (1954).

[48] L. Nevot and P. Croce, *Rev. Phys. Appl.* **15** 761 (1980).

[49] S. K. Sinha, E. B. Sirota, S. Garoff and H. B. Stanley, *Phys. Rev.* B. **38** 2297 (1988).

[50] S. K. Sinha *J. Phys.* III France **4** 1543 (1994).

[51] P. Meakin, P. Ramanlal, L. M. Sander and R. C. Ball *Phys. Rev.* A **34** 5091 (1986).

[52] M. Kardar, G. Parisi and Y.-C. Zhang *Phys. Rev. Lett.* **58** 2087–2090 (1987).

[53] J. Villain *J. Phys.* I **1** 19 (1991).

[54] Z.-W. Lai and S. Das Sarma *Phys. Rev. Lett.* **66** 2348 (1991).

[55] D. E. Wolf and J. Villain *Europhys. Lett.* **13** 389 (1990).

[56] S. F. Edwards and D. R. Wilkinson *Proc. R. Soc. London A* **381** 17 (1982).

[57] C. Herring *J. Appl. Phys.* **21** 301 (1950).

[58] R. L. Schwoebel and E. J. Shipsey *J. Appl. Phys.* **37** 3682 (1966).

[59] C. Thompson, C. Palasantzas, Y. P. Feng, S. K. Sinha and J. Krim *Phys. Rev.* B **49** 4902 (1994).

[60] H. -J. Ernst, F. Fabre R. Folkerts and J. Lapujoulade *Phys. Rev. Lett.* **72** 112 (1994).

[61] P. E. Hegeman, H. J. W. Zandvliet, G. A. M. Kip and A. van Silfhout *Surf. Sci.* **311** L655 (1994).

[62] R. C. Salvarezza, L. Vazquez, P. Herrasti, P.Ocon, J.M. Vara and A. J. Arvia *Europhy. Lett.* **20** 727 (1992).

[63] A. -L. Barabási, H. E. Stanley *Fractal Concepts in Surface Growth* Cambridge University Press (1995).

[64] F. Family and T. Vicsek *J. Phys.* A **18** L75–L81 (1985).

[65] J. N. Smith, Jr. and W. L. Fite *J. Chem. Phys.* **37** 898 (1962).

[66] C. D. Wagner, L. E. Davis, M. V. Zeller and J. A. Taylor, R. H. Raymond and L. H. Gale *Surf. Interface Anal.* **3** 211 (1981).

[67] C. W. Tu, S. R. Forrest, and W. D. Johnston, Jr. App. Phys. Lett. **43** 569 (1983).

[68] S. Siskos, C. Fontaine, and A. Munoz-Yague *App. Phys. Lett.* **44** 1146 (1984).

[69] T. Minemura, J. Asano and K. Tsutsui *J. Cryst. Growth* **114** 304 (1991).

[70] L. J. Schowalter, J. E. Ayers, S. K. Ghandhi *J. Vac. Sci. Technol.* **B 8** 246 (1990).

[71] S. R. Johnson, C. Lavoie, T. Tiedje and J. A. Mackenzie *J. Vac. Sci. Technol.* B **11** 1007 (1993).

[72] S. M. Heald, H. Chen and J. M. Tranquada *Phys. Rev.* B **38** 1016 (1988).

[73] T. Asano and H. Ishiwara *J. Appl. Phys.* **55** 3566 (1984).

[74] R. W. Fathauer, N. Lewis, E. L. Hall and L. J. Schowalter *J. Appl. Phys.* **60** 3886 (1986).

[75] S. Kanemaru, H. Ishiwara and S. Furukawa *J. Appl. Phys.* **63** 1060 (1988).

[76] D. N. Nichols, D. S. Rimai and R. J. Sladek, *Solid State Commun.* **36** 667 (1980).

[77] J. J. Yeh and I. Lindau *Atomic Data and Nuclear Data Tables* **32** 1 (1985).

[78] W. H. Press, S. A. Teukolsky, W. T. Vetterling and B. P. Flannery *Numerical Recipies in C The Art of Scientific Computing* 2nd ed. Cambridge University Press.